Spring 3-22-2017

DESIGN OF AN O-TYPE METAMATERIAL SLOW WAVE STRUCTURE FOR HIGH POWER MICROWAVE GENERATION

Sabahattin C. Yurt
University of New Mexico

Sabahattin Cihad Yurt

Candidate

Electrical and Computer Engineering

Department

This dissertation is approved, and it is acceptable in quality and form for publication:

Approved by the Dissertation Committee:

Edl Schamiloglu , Chairperson

Christos Christodoulou

Mark Gilmore

Zhen Peng

Anil Prinja

DESIGN OF AN O-TYPE METAMATERIAL SLOW WAVE STRUCTURE FOR HIGH POWER MICROWAVE GENERATION

by

SABAHATTIN CIHAD YURT

B.Sc., Electrical & Electronic Engineering,
Istanbul University, Turkey, 2009
M.Sc., Electrical Engineering,
Istanbul Technical University, Turkey, 2011

DISSERTATION

Submitted in Partial Fulfillment of the
Requirements for the Degree of

Doctor of Philosophy
Engineering

The University of New Mexico
Albuquerque, New Mexico

May 2017

DEDICATION

To my parents Fatma and Vehbi Yurt

ACKNOWLEDGEMENTS

I would like to thank my advisor, Professor Edl Schamiloglu, for giving me the opportunity to be his PhD student. His guidance and support encouraged and inspired me to work hard on my research and complete my degree. I would also like to thank Dr. Mikhail Fuks for the useful discussions that we had regarding many research ideas. I wish him all the best for his retirement. I want to thank all the professional collaborators of my research for their help and guidance: Prof. Christos Christodoulou, Prof. Mark Gilmore, Dr. Jerald Buchenauer, Dr. Kost' Ilyenko, Dr. Sarita Prasad and Dr. Ahmed Elfrgani.

The research presented in this dissertation was supported by AFOSR MURI Grant FA9550-12-1-0489.

DESIGN OF AN O-TYPE METAMATERIAL SLOW WAVE STRUCTURE FOR HIGH POWER MICROWAVE GENERATION

by

Sabahattin Cihad Yurt

B.Sc., Electrical & Electronic Engineering, Istanbul University, Turkey, 2009
M.Sc., Electrical Engineering, Istanbul Technical University, Turkey, 2011
Ph.D., Engineering, University of New Mexico, Albuquerque, USA, 2017

ABSTRACT

The aim of this dissertation is to design a novel metamaterial slow wave structure (MSWS) for high power microwave (HPM) generation which is an efficient and compact new generation O-type device whose output parameters are comparable to, and even better than conventional devices. There is increasing interest in using metamaterials for designing HPM sources because of their so-called unique electromagnetic properties that are not found in nature, such as below cutoff propagation, which is the main property that allows for a compact design, and negative refractive index that allows backward wave propagation and reversed Cerenkov radiation. As such new beam/wave interactions can be engineered using metamaterials.

In this work, we analyzed conventional vacuum electron devices to show the similarity of properties with MSWSs at microwave frequencies and pay more attention to understanding MSWSs for HPM generation. We show that the evolution of wave dispersion in systems of all-metallic periodic structures with increasing corrugation depth

have properties similar to MSWSs used in HPM sources. We show that the main properties of MSWSs, such as the existence of the lowest order wave with negative dispersion, also appear in ordinary metallic periodic systems with deep corrugation.

Our structure in this dissertation is a broadside-coupled split ring resonator (BCSRR) slow wave structure (SWS) that produces backward waves and beam/wave interaction with a TE-like mode at an operating frequency near 1.4 GHz. It is an array of periodically loaded all-metallic split ring resonators (SRRs) in a cylindrical waveguide with an output horn to extract power efficiently. This MSWS allows for high power extraction at the output, up to 310 MW and with 20% beam-to-RF conversion efficiency in a compact design compared to conventional backward wave oscillators (BWOs). We performed cold test experiments on a crudely manufactured MSWS in order to measure the resonant frequency and passband characteristics from the S-parameters using a TE-like mode launcher. Hot test experiments have validated the virtual protoyping design of this MSWS-based HPM source.

TABLE OF CONTENTS

LIST OF FIGURES

LIST OF TABLES

CHAPTER 1: INTRODUCTION

1.1. Background

High power microwaves (HPM) have found applications in many areas including the military, radar systems, space technology, etc. It is usually defined as devices that exceed 100 MW peak power with output frequencies ranging from 1 GHz to 300 GHz and even higher [1]. In recent decades, there have been many developments in HPM technology that use innovative methods which lead to new applications. Advances in microwave sources, such as miniaturization of the sources, improving them for higher efficiencies, and the innovative use of metamaterials in confining, controlling and radiating intense microwave pulses by engineering dispersion relations that cannot be produced using conventional periodic structures all contribute to HPM device development. With recent developments, HPM sources have reached up to 15 GW peak power levels with high efficiency [1].

Conventional HPM sources can be categorized as O-type and M-type devices. O-type devices comprise different forms of BWOs and traveling wave tubes (TWTs). These devices rely on using different configurations of slow wave structures (SWSs) for their operation. SWSs are used because the phase velocity of the waves within them are less than the speed of light and allow for resonance with the electron beam velocity. Since the electron motion in these devices is along the axial guide magnetic field, they are called O-type devices. In M-type devices, however, electron drift is perpendicular to the crossed electric $\boldsymbol{E}$ and magnetic $\boldsymbol{B}$ fields, such as in magnetrons. In these devices, electrons in the

interaction region perform an $\boldsymbol{E}\times\boldsymbol{B}$ drift and are recirculant, which is why M-type devices tend to operate with higher efficiency. In contrast, in O-type devices the electrons are produced external to the SWS and electrons perform a single transit through the system.

The magnetron was invented by American engineer Albert W. Hull while working for General Electric. Cavity magnetron and cooker magnetron inventions followed that in 1934 and in the 1940s, respectively. One can say that the cooker magnetron became the most commercialized microwave device in history. In the 1930s, the klystron was proposed after several investigations on resonant cavity devices. Rudolf Kompfiner invented the TWT during World War II [2] and, later on, his work was refined by John R. Pierce and other researchers. Using intense relativistic electron beam (IREB) technology, 10 MW of output power with 0.05% efficiency was achieved for the first time by John Nation of Cornell University [3]. The first true HPM source, a relativistic BWO that can provide 400 MW with 10 ns pulse duration in X-band was proposed by Russian researchers in 1973 [4, 5]. For the similar BWO, output power was improved to 500 MW by Cornell University right after Russian scientist's achievement [6]. TWTs are used mostly as amplifiers in satellite transponders and radars. The cross-field amplifier was developed in the 1960s. The first relativistic M-type HPM device was developed in 1976 Bekefi and Orzechowski at MIT.

If the electron beam/wave interaction takes place in a SWS waveguide and the phase velocity of the wave is less than the speed of light c, then the device is called a slow wave device, such as the case with TWTs and BWOs. If the phase velocity is greater than c, then the device is called a fast wave device and includes gyrotrons, cyclotron autoresonance masers, and free electron lasers (FELs or ubitrons) [7]. Microwave sources

can also be categorized through their mode of interaction. In general, TWTs interact with the transverse magnetic (TM) mode, gyrotrons interact with the transverse electric (TE) mode, and FELs can interact with either TE or TEM modes. In some cases, hybrid modes, which are a combination of TE and TM modes, can be the interaction mode of devices. The HE_{11} and EH_{11} modes are the most common hybrid interaction modes for some microwave sources.

HPM sources can be classified as amplifiers (as in TWTs) or oscillators (as in BWOs). In amplifiers, the high power RF is produced through a convective instability, whereas in an oscillator the high power RF is produced through an absolute instability. In general, a low power seed RF signal is required for an amplifier, whereas oscillations grow from noise. See [8] for additional information.

Another classification of microwave sources is whether they are relativistic or non-relativistic. In relativistic sources the beam energy usually >200 keV with current >250 A and they operate in pulse durations from 10s ns to 1 μs [7].

Recently, there has been growing interest in using metamaterials for designing microwave sources because of their unusual electromagnetic properties that do not exist in nature. Several MSWSs have been characterized and tested experimentally and reported in the literature. The most significant contribution of the MSWS design is the compactness of the microwave source because of its double negative behavior (permittivity $\varepsilon < 0$ and permeability $\mu < 0$) and below cutoff propagation properties which allows for smaller radial dimensions than traditional all-metallic structures. In this dissertation a novel MSWS-based HPM source design will be analyzed from the early design steps to the final experimental hot test verification.

Let us consider the subsystems of an HPM device briefly, and then we will discuss the operation of an HPM system in more detail in the next chapter. The HPM subsystems are described as follows and are illustrated in Figure 1.1 [1]:

1. A low voltage source (prime power) is used to charge a capacitive energy store. On a mobile system a DC to DC converter might also be used.
2. High voltage is achieved by either using a Marx generator or Tesla transformer that is connected to a pulse forming line. (The load is a coaxial magnetically insulated diode for the MSWS.)
3. A beam/wave interaction region is where the kinetic energy of electrons is converted to HPM through a resonance condition with the phase velocity of the electromagnetic mode.
4. A mode converter might be used to take the output of the HPM source and convert it to a more user-friendly mode, such as the TE_{11} mode.
5. An antenna subsystem is used to radiate the desired mode with some efficiency and gain.

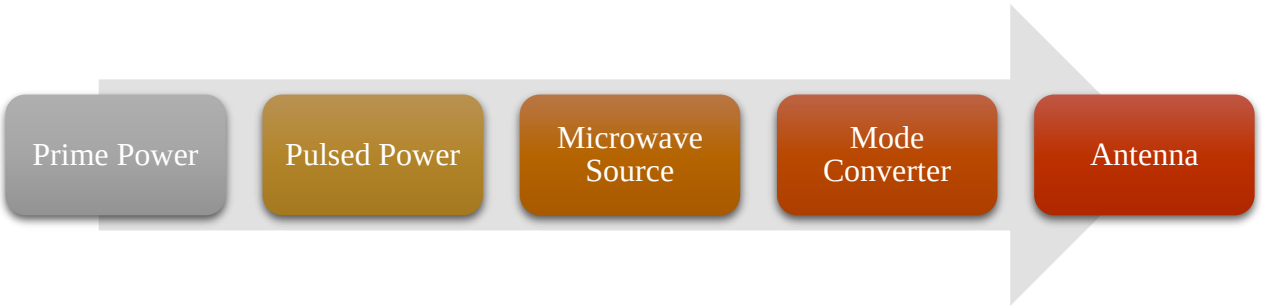

Figure 1.1 Subsystems of an HPM device.

1.1.1. Organization of this Dissertation

The research performed in this dissertation was funded by the Air Force Office of Scientific Research (AFOSR) within the Multidisciplinary Research Program of the University Research Initiative (MURI) under Grant FA9550-12-1-0489 with the involvement of five universities and the leadership of the University of New Mexico (UNM). The organization of the remainder of this dissertation is summarized as follows:

In Chapter 2, the basic theory and background of BWO, TWT, and relativistic magneron HPM devices is given, along with some information on their historical development. In the second half of this chapter, an introduction to metamaterials and the idea of using them in HPM devices is explained.

Chapter 3 shows the similarity of the properties of MSWSs and conventional metallic periodic structures, such as rectangular- and sinusoidally-corrugated BWO geometries. Essentially, this chapter shows that conventional periodic structures used in HPM devices have properties that were thought to be unique to MSWSs.

Chapter 4 presents the results of particle-in-cell (PIC) computer simulations of the proposed MSWS presented in this dissertation. Cold test simulations were performed using HFSS [9] and CST Microwave Studio [10]. Hot tests were performed using the fully relativistic 3D PIC codes MAGIC [11] and CST Particle Studio.

Chapter 5 presents experimental results that have been performed in UNM's HPM Laboratory with the SINUS-6 electron beam that validates the PIC simulations of the MSWS.

Finally, Chapter 6 presents the conclusions and suggestions for future work.

CHAPTER 2: THEORY OF OPERATION OF TWTS AND BWOS AND HPM FUNDAMENTALS

In this chapter we will review the fundamental principles of operation of TWTs and BWOs since our proposed MSWS is a Cerenkov device similar to them. HPM fundamentals will also be review. We first begin with a review of the fundamental velocities encountered in a guided wave system.

2.1. Energy Flow and Velocities

We start from Maxwell's equations,

$$\nabla\times\boldsymbol{E} = -\frac{\boldsymbol{\partial B}}{\boldsymbol{\partial} t} \tag{2.1}$$

$$\nabla\times\boldsymbol{B} = \mu_0\boldsymbol{j} + \frac{1}{c^2}\frac{\boldsymbol{\partial E}}{\boldsymbol{\partial} t} \tag{2.2}$$

$$\nabla\cdot\boldsymbol{B} = 0 \tag{2.3}$$

$$\nabla\cdot\boldsymbol{E} = \frac{\rho}{\varepsilon_0}, \tag{2.4}$$

where $\boldsymbol{E}$ and $\boldsymbol{B}$ are the electric and magnetic fields, and the sources terms are the charge ρ and current $\boldsymbol{j}$ densities**.** ε_0 and μ_0 represent the permittivity and permeability of free space, respectively. In order to proceed, boundary conditions also need to be determined. In a linear medium, the following energy conservation relation can be extracted from Maxwell's equation

$$\nabla\cdot\boldsymbol{S} + \frac{\partial}{\partial t}\left[\frac{1}{2}\varepsilon_0\varepsilon_r\boldsymbol{E}\cdot\boldsymbol{E} + \frac{1}{2}\mu_0\mu_r\boldsymbol{H}\cdot\boldsymbol{H}\right] = -\boldsymbol{j}\cdot\boldsymbol{E} \tag{2.5}$$

where

$$\boldsymbol{S} \equiv \boldsymbol{E}\times\boldsymbol{H}. \tag{2.6}$$

Equation 2.6 is related to the energy flux and is called the Poynting vector. Moreover, the second term on the left hand side is the instantaneous energy density related to the electric and magnetic fields

$$w \equiv \frac{1}{2}\varepsilon_0\varepsilon_r \boldsymbol{E}\cdot\boldsymbol{E} + \frac{1}{2}\mu_0\mu_r \boldsymbol{H}\cdot\boldsymbol{H}. \tag{2.7}$$

In a linear medium, Gauss's theorem is used, and integral form of the previous equation can be written as

$$W(t) \equiv \int_V \left[\frac{1}{2}\varepsilon_0\varepsilon_r \boldsymbol{E}\cdot\boldsymbol{E} + \frac{1}{2}\mu_0\mu_r \boldsymbol{H}\cdot\boldsymbol{H}\right] dV. \tag{2.8}$$

This is the total energy stored in the volume.

Here it is assumed that the electromagnetic power is not guided by metallic walls or waveguides. If waveguides are involved, we need to consider modes since each mode propagates power along the longitudinal direction of the structure independently. Analysis of energy flow in a waveguide can be easily shown for the TE_{01} mode in a rectangular waveguide with boundaries $0 < x < a$ and $0 < y < b$ [12]:

$$\boldsymbol{E_y} = i\frac{\omega a\mu}{\pi} H_0 \sin\left(\frac{\pi x}{a}\right) e^{i(kz-\omega t)} \tag{2.9}$$

$$\boldsymbol{H_x} = \frac{i}{\omega}\frac{\partial E_y}{\partial z} = -i\frac{ka}{\pi} H_0 \sin\left(\frac{\pi x}{a}\right) e^{i(kz-\omega t)} \tag{2.10}$$

$$\boldsymbol{H_z} = -\frac{i}{\omega}\frac{\partial E_y}{\partial x} = H_0 \cos\frac{\pi x}{a} e^{i(kz-\omega t)} \tag{2.11}$$

where *k* is the wavenumber,

$$k = \sqrt{\frac{\omega^2}{c^2} - \frac{\pi^2}{a^2}} \tag{2.12}$$

and c is the speed of light. Then, the time-average Poynting vector can be written as

$$\langle \boldsymbol{S} \rangle = \frac{k}{\omega}\frac{cE_0^2}{2\eta_0}\sin^2\frac{\pi x}{a}\hat{z}, \tag{2.13}$$

which shows the energy flow along the guide. Here $\omega/k = v_p$ is the phase velocity and $d\omega/dk = v_g$ is the group velocity. These two velocities will be explained in more detail next.

Before explaining the beam/wave interaction phenomenon, it is useful to explain some characteristic parameters including energy, phase, and group velocities, as well as characteristic impedance in order to characterize the interaction.

Energy Velocity

Energy velocity is defined as power flow divided by total energy per unit length in a system that has small input signal

$$v_e = \frac{P}{W_M + W_E}. \tag{2.14}$$

For a cylindrical waveguide with one propagating mode, it can be written as [13]

$$v_e = c\frac{1}{\varepsilon_r}\sqrt{\varepsilon_r - \left(\frac{J_{01}c}{\omega R}\right)^2} \tag{2.15}$$

where $J_{01}$is the zero of the Bessel function of the first kind.

Phase Velocity

Phase velocity is the speed at which any fixed phase of the moving cycle flows

$$\boldsymbol{v_p} = \frac{\omega}{k}. \tag{2.16}$$

The phase velocity of electromagnetic modes in a hollow smooth-walled waveguide are all greater than the speed of light c. However, if the waveguide is filled with a dielectric the phase velocity is reduced via $v_p \sim c/\sqrt{\varepsilon_r}$. The magnitude of the phase velocity is related to the direction of wave motion.

Group Velocity

For a system of two oscillating waves at adjacent frequencies described by

$$f(z,t) = \cos(\omega_1 t - k_1 z) + \cos(\omega_2 t - k_2 z) \tag{2.17}$$

where frequencies $\omega_1 = \omega + \Delta\omega, \omega_2 = \omega - \Delta\omega$ and wavenumbers $k_1 = k + \Delta k,\ k_2 = k - \Delta k$. Equation 2.17 can be rewritten as

$$f(z,t) = 2\cos(\Delta\omega t - \Delta k z)\cos(\omega t - kz) \tag{2.18}$$

where one can write the velocity in the limit $\Delta\omega \to 0$ as

$$v_g = \frac{\partial\omega}{\partial k}. \tag{2.19}$$

The group velocity is the velocity of wave energy flowing in the direction of the Poynting vector. It should be pointed out that if the group velocity and the phase velocity are in opposite directions, the propagation of the wave is referred to as *backward wave propagation.* When the group velocity and phase velocity are in the same direction, interaction is periodic instead of continuous [7].

Characteristic Impedance

Characteristic impedance is one of the important parameters of HPM systems. In order to have a good electrical match, the characteristic impedance should be added to design considerations. It is usually defined as the ratio between the transverse components of the E_r and H_ϕ fields in a cylindrical waveguide,

$$Z = \frac{E_r}{H_\phi}. \tag{2.20}$$

Interaction Impedance

Interaction impedance is directly related to device efficiency. For this reason, higher interaction impedance is always desired. It is defined by the longitudinal electric

field in the interaction region where the beam is injected. For a thin pencil beam ($0 < r < R_b$), it can be written as [13]

$$Z_{\text{int}} \equiv \frac{1}{2}|E_z|^2 \pi R^2 \frac{1}{P_z} \tag{2.21}$$

where P_z is the longitudinal power flow.

It should be pointed out that the maximum efficiency can be achieved when a longitudinal component of the electric field has higher values. It is the key element of HPM device design for better interaction and efficiency. Higher efficiencies can also be achieved by designing a structure with a smaller radius, or lower group velocity, which is the case for MSWS design.

All these parameters described here are referred to as cold parameters of the HPM structure (without the presence of the electron beam). In the next section a detailed characterization of cold parameters using dispersion engineering will be described.

2.2. Dispersion Engineering

If the wave velocities change with frequency in a circuit or a system then the circuit or system is said to be dispersive or to have dispersion. This is usually described by a ω-β diagram or Brillouin diagram, which is attributed to Brillouin's original work in 1946 [14]. Here, ω is the angular frequency and β is the wave propagation constant.

Waves in a waveguide can propagate either in the forward or backward directions and for each direction the dispersion diagram is symmetric. The dispersion diagram for a smooth-walled waveguide is asymptotic with the light line as shown in red in Figure 2.1.

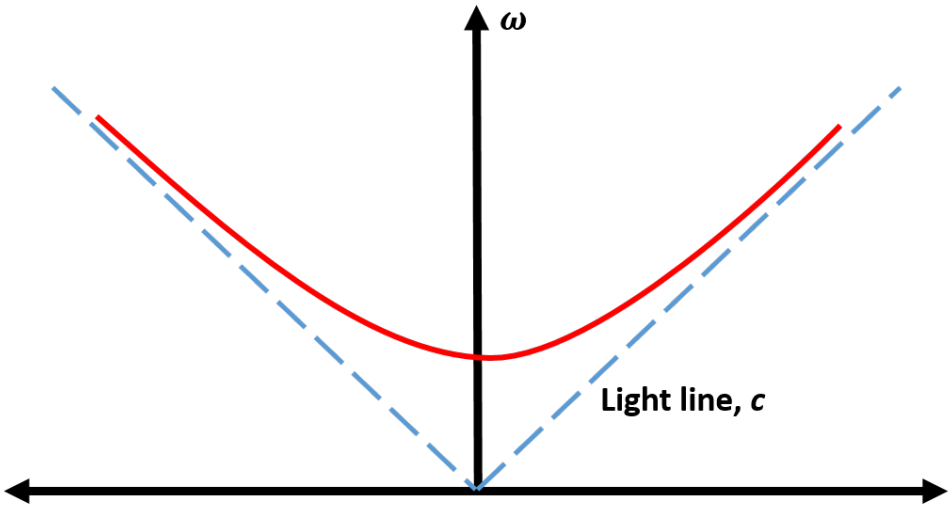

Figure 2.1 Dispersion diagram for the symmetric waves of a smooth-walled waveguide.

To better understand the dispersion characteristics and backward wave phenomena, a periodically loaded waveguide example will be studied here. Periodically loaded waveguides can be created by adding equally spaced metal vanes or cavities as an obstacle inside the waveguide in order to change the impedance of the structure. Each obstacle creates a reflection and in some point total reflection might occur. This phenomenon is called the *stopband*. If the waves can propagate in a periodically loaded waveguide, then this is referred to as a *passband*. When frequencies are close to the cutoff frequency ω_c, the phase velocity will be high and the wavelength will be longer than the obstacles' spacing. If the group velocity is zero, there will be no propagation.

In a periodic system shown in Figure 2.2 with spacing L between vanes, if βL is less than π, then the wave is referred to as a forward wave as in Figure 2.2 (a). At the point $\beta L = \pi$ when the phase velocity has higher values and the wavelength will be longer. If βL is greater than π, the wave will travel in the opposite or backward direction as in Figure

2.2 (b). If we consider the presence of a beam, when the electrons move at the same phase velocity of the wave, the electrons will maintain synchronism with the wave.

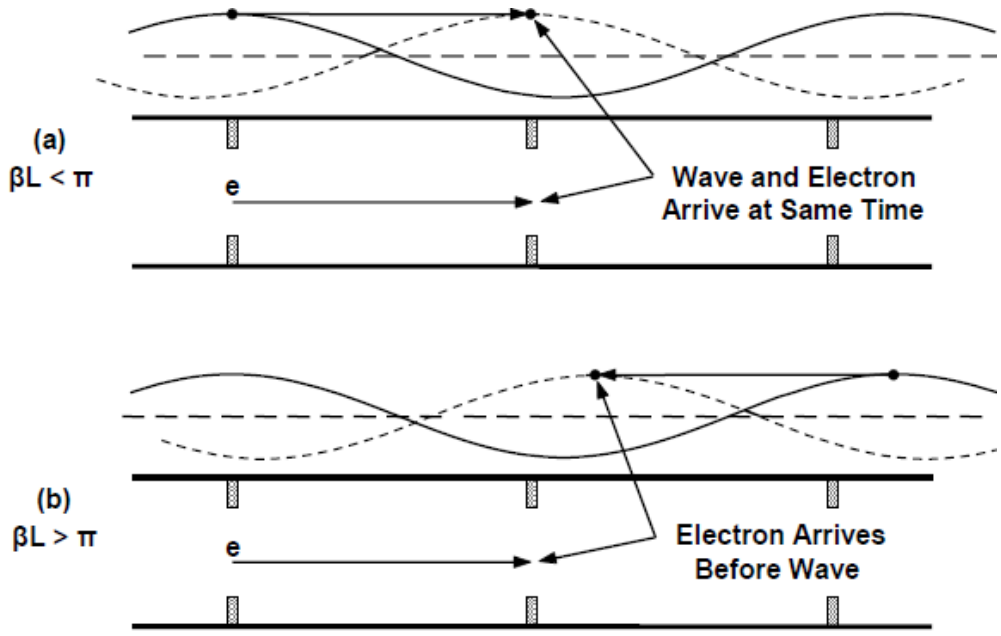

Figure 2.2 Illustration of a) forward and b) backward wave in a periodically loaded waveguide [7].

For synchronism of the wave and electrons with the backward wave, electron velocity will be decreasing when the backward wave reaches the peak. Therefore, the phase velocity of the wave will be less than the phase velocity of the forward wave.

If a backward wave is supported between π to 2π the dispersion diagram will be as shown in Figure 2.3. Since the dispersion characteristics are symmetric on each side for a periodic system, one can expect the same behavior for the region from 0 to -2π. Similarly, for the values of $\beta L > 2\pi$ a forward wave will once again exist. When $\beta L = 2\pi$ it is the point close to the cutoff condition of the waveguide and the phase velocity approaches infinity.

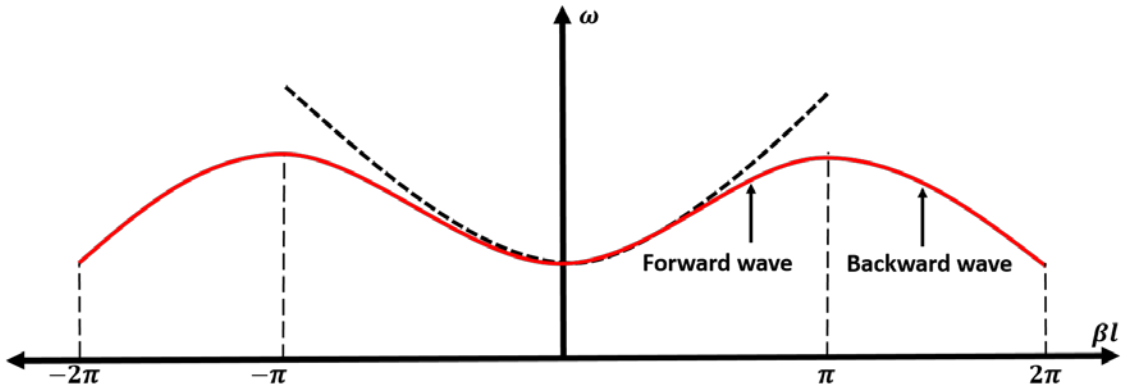

Figure 2.3 Dispersion diagram for the region 0<βL<2π.

With the cutoff condition, the upper and lower limits of frequencies are defined, and this creates the passbands for different propagating modes. This behavior can be seen in Figure 2.4 for the first four passbands.

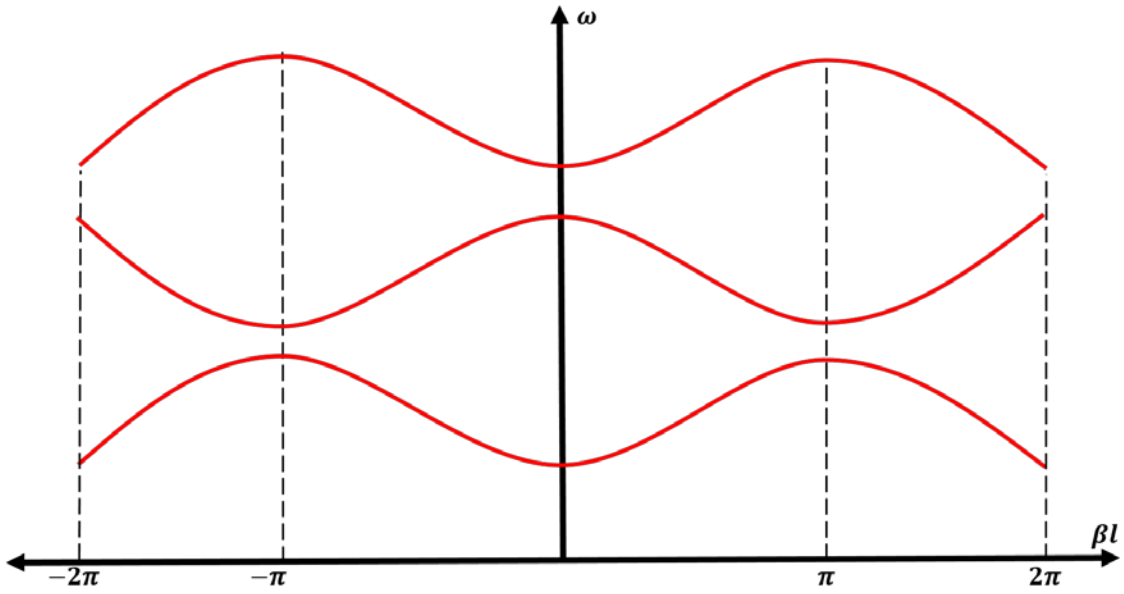

Figure 2.4 Dispersion diagram for a metallic vane-loaded waveguide.

Cerenkov Radiation

When the electron beam velocity exceeds the phase velocity of the electromagnetic wave in a medium Cerenkov radiation is emitted. In this case, resonant energy transfer to

the wave occurs along with electron bunching as a result of more electrons being decelerated than accelerated. Accelerated and decelerated electrons are illustrated in Figure 2.5 along with electron bunching.

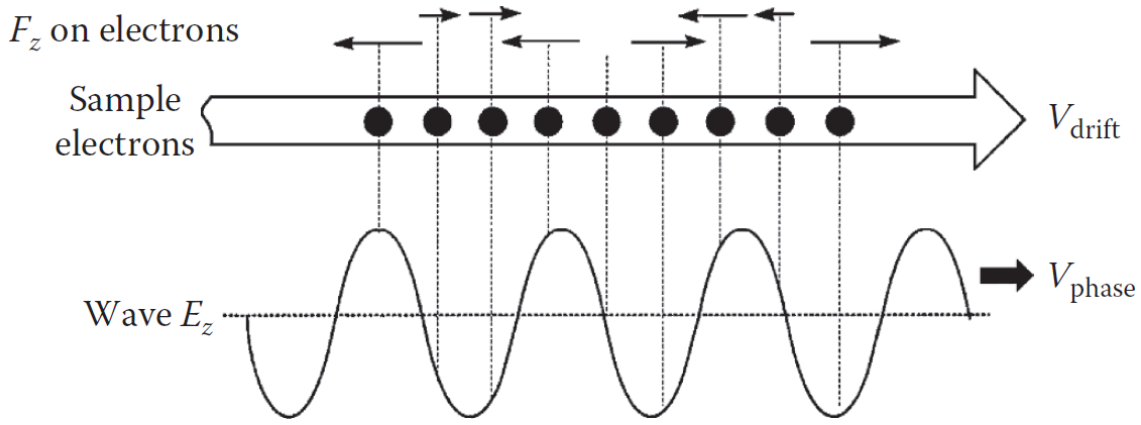

Figure 2.5 Electron bunching in an SWS [1].

For a wave propagating in a medium with index of refraction n at an angle θ with the longitudinal direction, the corresponding wavenumber is written as [13],

$$k_z = \frac{\omega}{c} n \cos\theta = \frac{\omega}{c}\frac{1}{\beta} \tag{2.22}$$

where θ is the Cerenkov radiation angle

$$\theta = \cos^{-1}\left(\frac{1}{n\beta}\right). \tag{2.23}$$

2.3. Electron Generation and Emission Models

Electrons that are attached to atoms need to be separated in order to have them available for generating a beam. This separation can be achieved by using several emission mechanisms including field-emission, thermionic emission, photo-emission, secondary emission, and explosive emission. These models will be briefly discussed here. Electron

emission from a cathode surface of an electron gun is illustrated in Figure 2.6. When electrons are generated, they are guided by a magnetic field and waveguide through a beam/wave interaction region.

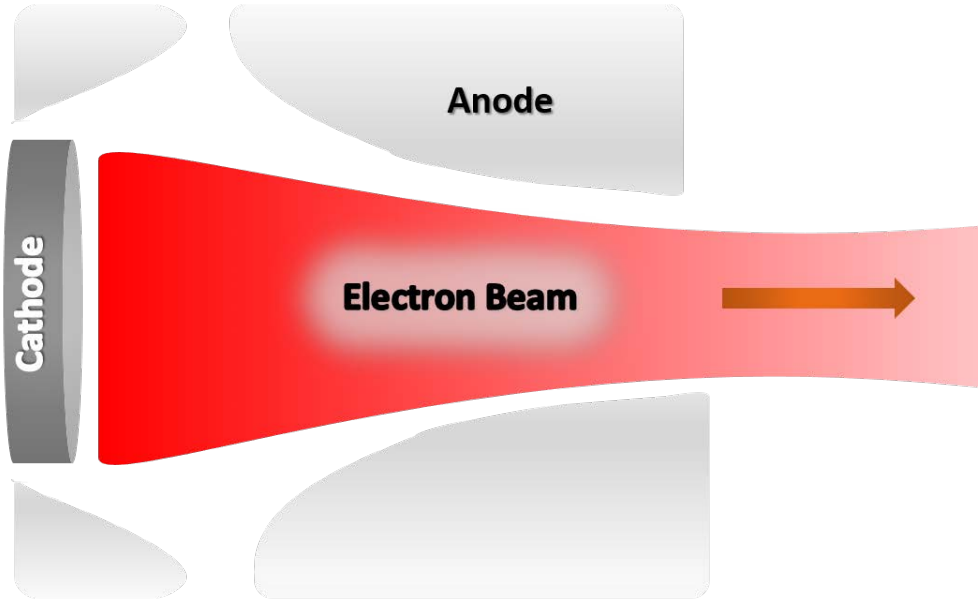

Figure 2.6 Electron emission near the cathode in an electron gun.

Field-Emission

If electrons are extracted from a cathode surface with the force of an electric field that is perpendicular to the surface, then it is called field-emission. When the applied electric field increases from 10^9 to 10^{10} V/m level, electron emission increases dramatically and is independent of cathode temperature and surface conditions [7]. Electron tunneling through a barrier at the vacuum side might occur as a result of the electrons' physical nature. The Fowler-Nordheim equation describes the current density field-emitted from a surface

$$J = aE^2 e^{-\frac{b}{E}} \tag{2.24}$$

where *a* and *b* are constants related to the material and *E* is the electric field.

When a large number of the electrons is emitted with the electric field at the cathode surface that is forced to be zero, it is called space-charge-limited emission. The *Child-Langmuir law* defines the maximum current that can be emitted with an applied voltage. It can be written for a planar space-charge-limited diode as

$$J = 2.33\times10^{-6}\frac{V^{3/2}}{x^2} \tag{2.25}$$

with the spacing between planar electrodes given by x. Moreover, for a diode with spacing *d* between the anode and cathode

$$J = \frac{PV^{3/2}}{A} \tag{2.26}$$

where *A* is the cathode area and *P* is known as the *perveance* and is given by

$$P = 2.33\times10^{-6}\frac{A}{d^2}. \tag{2.27}$$

Child-Langmuir space-charge-limited emission is the most common mechanism in HPM sources using explosive emission diodes. Explosive emission can lead to current densities exceeding 1 kA/cm^2.

Thermionic Emission

Thermionic emission occurs when the cathode surface is heated the bound electron can overcome the work function and become free [15]. Depending on the increasing temperature of the cathode surface, more current flows and the electron density around the cathode surface becomes greater. It is not possible to emit more electrons with increasing

temperature after a certain point where the potential might be negative near the cathode surface with additional electrons. The current density can reach up to 100 A/cm^2, but this level is still less than those for field-emission and explosive emission. The most common thermionic emitter types are classified by the material of cathode, such as tungsten, LaB_6, BaO, thorium-based cathodes, etc. Their thermal properties play an important role in the cathode selection for thermionic emission. The relation between emitted current density *J*, work function *W*, and temperature *T* is given by the Richardson-Dushman formula

$$J = A_0 T^2 e^{-\frac{W}{kT}} \tag{2.28}$$

where $A_0 = 4\pi qmk^2/h^3 = 1.2\times10^6 \mathrm{Am}^{-2}\mathrm{K}^{-2}$. Here k is the Boltzmann constant, h is Planck's constant, q is the particle charge, and m is the particle mass. Electron emission starts with a velocity given by

$$v_{\text{start}} = \sqrt{3k\frac{T}{m}}. \tag{2.29}$$

Photo-Emission

If a laser illuminates the cathodes surface, electrons can find sufficient energy to overcome the work function and leave the surface of the cathode. The advantage of this type of emission is that electron emission can be easily controlled by the laser pulse. Hence, photocathodes are frequently used to form prebunched electron beams. The most common materials for photo-emission are GaAs and Cs_3Sb.

Secondary Emission

When a primary electron has sufficient energy and hits the cathode surface, it can induce the emission of secondary electrons. This phenomenon is called *secondary electron emission*. The most commonly used materials for secondary emission cathodes are BeO, MgO, GaAsP, and PbO. Secondary emission cathodes are commonly used in cross-field tubes such as magnetrons and cross-field amplifiers.

Explosive Emission

Explosive emission is the most common emission model that is used in HPM devices. It is dependent on the electric field. When the electric field strength around the cathode surface is larger than the threshold level, which is usually 100 kV/cm, explosive electron emission is initiated. After emission starts, this threshold level does not affect the emission any further. This type of cathode can be made from different materials, such as aluminum, graphite, and stainless steel. Space-charge-limited operation is involved in explosive emission diodes so that the current density extracted is governed by the Child-Langmuir relationship. One exception to this is when a thin-walled annular magnetically insulated cathode is used, such as is commonly the case in BWOs. Here the current density is determined by the Fedosov solution [1].

In this dissertation, explosive emission will be the main emission mechanism for experimental and PIC simulation considerations.

2.4. Beam Propagation

After electrons are generated following the explosive electron emission process on the cathode, they have to be guided through the interaction space within a waveguide by a magnetic field. An axial magnetic field is the most common way to confine the electrons, and it can be either be uniform or periodic. Divergence caused by Coulomb repulsion can be overcome by using an applied axial magnetic field.

If the electron beam propagates within metallic boundaries (waveguide or vacuum pipe) the total energy becomes the sum of kinetic and potential energy. All the electrons will have the same kinetic energy $mc^2(\gamma_0 - 1)$ and the potential energy changes inside the waveguide. Since the electrons have different potentials in the waveguide because of their varying location, although they are injected with same kinetic energy, eventually they will have different kinetic energy [13]. A schematic of a waveguide with the presence of an electron beam is shown in Figure 2.7 with beam radius R_{BEAM} and radius of cylindrical waveguide R.

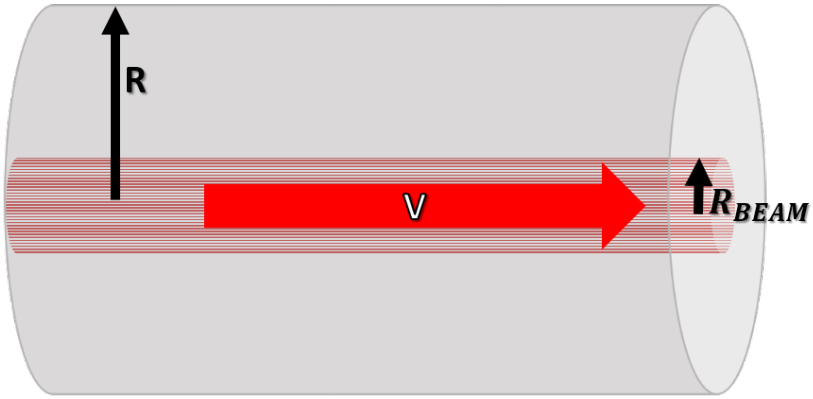

Figure 2.7 Illustration of a cylindrical waveguide with an electron beam.

The maximum current flow in the waveguide with the presence of an electron beam can be calculated with the consideration of kinetic and potential energy changes. The electrostatic potential satisfies Poisson's equation in the waveguide

$$\frac{1}{r}\frac{d}{dr}r\frac{d}{dr}\phi(r) = \frac{1}{\varepsilon_0}en(r). \tag{2.30}$$

After solving the equation based on Green's scalar theorem with beam radius R_b and assumption of energy and charge conservation, the potential can be written as

$$\phi(R_\mathrm{b}) = -\frac{J}{c\varepsilon_0}\ln\left(\frac{R}{R_\mathrm{b}}\right)\int_0^{R_\mathrm{b}} r\left(1-\left(\gamma_0+\frac{e\phi(r)}{mc^2}\right)^{-2}\right)^{-0.5} dr \tag{2.31}$$

where $mc^2(\gamma_0 - 1)$ is the kinetic energy of the beam at the input. For a narrow pencil beam, $\phi(r)$ can be replaced by $\phi(\mathrm{R_b})$ since the potential will not be changing significantly. Finally, the maximum current flow can be written as follows which is the Child-Langmuir axial space-charge-limiting current [13]

$$I_\mathrm{max} = \frac{mc^2}{e\eta_0}\frac{2\pi}{\ln\left(\frac{R}{R_b}\right)}\left(\gamma_0^{\frac{2}{3}}-1\right)^{1.5}. \tag{2.32}$$

Attempting to propagate currents greater than I_max will lead to virtual cathode formation. If it is desired to decrease the limiting current, one can increase the distance between the beam and the inner wall of the waveguide. Thus, potential depression will be decreased, and the limiting current will increase when the beam gets closer to the inner wall of the waveguide.

2.5. Periodic Structures

Beam/wave interaction can be achieved by loading a waveguide either with dielectric or periodic obstacles or cavities (corrugations). For beam/wave interaction, periodic structures play an important role since the phase velocity of spatial harmonics can be reduced to less than the speed of light and equal to the speed of the electrons. The electromagnetic wave in a periodic structure can be specified by wavenumber, phase velocity, group velocity, and interaction impedance at a frequency for a single mode. Periodic metallic structures are the most commonly used structures in HPM technology due to their low loss, tolerance for high field gradients, and ease of manufacture [13]. Periodically loaded waveguides create wave propagation delay because of the reflections close to the obstacles and this, in turn, leads to developing of an infinite spectrum of spatial harmonics. A few of these harmonics propagate faster than the phase velocity of the electromagnetic mode, but most of them propagate slower. For this reason, they are called SWSs. Most popular SWSs consist of wire helices, rods, and periodic corrugations of the waveguide wall. Thus, in SWSs, the main interest is in the spatial harmonics or monochromatic plane waves [16].

SWSs are typically characterized by Floquet's theorem. Floquet's theorem is applicable to a function $f(z)$ which has a value at point z that is equal to its value at the point $z + L$. Here L is a function of periodicity

$$f(z) = f(z + L). \tag{2.33}$$

Periodic functions can also be described using trigonometric functions

$$f(z) = \sum_{n=-\infty}^{\infty} f_n \, e^{-j2\pi n \frac{z}{L}}. \tag{2.34}$$

Based on the Fourier series of Equation 2.34, we end up with a general solution of the function for periodic structures

$$f(z) = \sum_{n=-\infty}^{\infty} f_n \, e^{-j\left(2\pi n\frac{z}{L}+kz\right)} \tag{2.35}$$

which satisfies

$$f(z) = e^{jkL} f(z + L). \tag{2.36}$$

These last two equations are known as Floquet's theorem.

In addition to the concept of a periodic structure, there are also quasi-periodic structures available. The main problems encountered with them are: having a clean spectrum with decreasing the reflections and avoiding oscillations, electrical breakdown issues, and compensating for the reduction in electron velocity as the beam exchanges energy with the electromagnetic mode during its transit through the SWS [13].

The most common application of a beam/wave interaction with a forward wave is in amplifiers, such as TWTs, and with the backward wave is oscillators or BWOs. These are the two most important classification of periodic structures as mentioned earlier and to be studied here.

Before investigating the O-type devices in detail, the operating principles of SWSs will be summarized here with the basic configuration shown in Figure 2.8 [1]. The electron beam that generates the energy for microwaves and specifies the output power and pulselength is guided by an axial magnetic field which also affects the system performance significantly. Cutoff waveguide section is added to reflect the backward propagating wave into a forward propagating wave (although cavity reflectors are now more common). Microwaves are generated due to the interaction of the electron beam with the -1st spatial harmonic of the SWS, and its frequency of operation with the output mode is determined

by the intersection of the electron beam line with the dispersion diagram. Finally, beam dumping occurs at the walls of the tube right before the antenna and microwaves are radiated through the antenna in the forward direction (endfire configuration).

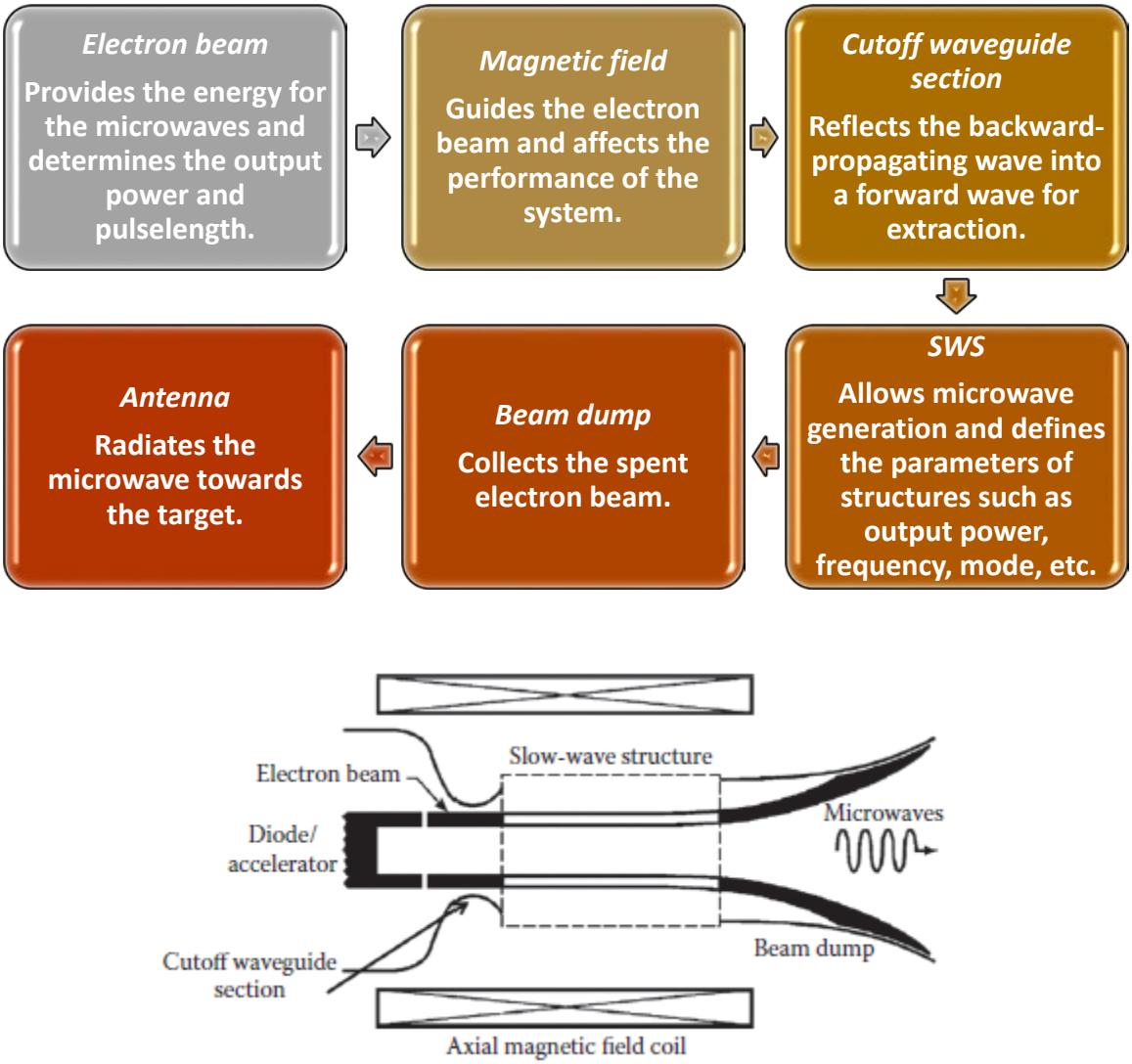

Figure 2.8 Operating principles and basic configuration of O-type HPM devices [1].

2.5.1. TWT

As mentioned earlier, if an electromagnetic wave travels in the interaction region of a waveguide with a phase velocity less than the speed of light and if the electron beam line intersects the dispersion relation of the SWS when the group velocity is postive, then the interaction is a TWT interaction, which is also a Cerenkov device. Essentially the modulated beam and electromagnetic field will grow dramatically with distance along the interaction structure. When the beam velocity and the phase velocity of the electromagnetic mode are in synchronism a beam/wave interaction occurs, and this can be characterized by the interaction impedance as it was given in Equation 2.21. It can be rewritten in a simple form as follows

$$Z_{\text{int}} = \frac{E^2}{2k^2P}. \tag{2.37}$$

This is the basic form of the equation that was first introduced by Pierce in 1950 for the TWT. He also described the techniques that allow for the suppression of backward waves and oscillations. If a beam travels parallel to the electromagnetic field, it can also propagate in the other (backward) direction. This is an undesired feature for an amplifier design. However, it is the fundamental parameter for an oscillator model. Another contribution of Pierce's was that supporting dielectric rods in helix TWT were extensively studied.

Synchronism with an electron beam and an electromagnetic wave creates electron bunches in a TWT and the interaction will be continuous. TWT design and its applications can be varied in different configurations, such as in the helical design for broadband applications, as a coupled cavity (can be disk loaded waveguide) structure for HPM applications, dielectric-loaded waveguide, or folded waveguide for other applications. TWTs have also been used for applications such as radar systems, electronic warfare

systems, and satellite communications. However, TWTs have received less attention than other microwave sources because of their sideband control and suppression of parasitic oscillations, although they can reach up to 1 GW power levels with more than 20-30% efficiency [1]. Some of configurations of TWTs are illustrated in Figure 2.9.

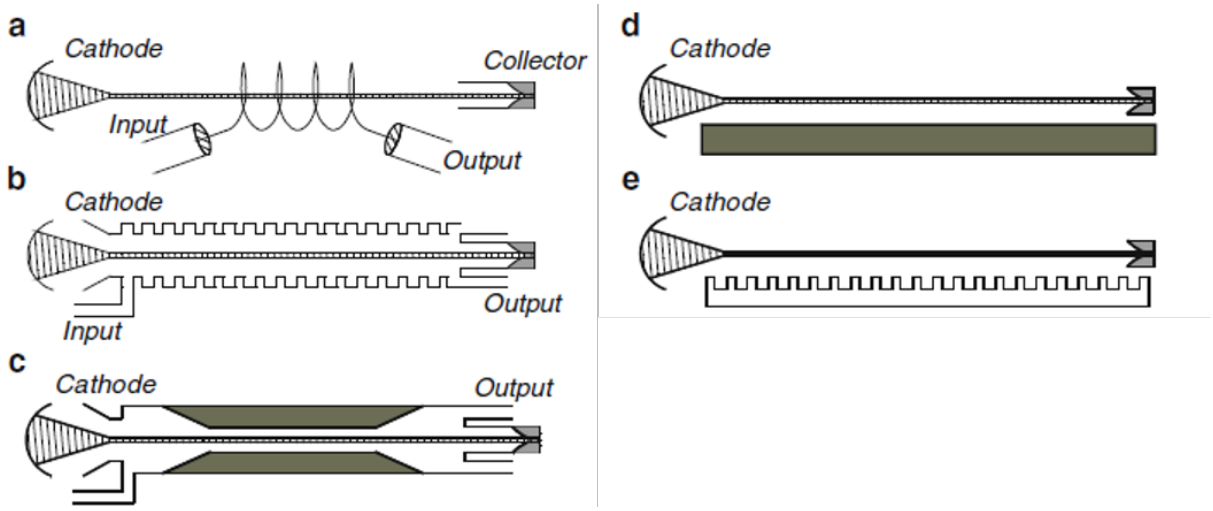

Figure 2.9 Illustration of TWT amplifier with different configurations a) helix, b) coupled cavity, c) dielectric loaded, d) open dielectric structure, e) open periodic structure [13].

The operation of TWTs mainly depends on the electron beam propagating along the z-axis and on the beam's radial distribution. Interaction in TWTs usually occurs with TM modes due to their strong longitudinal electric field E_z component. Beam location is important because the beam needs to interact with the E_z field. The electron beam is usually a pencil beam focused on-axis (as is shon in Figure 2.9), or can be an annular beam. For the operation of TWT we will investigate the helix TWT as an example here (Figure 2.10). The helix TWT is a relatively low power device compared to other TWT configurations, but it has broadband capability.

As an electron beam transits through the helix some electrons are accelerated while others are decelerated by the axial electric field components. Eventually with time, electron

bunches are created because some electrons are decelerated while others are accelerated, depending on the phase of the axial electric field they are located in. The helical shape of the structure allows the electromagnetic wave to have almost the same phase velocity as the electron bunches in the beam. Because of the phase shift between helical pitches, electrons are forced into the bunched region and the wave amplitude gets larger over time. This, in turn, leads to increasing RF power in order to complete the amplification process. Figure 2.11 shows the schematic view of bunch formation.

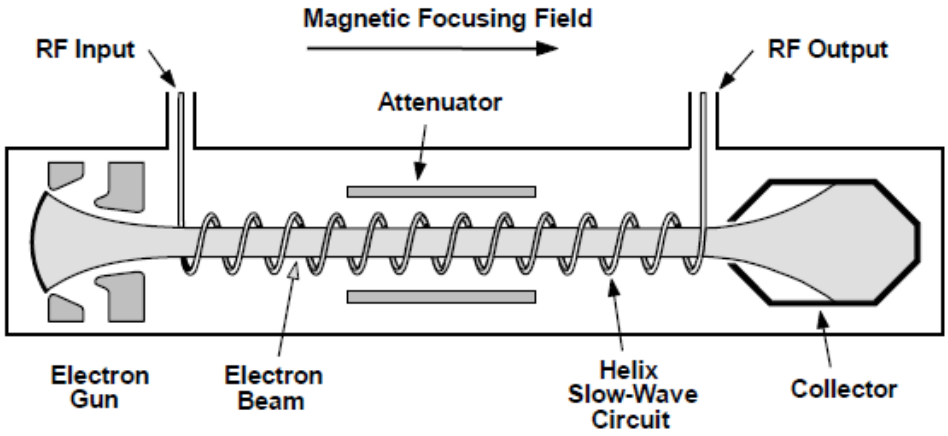

Figure 2.10 Illustration of a helix TWT [7].

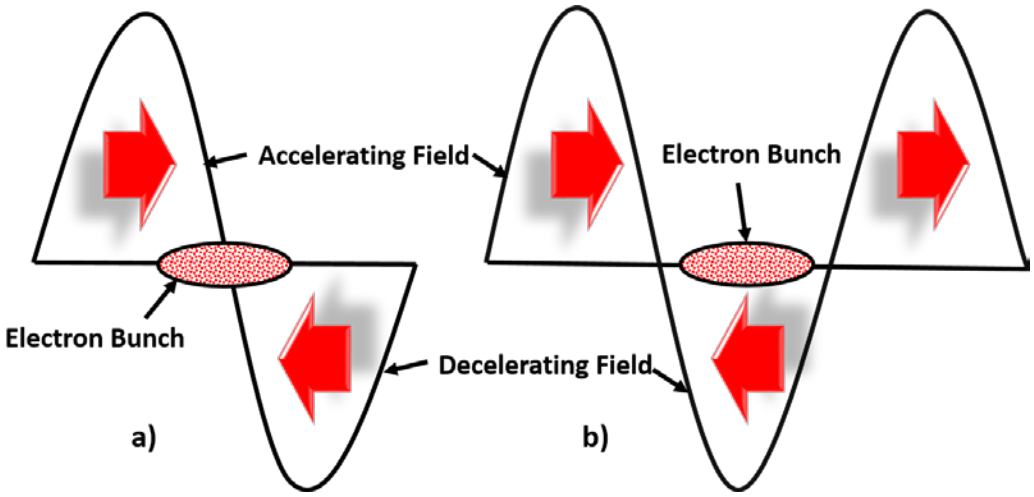

Figure 2.11 Electron bunch formation and energy extraction from an electron beam beam when a) the electron beam enters the interaction region, and b) after the interaction has occurred.

Another important phenomenon after forming the electron bunch that needs to be mentioned is saturation. When the decelerated electrons enter the accelerating field region, each accelerated electron in the bunch starts giving up its energy to the growing wave. Eventually, with time, the wave becomes equal to the supplied energy and stops growing. This point is called saturation, which is when the amplitude of the signal reaches its maximum. There are two main reasons that lead to saturation: 1) electron oscillations move out of resonance and excess kinetic energy of electrons is exhausted, or 2) trapping of electron bunches that start absorbing the energy from wave [1]. The saturation regime can be shown as in Figure 2.12.

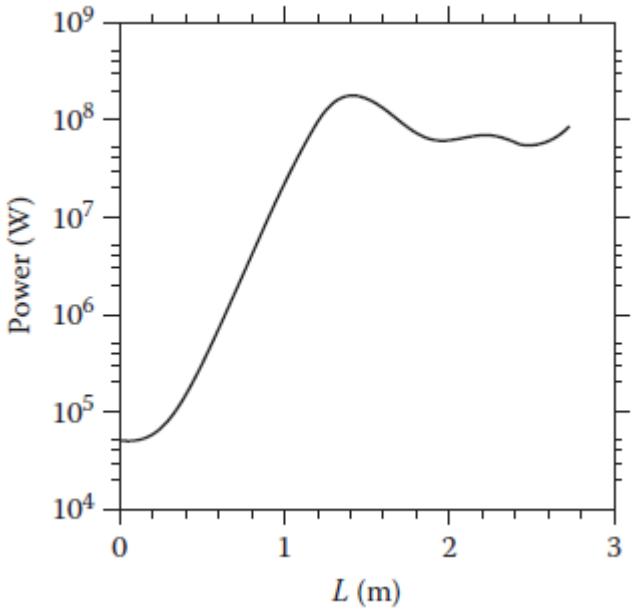

Figure 2.12 Plot of power with the interaction region that shows the microwave signal reaches saturation after growth of microwave signal [1].

It is possible to describe a TWT using a transmission line model that includes distributed inductances and capacitances per unit length, as shown in Figure 2.13 with beam current I_z.

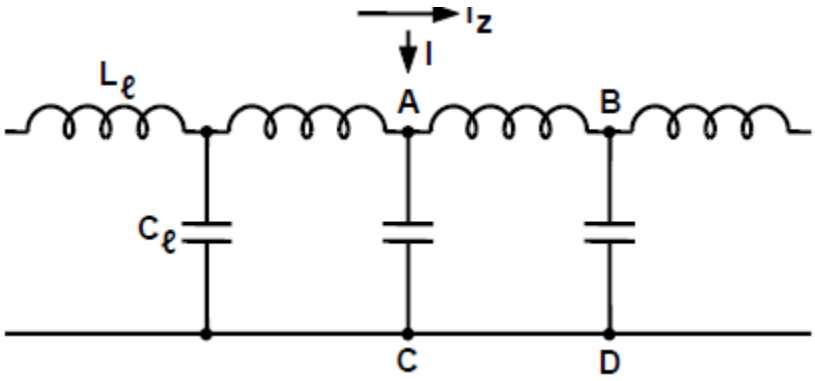

Figure 2.13 Transmission line model of a TWT [7].

The phase velocity and the impedance of the transmission line circuit without an electron beam $I_z = 0$ can be written as

$$v_p = \left(\frac{1}{L_l C_l}\right)^{1/2} \text{ and } Z_0 = \left(\frac{L_l}{C_l}\right)^{1/2}; \tag{2.38}$$

moreover, other circuit quantities, such as propagation constants are given by

$$\beta^2 = \beta_c^2 = \omega^2 L_l C_l \text{ and } \omega L_l = \beta_c Z_0. \tag{2.39}$$

From these equations, one can derive the longitudinal component of the electric field [7]

$$E_z = j\frac{\beta^2 \beta_c Z_0}{\beta^2 - \beta_c^2} I_z. \tag{2.40}$$

There are some other TWT designs that may achieve higher power levels that might also improve the performance compared to a helix structure. A ring bar or ring loop TWT, which is also a form of helix structure, is shown in Figure 2.14.

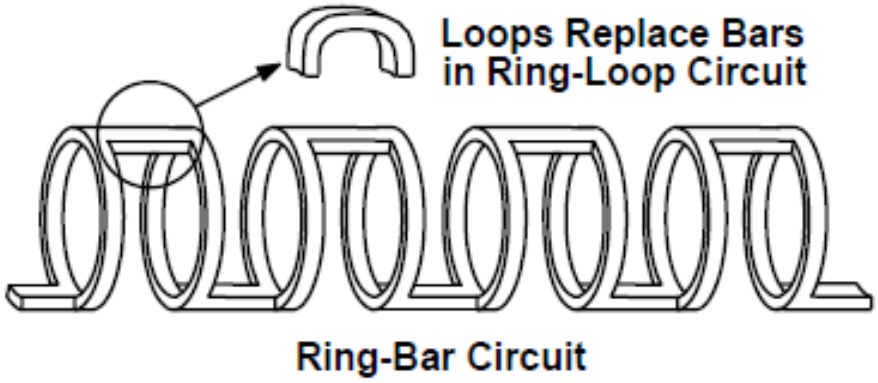

Figure 2.14 Ring bar and ring loop TWT design [7].

One of the significant advantages of this design is ease of fabrication compared to a helix. Besides, they are useful for suppression of oscillations and can be operated at higher voltages. This is achieved when accelerating and decelerating forces cancel one another, not allowing for net gain that creates parasitic backward wave oscillations. Because of their design, it is also possible to operate them with higher beam current and larger electron beams. However, bandwidth gets narrower because of design trade-offs. Chodorow and Chu [17] described this design for the first time in 1955. The dispersion diagram of a ring bar structure was investigated by LeBorgne [18] and is shown in Figure 2.15. There is a relatively recent paper which also describes progress in ring bar structure development [19].

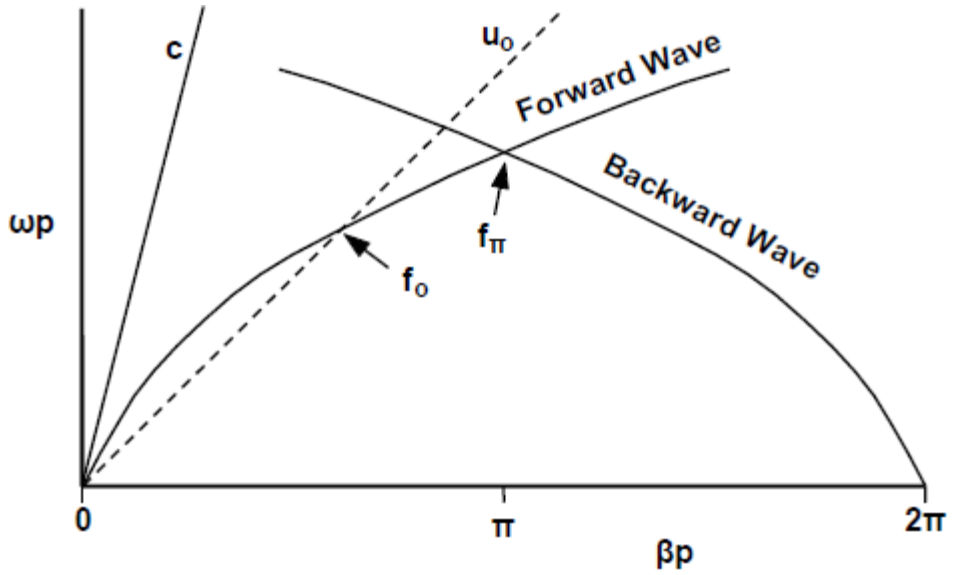

Figure 2.15 Dispersion diagram of a ring-bar structure [18].

At the point where the electron beam line intersects with the forward wave mode in the dispersion diagram, beam/wave synchronism occurs. At the point f_π a backward wave cannot be excited because the voltage during the synchronism is high. It should be mentioned that the phase velocity of the structure is characterized by the length and width of the bar or the loop.

2.5.2. BWO

After the invention of the TWT during WWII, researchers Kovalev et al. from the Lebedev Institute in Moscow in 1973 [4] and Carmel et al. from Cornell University in 1974 presented the relativistic BWO concept for HPM generation, driven by relativistic electron beams with high current [6].

When group velocity and power flow become negative with respect to the direction of electron beam propagation (since group velocity and energy velocity are related to each other) the device operates with a beam that is anti-parallel to power flow and is called a

BWO. Since the direction of wave propagation is reversed, the beam line intersects the dispersion diagram at a point where the group velocity of the mode is negative. The dispersion diagram for a vane-loaded waveguide BWO is given in Figure 2.15. A forward wave interaction occurs when the electron velocity is reduced and the wave travels to the other side, and the beam line intersects with the wave at point 2 in Figure 2.16 b). There are two main differences between amplifiers and oscillators: the wavenumber is defined by the waveguide and determines the interaction for an amplifier, but it is defined by cavities for an oscillator. Moreover, the wave amplitude changes in space; however, it is constant for a given location in an amplifier. In oscillators, the wave amplitude becomes constant in space since the structure provides feedback to the input port.

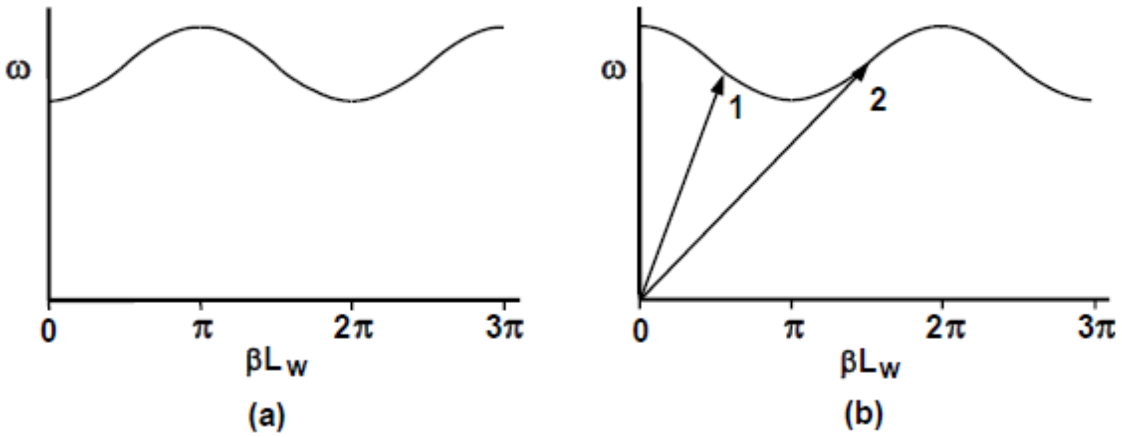

Figure 2.16 Dispersion diagram of a) a vane-loaded waveguide and b) the intersection of the electron beam line with the dispersion diagram [7].

To make the operating characteristics of a BWO more clear, two common models – the staggered slot and aligned slot structures will be presented here. These two models were proposed by Gittins in 1965 [20] and are shown in Figure 2.17. The dispersion diagram of the staggered slot structure is shown in Figure 2.18. Two propagating modes are shown in the dispersion diagram. These modes are called “cavity passband” because

they are controlled by the cavity resonance for the lower order mode and “slot passband” because it is controlled by the slot resonance for the higher order mode. Here the parameters were derived from the transmission line circuit model of the structure, and more detailed analysis is given in [7]. The most important parameters for this particular structure that affect the dispersion diagram are the coupling coefficient (k), slot inductance (k_c), slot resonance frequency (ω_s), and coupling slot angle (θ).

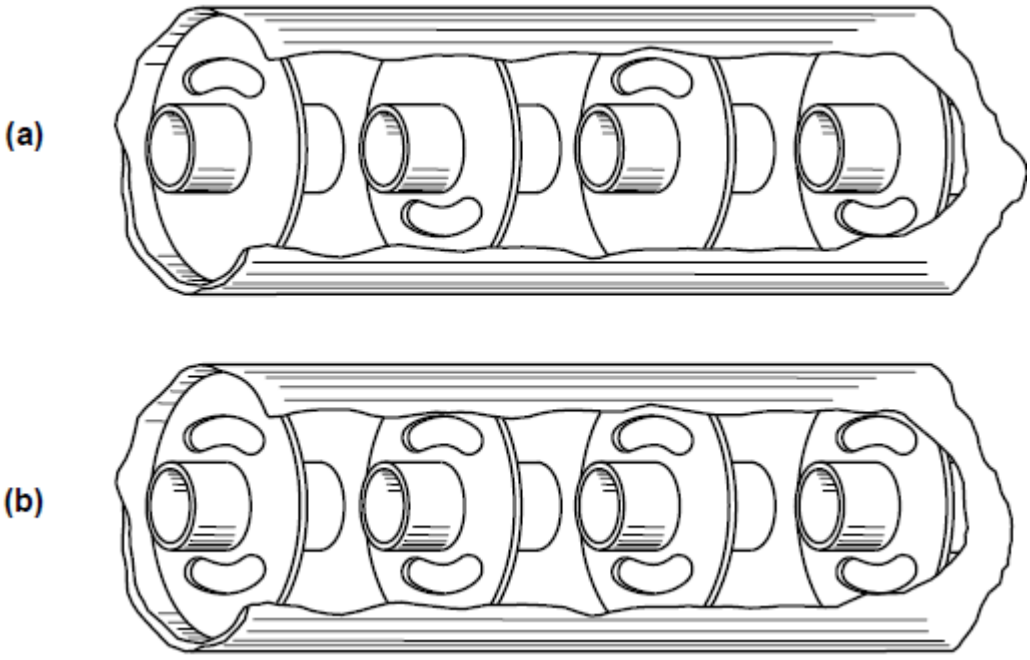

Figure 2.17 BWO design examples. a) Staggered slot and b) aligned slot structures [20].

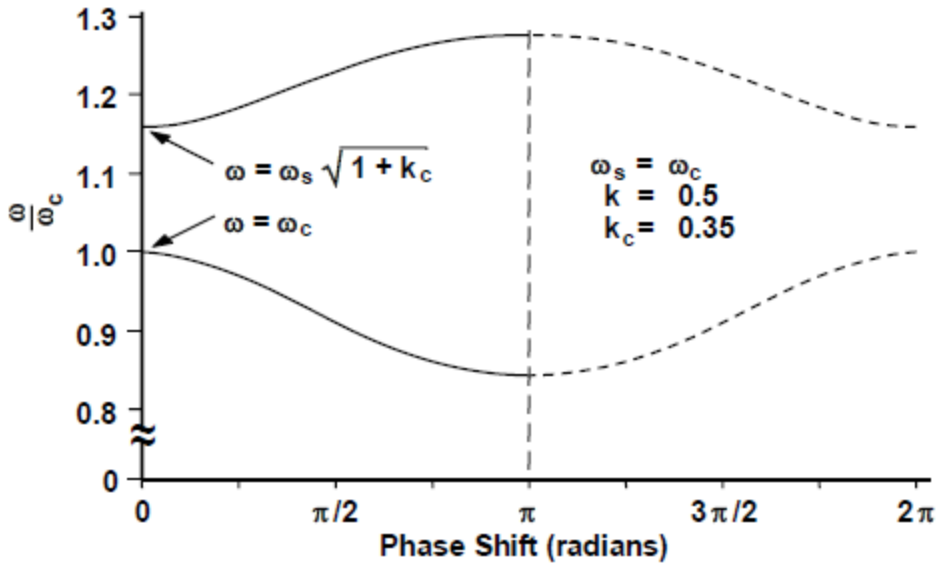

Figure 2.18 Dispersion diagram for a staggered slot structure [7].

For the aligned slot structure, current flowing around the cavity couples to the adjacent cavities as well. This leads to some operational changes compared to the staggered slot structure. It can allow higher powers but with a smaller bandwidth than staggered structures. An efficiency of 30% has been achieved with this structure.

Thus, the BWO design process can be summarized as follows [1]:

- In order to define the operating frequency and electromagnetic characteristics, the SWS should be simulated with a software package that allows for computational electromagnetic measurements without considering the electron beam (cold measurements). With the presence of a beam, PIC simulations should be performed in order to determine the beam parameters such as beam current, the energy of the electrons, and their distribution.
- For an oscillator, threshold condition needs to be satisfied in order for oscillations to begin. This parameter is known as the *start current* and depends on the length and radius of the SWS, the reflection coefficient, and smoothness or shape of the wall that

causes perturbations. The start current is an important parameter because for proper operation the beam current has to exceed it (by a factor of 2-3) and it might lead to instabilities if the beam current is more than 5-6 times the start current. Thus, BWOs can operate as amplifiers below their start current.

- The magnetic field strength is an another important parameter that needs to be optimized. The magnetic field strength must be sufficient to guide the beam, but should not be so strong that cyclotron resonance would occur, whereby oscillations would cease. (Cyclotron absorption is often used in overmoded BWOs to suppress higher order modes.)
- The goal after PIC simulations is to have an output power of the oscillator or amplifier that saturates with time that is shorter than the pulselength of the accelerator.
- Before verifying the structure experimentally, axial extraction of microwave power after the beam dump needs to be considered. Coupling of the output mode can be predicted by computer simulations. For BWOs, the most common output modes are TM_{01}.

Although phase and frequency controls are relatively complicated for high power amplifiers, high power BWOs can be more compact and could be easier to design. In some BWOs it is possible to achieve output powers that may be several gigawatts [21, 22].

2.6. Beam–Wave Interaction in Slow-Wave Structures

When the electron beam is included in the system, Maxwell's equations become nonlinear. Interception of the electron beam line with the dispersion diagram determines the output, to first order. The effect of electron cyclotron waves on beam/wave interaction is determined by the strength of the guide magnetic field. The kinetic energy of electrons

$(\gamma_{\mathrm{b}} - 1)mc^2$, the electron beam current $\mathrm{I_b}$, and the radius of the beam are the main parameters that determine the beam/wave interaction and microwave generation for a given SWS.

The beam line that needs to be added to the dispersion diagram is given as

$$\omega = k_n v_{\mathrm{b}} = (k_z + nh_0)v_{\mathrm{b}}. \tag{2.41}$$

The beam line intersects with a mode that propagates through the system and helps to define system operation as either an amplifier when it intersects with a forward wave or an oscillator when it intersects with a backward wave. For a thin annular electron beam, its effect on the dispersion diagram is given by the space charge factor α given by [1]

$$\alpha = \frac{\pi I_{\mathrm{b}}}{\beta_{\mathrm{b}} I_{\mathrm{A}} \gamma_{\mathrm{b}}^3} \tag{2.42}$$

where $I_{\mathrm{A}} = 17.1$ kA is the Alfvén current and β_{b} is the normalized electron beam velocity. When γ_{b} increases α decreases dramatically.

There are several approximations that yield an analytic model of beam/wave interaction in microwave devices such as the Pierce-like theory for semi-infinite structures that is commonly used for TWTs, the macro-particle approach that uses a large number of electron clusters instead of the hydrodynamic (single fluid flow) approximation, or a unified approach for amplifiers and oscillators which allows for calculations of relativistic devices, as described in detail in [13].

Beam/wave interaction will be investigated here with the example of a dielectric-filled waveguide as a TWT because of its relative simplicity, in addition to a BWO.

Interaction Mechanism of a Dielectric-Filled Waveguide TWT

The dispersion relation for a dielectric-filled waveguide for the TM_{01} mode and without presence of a beam is given by

$$k_1^{(0)} = \sqrt{\frac{\varepsilon_r \omega^2}{c^2} - \frac{J_{01}^2}{R^2}} \tag{2.43}$$

where k is the wavenumber, J_{01} is the zero of the Bessel function of the first kind of order zero, and R is the waveguide radius. In the presence of a beam the solution of the dispersion relation is

$$k_1 = k_1^{(0)} + \delta k. \tag{2.44}$$

With some assumptions one can obtain the following simplified dispersion relation

$$\delta k(\delta k - \Delta k)^2 = -K_0^3 \equiv -\frac{1}{2}\frac{J_{01}^2}{R^2}\frac{\omega_p^2}{\varepsilon_r k_1 v_0^2 \gamma^3} \tag{2.45}$$

where $K_0$is the coupling coefficient. This type of dispersion relation was presented by Pierce in 1947 for a helix structure with a nonrelativistic electron beam. For this reason it is called Pierce's approach. Solution of this third order polynomial equation at resonance when the electron beam is synchronous with the electromagnetic wave is given by [13],

$$\delta k_1 = -K_0, \;\; \delta k_2 = K_0\left(\frac{1}{2} - \frac{j\sqrt{3}}{2}\right), \;\; \delta k_3 = K_0\left(\frac{1}{2} + \frac{j\sqrt{3}}{2}\right). \tag{2.46}$$

This solution shows three waves that propagate in the forward direction. The longitudinal component of the electric field is written by

$$E_z(r, z, \omega) = J_0\left(J_{01}\frac{r}{R}\right)e^{-jk_1 z}\left[E_1 e^{-j\delta k_1 z} + E_2 e^{-j\delta k_2 z} + E_3 e^{-j\delta k_3 z}\right]. \tag{2.47}$$

Moreover, the gain G is proportional to the E_z field

$$G \equiv \frac{|E(0)|}{|E(d)|} \cong \frac{1}{3}\left|e^{3jK_0\frac{z}{2}} + e^{-\sqrt{3}K_0\frac{z}{2}} + e^{\sqrt{3}K_0\frac{z}{2}}\right|. \tag{2.48}$$

Interaction Mechanism of a BWO

In order to understand the interaction mechanism for a BWO we consider the input at $z = d$ and the output at $z = 0$. The coupling coefficient K_0^3 can be formulated depending on energy velocity β_{en}, particle momentum $\gamma\beta$, cross section of wave propagation $S_w = \pi R^2$, and the current which flows inside the waveguide $I = en_0 v_0 \pi R^2$ for an electron beam that interacts with the TM mode [13]

$$K_0^3 = \frac{1}{2}\frac{1}{S_w}\frac{\omega}{c}\frac{eI\eta_0}{mc^2}\frac{1}{(\gamma\beta)^3}\frac{1}{\varepsilon_{\text{int}}\beta_{\text{en}}}. \tag{2.49}$$

Since energy velocity and phase velocity are antiparallel for a BWO, we will consider β_{en} and K_0^3 as negative. The dispersion relation for a BWO is derived in [13] and is given by

$$\delta k(\delta k - \Delta k)^2 = K_0^3. \tag{2.50}$$

Here K_0^3 has the opposite sign for an amplifier. Solution of the dispersion relation for the three modes can be written as

$$\delta k_1 = K_0, \;\; \delta k_2 = -K_0\left(\frac{1}{2} - \frac{j\sqrt{3}}{2}\right), \;\; \delta k_3 = -K_0\left(\frac{1}{2} + \frac{j\sqrt{3}}{2}\right). \tag{2.51}$$

Additionally, the longitudinal component of electric field E_z can be derived as [13]

$$E_z(r, z, \omega) = J_0\left(\mathrm{p}_1\frac{r}{R}\right)e^{-jk_1(z-d)}[E_1 e^{-j\delta k_1(z-d)} + E_2 e^{-j\delta k_2(z-d)} + E_3 e^{-j\delta k_3(z-d)}. \tag{2.52}$$

At the input $z = d$, $E_1 + E_2 + E_3 = E_0$ and is called the initial amplitude. At the output where $z = 0$, the third solution (mode) of the dispersion diagram becomes dominant, and gain is given by

$$G \equiv \frac{|E(0)|}{|E(d)|} \cong \frac{1}{3}\, e^{\sqrt{3}K_0\frac{d}{2}}. \tag{2.53}$$

Since there is feedback in the system that is not dependent on the load impedance for the interaction the BWO device is less sensitive to the load than an amplifier.

The interaction impedance was defined previously in Equation 2.21; it is the parameter that plays an important role in beam/wave interactions for periodic microwave structures. Here it will be given as an explicit expression for periodic structures. Considering a pencil beam with beam radius R_{b}, the electric field is

$$|E|^2 = \frac{2}{R_{\mathrm{b}}^2}\int_0^{R_b} \left|E_{z,n=0}(r,z)\right|^2 dr\,. \tag{2.54}$$

The expression for E_z is derived in [13] for a periodic structure with corrugations that have parameters period L, inner radius R_{in}, outer radius R_{ext}, and distance between cavities d. Equation 2.54 can then be written again as

$$|E|^2 = \frac{c^4}{\omega^2}\,|A_0|^2\Gamma_0^4\frac{2}{R_{\mathrm{b}}^2}\int_0^{R_{\mathrm{b}}} I_0^2(\Gamma_0 r)dr. \tag{2.55}$$

After solving this integral, the definition of interaction impedance for periodic structures is given as [13]

$$Z_{\mathrm{int}} = \frac{1}{2}\frac{|E|^2(\pi R_{\mathrm{int}}^2)}{P} = \eta_0\left(\frac{R_{\mathrm{int}}}{R_{\mathrm{b}}}\right)^2\left(\frac{c\Gamma_0}{\omega}\right)^2 W_1(\Gamma_0 R_b)\left[\sum_{n=-\infty}^{\infty} U(\Gamma_n R_{\mathrm{int}})\left(\frac{ck_n}{\omega}\right)\frac{|A_n|^2}{|A_0|^2}\right]^{-1} \tag{2.56}$$

where the ratio $\frac{|A_n|^2}{|A_0|^2}$ is related to the solution of the dispersion relation and the full solution is given in [13]. From this expression, it can be pointed out that the interaction impedance increases gradually with beam radius and decreases with increasing radius of the structure.

Furthermore, for the interaction in O-type devices, space-charge wave oscillations on an electron beam can be interpreted by considering a long and large electron beam that is confined in the z direction by a strong magnetic field. Oscillations are created by the space-charge forces between the electrons in an electron bunch which occurs when

electrons are squeezed into one area. Thus, the oscillation frequency and wavenumber of the oscillations are related and given by [1],

$$\omega = k_z v_z \pm \frac{\omega_{\mathrm{b}}}{\gamma_0}. \tag{2.57}$$

Here $\omega_{\mathrm{b}} = \sqrt{n_{\mathrm{b}} e^2/\varepsilon_0 m \gamma_{\mathrm{b}}}$ is the beam plasma frequency where n_{b} is the beam electron density, γ_{b} is the relativistic factor, and v_z is the electron velocity. It is, in fact, the slow space-charge wave on the electron beam that actually interacts with the electromagnetic mode on the dispersion diagram.

2.7. Design Limitations and Issues

Several limitations and problems have been encountered by researchers over the years in the design of O-type Cerenkov devices. Limitations related to physics or technology that have been commonly faced include the size, volume, and power handling capability of the structure; the axial magnetic field; pulse shortening when long pulse operation is required; and operation in repetitively-pulsed mode. Other limitations related to the system include mobility of the system and requirements for specific applications. These restrictions affect the output power, energy of the pulse, and overall efficiency of the structure.

Limitations in size are mostly related to the frequency of operation. If the radius or cross-section of a device increases, the frequency will decrease and vice versa. Increasing size will also affect other beam parameters. It could improve the ability to overcome the breakdown problem and quality of beam confinement. On the other hand, it may cause overmoded operation which requires a strategy to mitigate unwanted higher order modes.

The guide magnetic field is another parameter that sets limitations in the structure's overall weight, size, or power requirements. If the amplitude of the guide magnetic field decreases, it will reduce the size and weight of the overall system because of requiring fewer magnets and smaller power supplies. However, a strong guide magnetic field is required for many HPM applications, such as for the NAGIRA (Nanosecond Gigawatt Radar) system [1].

In addition to the limitations above, there are some others that can be mentioned here briefly. Having a low or high impedance might cause other issues or limitations related to the matching problem with a pulsed power source. Increasing the beam current to increase the output power can cause instabilities related to overbunching of electrons.

One of the most commonly faced and least understood issue in HPM devices is electrical breakdown within the SWS that could cause failure and limit the power handling capability of devices. The breakdown characteristics of vacuum limit the current density that is drawn from a cathode. The vacuum breakdown limit is given as about 100 kV/cm, so breakdown occurs after this threshold field is exceeded for a 1 cm gap with a uniform magnetic field and potentials above 100 kV. This can occur in several regions of the HPM source, including between electrodes in an electron gun, in the collector region, or inside the microwave SWS or other RF elements that is exposed to the high power (Figure 2.19). The breakdown fields of some commonly used media are: gas (10 V/cm-100 kV/cm), vacuum (50-300 kV/cm), liquid (0.5-1 MV/cm) or solid (0.5-1 MV/cm) [7].

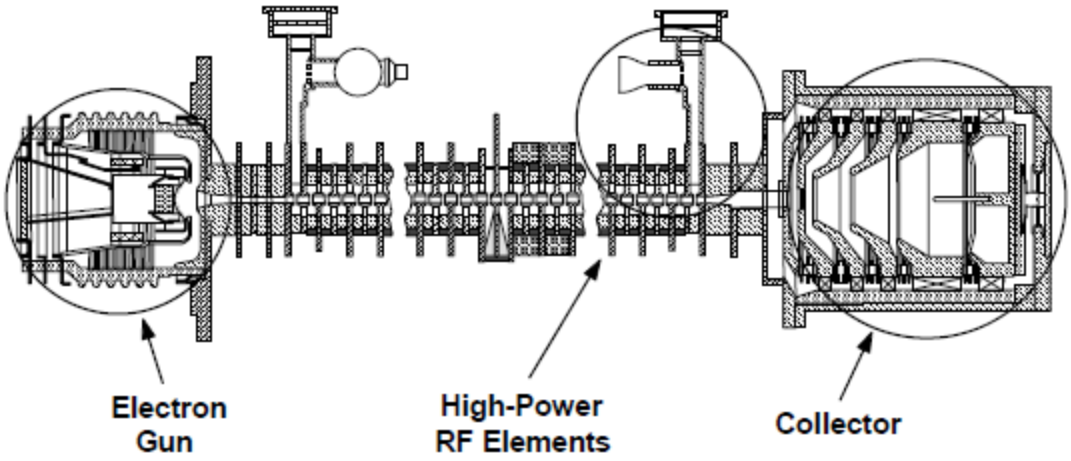

Figure 2.19 Possible regions that may suffer from electrical breakdown [7].

2.8. Introduction to Metamaterials

"Metamaterials are macroscopic composites having man-made, three-dimensional, periodic cellular architecture designed to produce an optimized combination, not available in nature, of two or more response to specific excitation." This was coined by Rodger Walser of the University of Texas – Austin in 1999 [23]. In this dissertation we use the term metamaterials to denote artificially structured composite materials which simultaneously possess negative permittivity ε and negative permeability μ. Metamaterials are often described as consisting of subwavelength resonant structures that can produce an electromagnetic behavior not typically available in nature and they exhibit unusual physical properties such as:

- Negative index of refraction
- Anti-parallel wavevector and Poynting vector
- Anti-parallel phase and group velocities
- Time-averaged energy flux opposite to the time-averaged momentum density.

Moreover, their other properties are:

- Period much less than operational wavelength
- Negative dispersion (reversed Cerenkov radiation)
- Inverse doppler effect
- Negative Goos–Hanchen shift.

Metamaterials are also called left-handed materials (LHM) or negative index materials (NIM). In 1968, Vesalago studied simultaneously negative ε and μ phenomenon for the first time in his paper [24]. Following nearly three decades later, Pendry designed a composite material that can produce negative effective permittivity in microwave frequencies in 1996 [25]. He used a periodic collection of metallic rods that behaves like a plasma medium when the electric field vectors are properly oriented. He showed that there is negative permittivity below the plasma frequency, depending on the rods' dimensions. After that he worked on developing negative permeability media using an array of Swiss roll capacitors as a magnetic resonant structure [26]. Most of today's metamaterial designs are based on his cylinder design, which is called a split ring resonator (SRR).

In 2000, Smith et al. established a design procedure for artificial bulk media with negative constitutive parameters at microwave frequencies [27]. The first design consisted of SRRs printed on a dielectric substrate and rods that are printed on it and parallel to the SRRs. This procedure makes use of a system of metallic wires and/or plates to obtain the negative dielectric permittivity, and an SRR is used to obtain the negative magnetic permeability. Since these metamaterials are expected to be highly anisotropic and have lossy behavior, much research has been performed in order to characterize them.

The first experimental demonstration was carried out by Shelby et al. wherein they placed the metamaterial structure in a parallel-plate waveguide [28]. They observed a negative refraction at around 10 GHz by launching an X-band microwave beam into one end of the waveguide. They observed an angular radiation pattern of the transmitted beam that was refracted by the prism's slanted side.

Metamaterials have been widely used in many microwave devices, such as in amplifier, filters, phase shifters for broadband applications, directional couplers, and power dividers. They have also been used for antenna miniaturization, as superlenses (super-resolution medical and optical imaging and nondestructive detections), beam bending or beam focusing lenses, photonic crystals, cloaking devices, polarizers, and more [29-31]. In addition to them, there is recent growing interest in using metamaterials for improving the performance of vacuum electron devices which is also the subject of this dissertation.

There are some retrieval methods defined for extraction of constitutive material parameters such as ε, μ, index of refraction n and impedance Z using reflection and transmission coefficients of S-parameters. These will be reviewed in detail in this chapter.

2.8.1. Theory and Fundamentals

Negative dielectric constant or negative magnetic permeability phenomena have long been known in electromagnetics [32]. The Drude – Lorentz model is suitable for predicting numerical values of permittivity and permeability and characterizing wire media with periodic cuts in classical electromagnetics [33]. If we consider a plane wave that propagates in an isotropic, homogeneous medium, Maxwell's equations can be written for

the conditions of no free charges (ρ) and currents (j) using the electric and magnetic components of the plane wave as

$$\boldsymbol{E}(\omega, k) = \boldsymbol{E_0} \exp(i\boldsymbol{k} \cdot \boldsymbol{r} - i\omega t) \tag{2.58}$$

$$\boldsymbol{H}(\omega, k) = \boldsymbol{H_0} \exp(i\boldsymbol{k} \cdot \boldsymbol{r} - i\omega t) \tag{2.59}$$

where ω is the angular frequency and k is the wavenumber. Maxwell's equations in the sinusoidal steady state are given as

$$\nabla \times \boldsymbol{E} = -j\omega\mu\boldsymbol{H} \rightarrow \quad \boldsymbol{k} \times \boldsymbol{E} = \omega\mu\boldsymbol{H} \tag{2.60}$$

$$\nabla \times \boldsymbol{H} = -j\omega\varepsilon\boldsymbol{E} \rightarrow \quad \boldsymbol{k} \times \boldsymbol{H} = -\omega\varepsilon\boldsymbol{E}. \tag{2.61}$$

These equations are the basic representation of right handed media since a plane wave propagates in traditional dielectric materials with $\varepsilon > 0$ and $\mu > 0$. For left-handed media these vectors can be written for materials with $\varepsilon < 0$ and $\mu < 0$ and the Poynting vector, which is $\boldsymbol{S} = \boldsymbol{E} \times \boldsymbol{H}$, becomes antiparallel to the wavevector $\boldsymbol{k}$. Moreover, the refractive index takes a negative sign because of the expression $n = \pm\sqrt{|\varepsilon_r||\mu_r|}$. Therefore, Maxwell's equations are written again for left-hand media as

$$\boldsymbol{k} \times \boldsymbol{E} = -\omega|\mu|\boldsymbol{H} \tag{2.62}$$

$$\boldsymbol{k} \times \boldsymbol{H} = \omega|\varepsilon|\boldsymbol{E}. \tag{2.63}$$

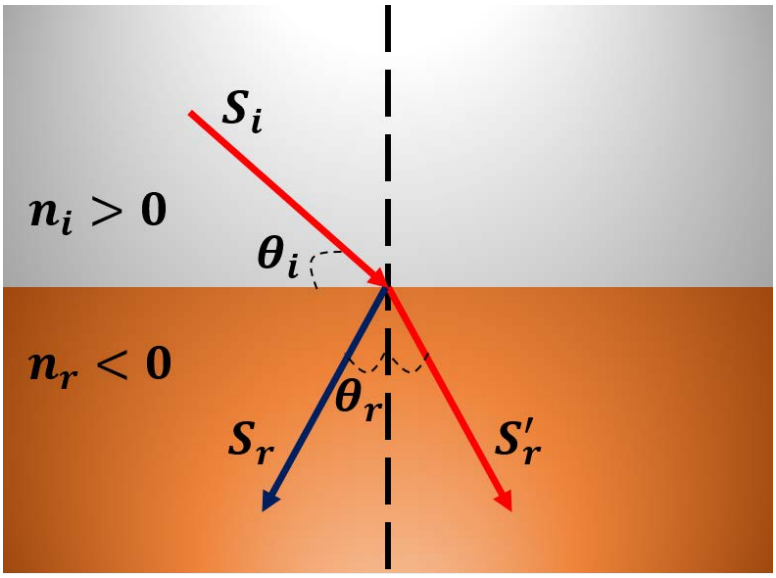

Figure 2.20 Illustration of negative refractive index antiparallel to the Poynting vector.

We know from Snell's law that the angle of refraction is negative when the refractive indices of two materials have opposite signs, as shown in Figure 2.20. The Drude – Lorentz model is written as

$$\varepsilon(\omega) = 1 - \frac{\omega_p^2 - \omega_{0e}^2}{\omega(\omega + j\Gamma_e) - \omega_{0e}^2} \tag{2.64}$$

$$\mu(\omega) = 1 - \frac{F\omega^2}{\omega(\omega + j\Gamma_m) - \omega_{0m}^2} \tag{2.65}$$

where ω_p is the plasma frequency, ω_0 is the resonant frequency, Γ is the damping factor related to material losses, subscripts "e" and "m" refer to epsilon and mu, respectively, and F is the filling ratio of the SRR. Using this model, one can explore the left-handed region of the medium.

Effective electric permittivity (ε_{eff}) and magnetic permeability (μ_{eff}) are the two fundamental parameters that characterize the electromagnetic properties of a medium. In

principle, they describe how an electric or magnetic field affects or is affected by a medium which is determined by the material polarization in response to an electric or magnetic field.

Using Faraday's law, one can generate a current loop, like the orbital current comprising magnetic dipoles in magnetic material, by applying a magnetic field through a conducting coil. The magnetic moment and induced current can be enhanced by introducing resonances in the coil. Pendry's SRR is one of the first designs that can produce negative permeability.

2.8.2. Basic Metamaterial Structures

Pendry et al. for the first time proposed a structure using the concept of Veselago with extremely low plasma frequency in a three-dimensional form of a thin metallic wire lattice, as shown in Figure 2.1 (a). Simultaneous negative permittivity and negative permeability were proposed and proven by Smith and Pendry with a structure that consists of two split rings and wires which are shown in Figure 2.21 (c). These SRRs are usually used to form macroscopic periodic cells, as shown in Figure 2.22.

SRRs are composed of two split rings that are placed 180° out of phase in an edge coupled form as illustrated in Figure 2.21 (c), (d), and (f). It can be considered as an LC circuit that has a resonant frequency $\omega_0 = 1/\sqrt{LC}$ with L and C representing the geometric inductance and capacitance of the SRR structure, respectively [34]. Because of the gaps in the SRR structure, a circulating current will build up a charge across the gap with energy stored as in a capacitor [35]. The gaps are the main capacitive region in which charge is concentrated, and a stronger surface current density has been found in the continuous SRR

branch which is opposite to the one bearing the gap. In [35, 36] it was also shown that having more than one gap in the SRRs leads to increasing magnetic resonant frequency.

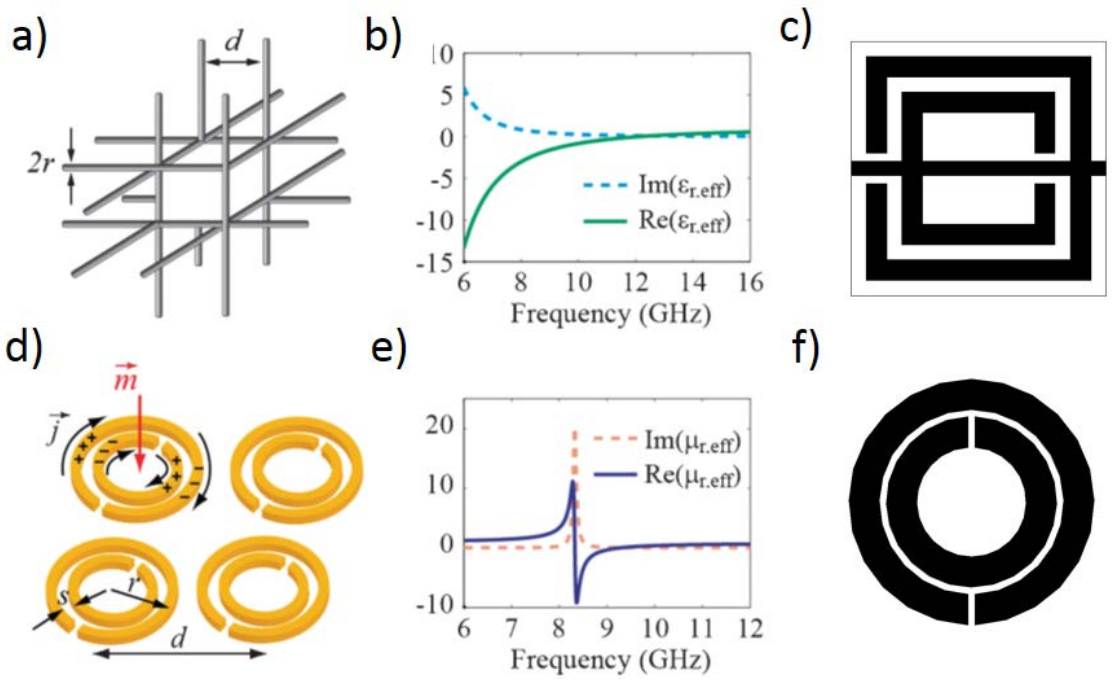

Figure 2.21 Edge-coupled SRRs (EC-SRRs) [25-27]: a) wire conductors, b) effective permittivity plot, c) rectangular SRR structure, d) circular SRR with charge orientation, e) effective permeability plot, and f) circular SRR structure.

The SRR can induce a strong orbital current when magnetic flux is applied to it in a certain frequency range which results in an effective magnetic moment. An external magnetic field changes the phase of this induced magnetic moment and when it is strong, it can produce negative effective permeability within this frequency range [37].

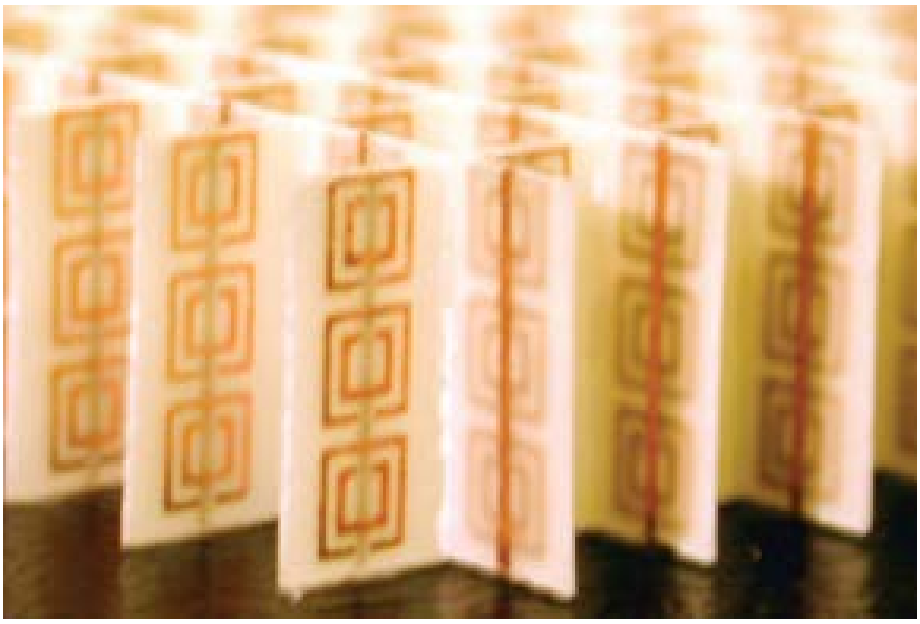

Figure 2.22 Bulk SRR metamaterial [28].

Negative responses to the electric component of light have been known for a long time. Metals at their plasma frequency at which they become transparent produce negative permittivity. With consideration of Pendry's wire design, since the effective density can be reduced depending on the number of thin wires used, which also increases the effective mass of the charge, the effective plasma frequency can be decreased.

Using these two fundamental concepts, researchers proposed a medium with simultaneously negative permittivity and permeability within a certain microwave frequency range. However, the resonant frequency of the SRR structures is highly sensitive to the capacitance of the rings and the dielectric constant of the substrate [34].

It has been found that coupling along the electric field direction results in a shift of the magnetic resonant frequency depending on the strength of the current and amount of charge. The upward shift occurs when there is a strong current between the SRRs that is due to the inductive interaction of SRRs. Similarly, the downward shift occurs when there

is a strong charge concentration that is due to the capacitive interaction between the rings [35].

There is also a common belief that the magnetic resonance of the SRRs can only be excited through the magnetic field component of an electromagnetic wave [38]. It is also assumed that the magnetic resonance occurs only with external magnetic field perpendicular to the SRR plane and with direction of propagation parallel to the SRR. Contrarily, it was shown in [39] that the electric coupling of the incident electromagnetic wave to the magnetic resonance of the SRR occurs even if the incident magnetic field is parallel to the SRRs and the direction of propagation is perpendicular to the SRR plane, as shown in Figure 2.23**.**

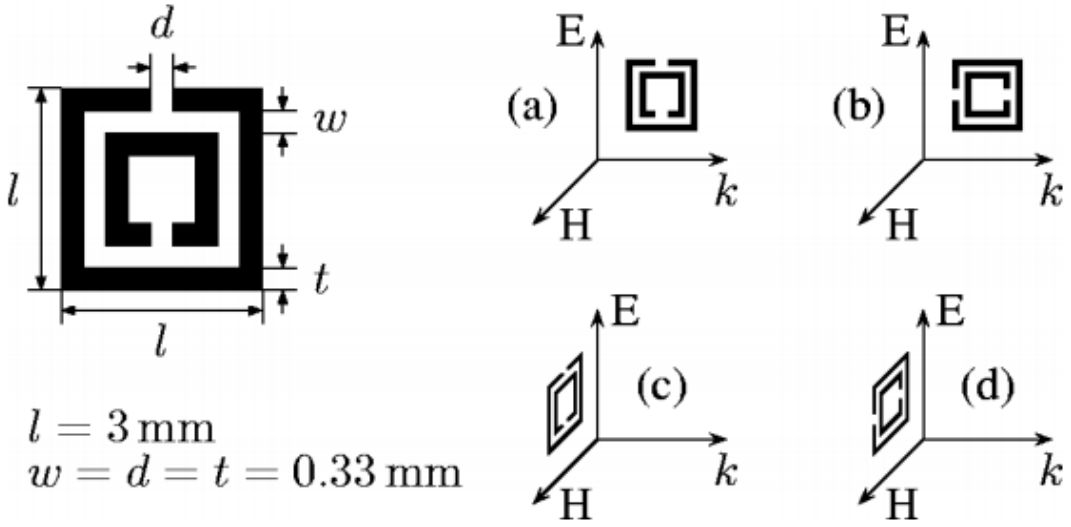

Figure 2.23 Different configurations of electric and magnetic fields incident onto an SRR [39].

Metamaterials are formed as periodic structures with repeated unit cells. They can be modeled by simulating the properties of a single unit cell and applying various forms of periodic boundary conditions using full wave electromagnetic simulation tools such as

HFSS, CST, or COMSOL. These results provide good qualitative agreement with experimental measurements.

2.8.3. SRR-Loaded Waveguides

The main property of metamaterial-loaded waveguides is below cutoff propagation for the selected mode or dominant mode. Since metallic waveguides can support TE and TM modes, they satisfy the expression

$$k = \omega\sqrt{\mu_0 \varepsilon_{\text{eff}}} \tag{2.66}$$

where k is the propagation constant, ω is the angular frequency, μ_0 is the magnetic permeability of free space and ε_{eff} is the effective dielectric constant given by

$$\varepsilon_{\text{eff}} = \varepsilon_0 \left(1 - \frac{\omega_c^2}{\omega^2}\right). \tag{2.67}$$

Here ω_c is the cutoff frequency of the mode and ε_0 is the permittivity of free space [40].

Electromagnetic transmission below cutoff frequencies occurs in the region of frequency where permittivity and permeability are both negative. In [40] an experimental reference model of a metamaterial-loaded waveguide was given. SRRs are placed partially out of the waveguide to be able to excite the first and last rings of the structure, as illustrated in Figure 2.24. After the SRRs are inserted into the waveguide the S-parameters can be measured using a network analyzer in order to be able to analyze the behavior of the system.

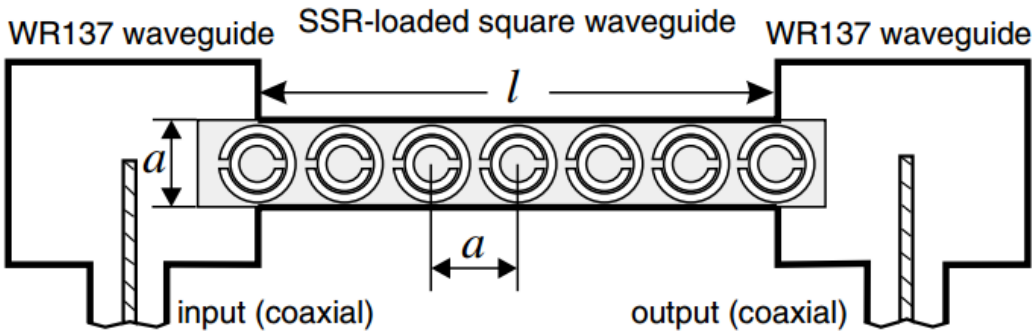

Figure 2.24 Sketch of Marques's experimental setup [40].

In [41] the propagation constant equation is given for TE modes as

$$\gamma^2 = -\omega^2\mu_0\varepsilon_0\left(1-\frac{\omega_c^2}{\omega^2}\right)\left(1-\frac{\omega_p^2}{\omega^2}\right). \tag{2.68}$$

TE modes propagate at the frequencies where the terms in parenthesis have the same sign. A backward wave occurs when the frequency ω is less than ω_c and ω_p and vice versa for a forward wave.

Marques et al. proposed that if a set of elements capable of producing negative permeability is placed inside a below cutoff waveguide then the propagation characteristics will be the same as for a double negative media. Thus, a cutoff waveguide can be considered as a medium that has an effective negative permittivity. Propagation in such waveguides where the refractive index has negative values can be possible when the radius of the waveguide is small enough, and this leads to reduced dimension of the waveguide and the result is power compression [29, 40].

2.8.4. Main Properties of Metamaterials

Since metamaterials supposedly have unique properties such as negative refraction, backward wave propagation (opposite phase and group velocities), etc., allows them to control the propagation of electromagnetic waves.

Negative Refraction

A plane wave is partially reflected and partially refracted when it is incident upon a boundary. Using the expressions for the reflection and transmission coefficients, and the relationship between the reflection and refraction angles, one can solve Snell's law and determine whether or not negative refraction occurs. This negative refraction effect is beneficial for lenses and optics when wave focusing is needed for some applications.

Anti-parallel Wavevector and Poynting Vector

The time-average Poynting vector is given by,

$$\boldsymbol{S} = \frac{1}{2}\mathrm{Re}\,[\boldsymbol{E}\times\boldsymbol{H}^{*}], \tag{2.69}$$

where the asterisk denotes complex conjugate. From this equation, it can be seen that the time-average flux of energy and propagation vector are anti-parallel (Figure 2.25).

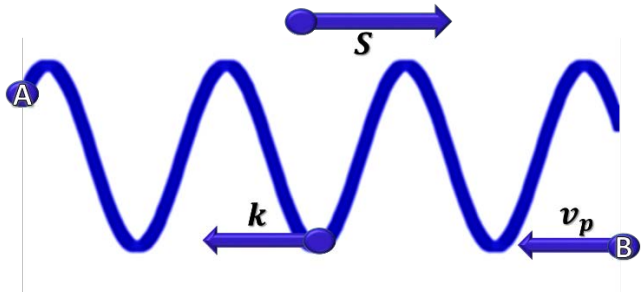

Figure 2.25 Reverse Cerenkov radiation in a left-handed medium.

Anti-Parallel Phase and Group Velocities

Since the wavevector is in the direction of phase velocity, left-handed media have negative group velocity. However, this phenomenon has long been used and known from the 1940s [32]. This behavior is one of the properties of metamaterials that has similarities with all-metallic SWSs that are used to produce backward waves.

Time-Average Energy Flux Opposite to the Time-Average Momentum Density

Since the time-average energy flux is related to the group velocity, which is negative, and the time-average momentum density is related to the wavevector, then the time-average energy flux and momentum density are opposite to one another

$$\langle \boldsymbol{S} \rangle = \langle u \rangle v_g \quad \text{and} \quad \langle \boldsymbol{p} \rangle = \frac{\langle u \rangle \boldsymbol{k}}{\omega} \tag{2.70}$$

where v_g is the group velocity $\partial\omega/\partial k$.

Backward Wave Propagation

The other unique property of left-handed materials is their ability to support backward waves which are waves whose power propagates in a direction opposite to their phase. The power flow direction can be shown using Maxwell's equations,

$$\boldsymbol{E} = \boldsymbol{p} e^{i\boldsymbol{k}\cdot\boldsymbol{r}} \tag{2.71}$$

$$\boldsymbol{H} = \frac{1}{\omega\mu}(\boldsymbol{k}\times\boldsymbol{p}) e^{i\boldsymbol{k}\cdot\boldsymbol{r}} \tag{2.72}$$

$$\langle \boldsymbol{S} \rangle = \frac{1}{2}\mathrm{Re}\,[\boldsymbol{E}\times\boldsymbol{H}^*] = \frac{1}{2\omega\mu}\boldsymbol{p}\times(\boldsymbol{k}\times\boldsymbol{p}) = \frac{\boldsymbol{k}}{2\omega\mu} \tag{2.73}$$

where, $\boldsymbol{p}\times(\boldsymbol{k}\times\boldsymbol{p}) = (\boldsymbol{p}\cdot\boldsymbol{p})\boldsymbol{k} - (\boldsymbol{p}\cdot\boldsymbol{k})\boldsymbol{k}$ and $\boldsymbol{p}\cdot\boldsymbol{k} = \boldsymbol{0}$ because of Gauss's law. When permittivity and permeability are both negative, this result shows that the Poynting vector will be in the opposite direction of the phase propagation vector [37].

Backward wave propagation also provides the well-known phenomenon of Cerenkov radiation which is used in some HPM source designs. The advantages of metamaterials are that they may lead to the development of new devices in the HPM field through the engineering of new dispersion relations that would not exist using conventional materials. It is known that backward waves can be produced by BWOs in conventional vacuum electronic systems. The differences and similarities between BWO SWSs and MSWSs will be discussed in detail in Chapter 3.

Inverse Doppler Effect

Anti-parallel directions of the Poynting vector and wavevector leads to the "inverse Doppler effect" in left-handed media. The Doppler frequency can be written as,

$$\omega_{D\text{oppler}} = \omega_0\left(1 - s\frac{v_s}{|v_p|}\right). \tag{2.74}$$

Negative Goos–Hanchen Shift

If energy flow is antiparallel to the direction of wavefront propagation, the Goos-Hanchen shift will be negative. This can be shown by considering the relation of the phase of the reflection coefficient with the parallel wavevector (Figure 2.26)

$$\Delta = \frac{\partial\varphi_r}{\partial k_{\text{parallel}}}. \tag{2.75}$$

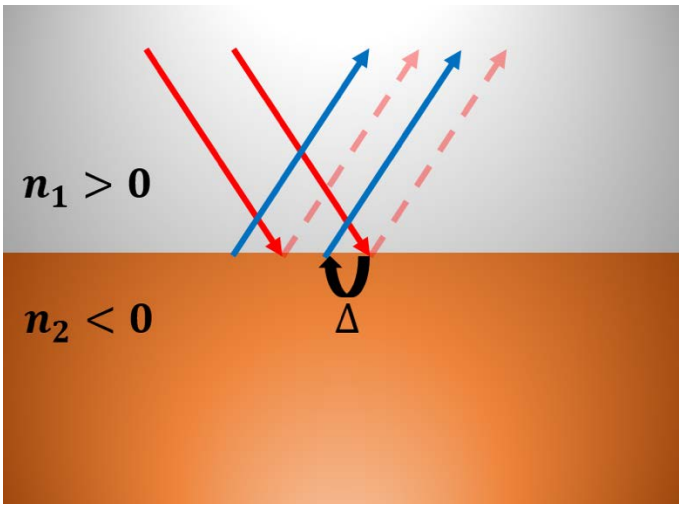

Figure 2.26 Goos-Hanchen effect in a left-handed medium.

2.8.5. Bianisotropic Effect - Edge and Broadside Coupled SRRs

Marques et al. have published several studies related to the bianistropy of SRRs. According to their arguments, the magnetic moment is induced by the incident magnetic field through rings that can also induce an electric moment. Therefore, it polarizes both the electric and magnetic fields which results in the bianisotropic effect. They suggested a new configuration of rings in which two rings are coupled from the broadside in order to eliminate this effect. In this configuration, the induced electric dipole moments in each ring would cancel while the induced magnetic dipole moments would sum, leaving the desired negative permeability feature of the ring intact [37, 40].

In general, edge-coupled SRRs have the bianisotropic effect because of electric and magnetic polarizations and asymmetry of the inner and outer rings. Therefore, there is a dependence of $\boldsymbol{D}$ on $\boldsymbol{H}$ and $\boldsymbol{B}$ on $\boldsymbol{E}$, via

$$\boldsymbol{D} = \bar{\bar{\varepsilon}} \cdot \boldsymbol{E} + \bar{\bar{\xi}} \cdot \boldsymbol{H} \tag{2.76}$$

$$\boldsymbol{B} = \bar{\bar{\mu}} \cdot \boldsymbol{H} + \bar{\bar{\xi}} \cdot \boldsymbol{E}. \tag{2.77}$$

In order to avoid this magnetoelectric coupling broadside coupled SRRs can be used. They have a non-bianisotropic property due to the broadside coupling of rings, and the charge distribution does not result in a net electric dipole (Figure 2.27 (b)).

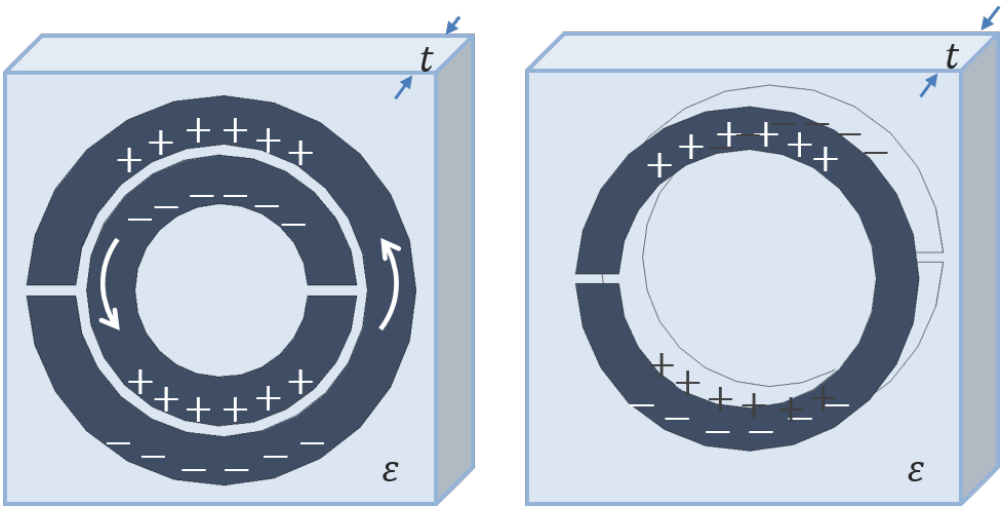

Figure 2.27 a) Edge-coupled SRR; b) broadside-coupled SRR.

The constitutive relationship for bulk SRRs can be analyzed using the constitutive relations, the bianisotropic property, and Maxwell's equations:

$$\boldsymbol{D} = \varepsilon_0 \boldsymbol{E} + \boldsymbol{P} \tag{2.78}$$

$$\boldsymbol{B} = \mu_0 (\boldsymbol{H} + \boldsymbol{M}) \tag{2.79}$$

where $\boldsymbol{P}$ and $\boldsymbol{M}$ are the polarization and magnetization vectors.

$$\bar{\bar{\varepsilon}} = \varepsilon_0 \left(1 + \overline{\overline{X_e}}\right) \text{ and } \bar{\bar{\mu}} = \mu_0 \left(1 + \overline{\overline{X_m}}\right). \tag{2.80}$$

After deriving these equations, we obtain the dispersion relation for TE waves,

$$k_x = \omega \sqrt{\mu_{zz} \varepsilon_{yy} - \mu_0 \varepsilon_0 \kappa_{yz}^2}; \tag{2.81}$$

moreover, for TM waves

$$k = \omega\sqrt{\mu_{\text{eff}}\varepsilon_{yy}} \text{ and } \mu_{\text{eff}} = \mu_{xx} - \frac{\varepsilon_0\mu_0\kappa_{yz}^2}{\varepsilon_{yy}}. \quad (2.82)$$

This result may vary depending on whether the structure is edge-coupled or broadside-coupled.

2.8.6. Techniques for Extraction of Material Parameters

In general, it is difficult to analytically derive the effective parameters of metamaterials due to the complexity of the structure. Alternatively, we can retrieve these parameters from numerical simulations. First, reflection and transmission coefficients for the metamaterials can be calculated to start the retrieval process using FDTD and FEM-based software. These structures can be simulated with the usual wave incident through a unit cell with a PEC-PMC waveguide configuration in HFSS. The difficulties of extracting the index of refraction using most of these methods are determining the correct value of m (branch) to use. The integer variable m is roughly related to the thickness of the slab in terms of wavelength.

Smith et al. [42] introduced an extraction method for constitutive parameters (ε, μ, Z, n) using S-parameters and reflection and transmission coefficients for inhomogeneous metamaterials. S-parameters are calculated from a wave incident normally onto a slab of metamaterial, and then the effective refractive index n and impedance Z can be obtained. Finally, permittivity and permeability are directly calculated from the general equations $\mu = nz$ and $\varepsilon = n/z$.

There are several other methods proposed for the sake of efficiency and to achieve better results. Kong et al. [43] improved the method to be able to solve the problems caused by the thickness of the effective slab when it is not accurately estimated, or reflection and transmission data has very small amplitude. He proposed a robust and effective retrieval method that has an advantage that the wave impedance and the imaginary part of the refractive index can be uniquely determined from the S-parameters. However, his method also has some limitations that require solving an iterative method based on a Taylor series expansion to be able to determine the real part of the refractive index. Besides, it cannot find any effective material parameters for some frequency regions for the common passive material condition.

Li et al. [44] also improved those methods using a method based on the Kramers-Kronig relationship. However, it also has some limitations because the resulting uncertainty is referred to as a branching problem that also affects the real part of the refractive index. Moreover, if the metamaterial is thick compared to the wavelength, more than one branch is involved and his technique does not provide accurate results.

A stepwise technique finds a solution to the aforementioned branching problem of the real part of the refractive index being related to the thickness of the slab. It measures the phase difference between two measurement points and uses the information about the phase delay at the previous point. For this reason, it does not need to verify the branch of each point separately. This method is also capable of finding a correct branch even in very noisy situations caused by the thickness of the slab. The one important feature of this technique is that the magneto-electric coupling coefficient can also be retrieved, which is essential for the analysis of bianisotropic SRRs [45, 46].

In this work we use the stepwise method to retrieve the effective constitutive parameters of metamaterials and show all retrieved results based on this technique. The reflection and transmission parameters are given by [46]

$$S_{11} = S_{22} = \frac{\Gamma_1(1-T^2)}{1-\Gamma_1\Gamma_2T^2} \text{ and } S_{21} = \frac{(1-\Gamma_1\Gamma_2)T}{1-\Gamma_1\Gamma_2T^2}, \tag{2.83}$$

where

$$\Gamma_{1(2)} = \frac{z_w^{\mp}-1}{z_w^{\mp}+1} \text{ and } T = e^{ik_0nL}, \text{and} \tag{2.84}$$

$$z_w^{+} = \frac{\mu_y}{n+i\xi_0} \text{ and } n = \sqrt{\varepsilon_z\mu_y - \xi_0^2}. \tag{2.85}$$

Here z_w^{+} is the normalized wave impedance, n is the refractive index, ε_z is the relative complex permittivity in the z direction, μ_y is the relative complex permeability in the y direction and ξ_0 is the magneto-electric coupling coefficient. The problem with these set of equations is caused by the dependence of the metamaterial length on the propagation parameter T. The method based on the stepwise technique that eliminates the propagation parameter is given in [46]. Based on that, the wave impedance is written as

$$z_w^{+} = \frac{-\Lambda_2 \mp \sqrt{\Lambda_2^2 - 4\Lambda_1\Lambda_3}}{2\Lambda_1}, \tag{2.86}$$

where

$$\begin{aligned} \Lambda_1 &= S_{21}^2 - (1-S_{11})(1-S_{21}), \qquad \Lambda_2 = 2(S_{11}-S_{22}), \\ \Lambda_3 &= (1+S_{11})(1+S_{22}) - S_{21}^2, \ \ \Lambda_4 = \frac{S_{11}+S_{22}}{S_{11}-S_{22}}. \end{aligned} \tag{2.87}$$

From S-parameters we obtain T as

$$T = \frac{\Gamma_1(1-\Gamma_1\Gamma_2)S_{21}}{(1-\Gamma_1\Gamma_2)(\Gamma_1 - S_{11}\Gamma_1\Gamma_2)} \tag{2.88}$$

$$n = \frac{[\mathrm{Im}(\ln T) \mp 2\pi m - i\mathrm{Re}(\ln T)}{k_0 L}. \tag{2.89}$$

Here n depends on the branch number m. Using the stepwise technique the problems caused by branch number are eliminated, and n is given by

$$n_{\,r+1} = \frac{\mathrm{Im}\left[\ln\frac{T_{r+1}}{T_r}\right] + \theta_{\,r} \mp 2\pi m_0 - i\ln|T_{\,r+1}|}{k_{\,0(r+1)}L}, \tag{2.90}$$

where

$$\theta_{\,r+1} = \theta_{\,r} + \mathrm{Im}\left[\ln\left(\frac{T_{\,r+1}}{T_{\,r}}\right)\right], \text{with} \tag{2.91}$$

$$T_r = e^{-k_0 n_r'' L} e^{+i\left(k_0 n_r' L \mp 2\pi m_0\right)} = |T_r| e^{+i\theta_{\,r}} \tag{2.92}$$

Eventually, one can retrieve the following effective constitutive parameters

$$\xi_0 = \frac{n(\Gamma_2 - \Gamma_1)}{i(1-\Gamma_1\Gamma_2)}, \tag{2.93}$$

where ξ is the magneto-electric coupling coefficient,

$$\varepsilon_z = \frac{n^2+\xi_0^2}{\mu_y}, \text{with} \tag{2.94}$$

$$\mu_y = \frac{(1-\Gamma_1\Gamma_2)(n^2+\xi_0^2)}{n(1+\Gamma_1\Gamma_2)-2n\Gamma_1-i\xi_0(1-\Gamma_1\Gamma_2)}. \tag{2.95}$$

As an example, the retrieval results that are shown in Figure 2.28 were obtained using the stepwise technique for the SRR structure in Smith's paper [42], which was chosen because it is easier to compare with his results. In the region 9.8-11.8 GHz this structure shows left-handed behavior.

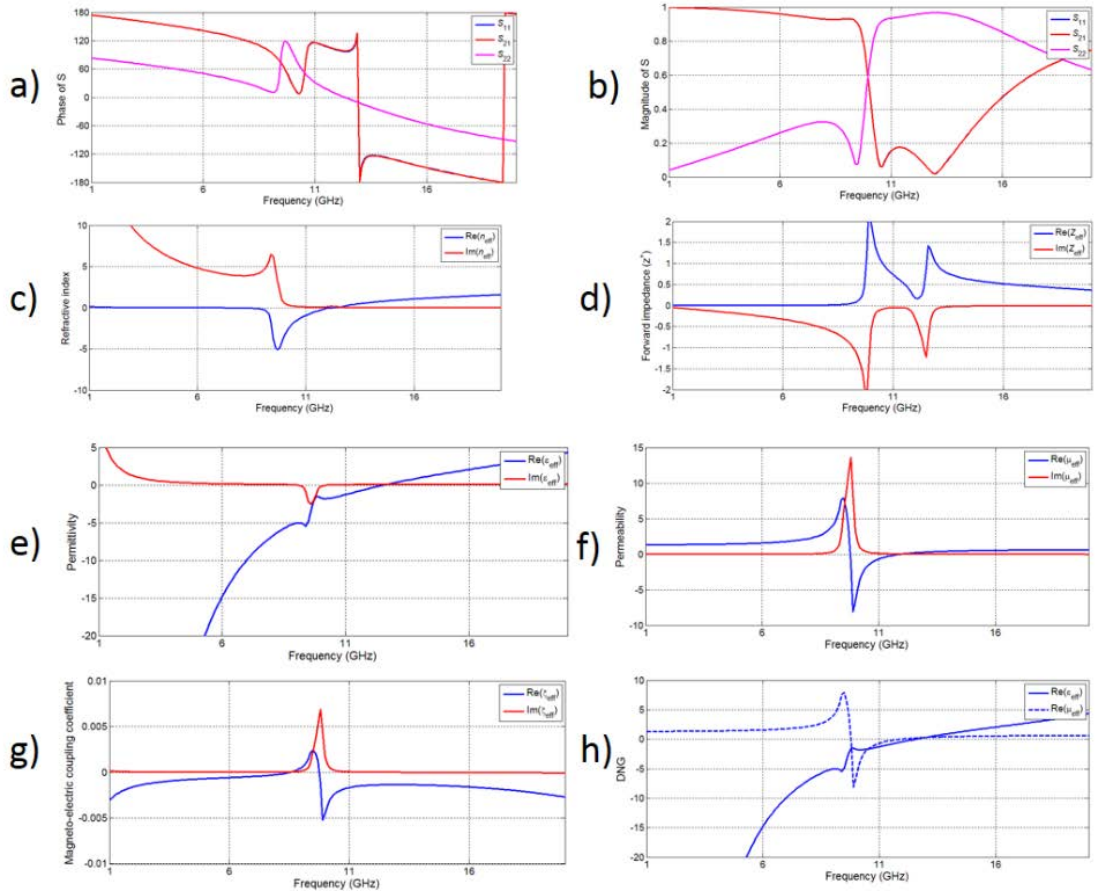

Figure 2.28 Retrieved constitutive material parameters: a) phase of S-parameters, b) magnitude of S-parameters, c) refractive index n, d) impedance Z, e) effective permittivity ε_{eff}, f) permeability μ_{eff}, g) magneto-electric coupling coefficient ξ_{eff}, h) double negative region.

CHAPTER 3: SIMILARITY OF PROPERTIES OF METAMATERIAL SLOW WAVE STRUCTURES AND METALLIC PERIODIC STRUCTURES

A study of the evolution of wave dispersion in systems of all-metallic periodic structures with increasing corrugation depth shows a similarity of the properties of waves in MSWSs and traditional metallic SWSs used in HPM sources. We show that the main properties of MSWSs, such as the existence of a lowest order negative dispersion wave below the cutoff, also appear in conventional metallic periodic systems with deep corrugations. Furthermore, we find that the appearance of negative dispersion in all-metallic periodic structures with increasing corrugation depth is accompanied by a hybrid mode being identified as the lowest order negative dispersion mode [47].

In this chapter, our interest is to identify MSWSs with novel dispersion characteristics for use in HPM source concepts. To avoid problems with electron beam propagation, such as charging of dielectrics, and to increase the thresholds of DC and microwave breakdown, we restrict our considerations to all-metallic SWSs as is usually the case in vacuum electronic sources of microwaves.

MSWSs commonly comprise periodically placed split rings as LC elements and pins as electric dipoles that, as a rule, are embedded in a dielectric substrate [42], where the period d of these repeated elements is much less than a wavelength λ of the operating wave, $d \ll \lambda$ [26]. On the other hand, MSWSs are electrodynamic structures that comprise metamaterial-loaded waveguides that can be used to generate HPM radiation through the Cherenkov interaction with an electron beam propagating through it [48, 49], Such

structures have the following properties that many authors attribute as being unique to metamaterials [31] [Ch. 1]:

1. In MSWSs, the lowest order propagating waves can be supported that are cutoff in smooth-wall waveguides of the same cross section [30]. It is pertinent to note that in such MSWSs, the waves are slow, which means that their phase velocity is less than the speed of light; thus, their wavelength is shorter than the vacuum wavelength so that the cutoff conditions are different compared with those found in corresponding smooth-wall regular waveguide. In this chapter, we establish that this property of supporting waves that would be cutoff in the smooth-wall waveguide is not unique to MSWSs and is inherent to ordinary metallic SWSs.
2. In the region of phase $0 \leq hd \leq \pi$ of the dispersion diagram $\omega(hd)$, low-order slow waves can exist with negative dispersion 4 in some frequency band (waves with negative group velocity $v_{gr} < 0$ and positive phase velocity $v_{ph} > 0$, where $h = \omega/v_{ph} = k/\beta_{ph}$ is the longitudinal wavenumber; $k = \omega/c$, where ω is the radian frequency and c is the light speed). Such slow waves exist in ordinary periodic metallic SWSs with deep corrugation [50-52].

Conventional vacuum electron microwave devices have been known to have the same properties as MSWSs long before the publication of Vesalago. For example, the oldest TWT with a spiral SWS [53] operates with the TM_{01} mode that cannot propagate in a smooth-wall waveguide with the same cross section. Another example is the coupled cavity SWS (Figure 3.1) of the powerful TWT [54] where, along with the operating forward wave, there is also a low-order wave with negative dispersion in the region $0 \leq hd \leq \pi$ that is below cutoff, which is usually determined for $hd = 0$.

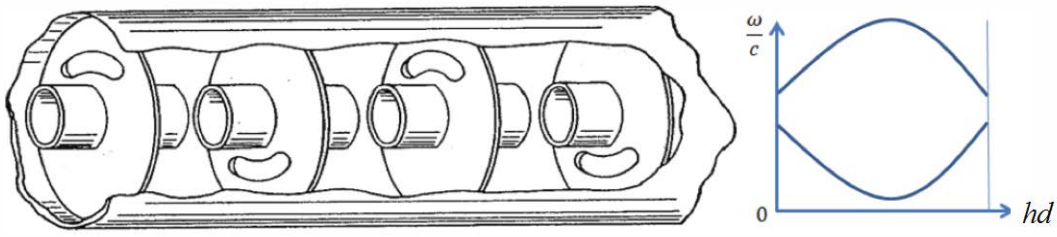

Figure 3.1 Left: SWS comprising coupled cavities; right: its corresponding dispersion diagram for the lowest two modes.

We would also like to mention that the dimensions of multi-cavity magnetron structures, as a rule, are less than the operating wavelength λ in these devices. For example, in the four-cavity magnetron [55] $\lambda = 11$ cm is much larger than its maximal diameter $2R_{\max} = 2.5$ cm, to say nothing of the period of the wave. The configuration of magnetron cavities (Figure 2.2) appears similar to split rings that are the usual elements of metamaterial structures [30].

Therefore, long before the appearance of the concept of MSWSs, many researchers in vacuum electronics worked with SWSs having properties similar to the known (at present) "unique" properties of MSWSs without knowing about it.

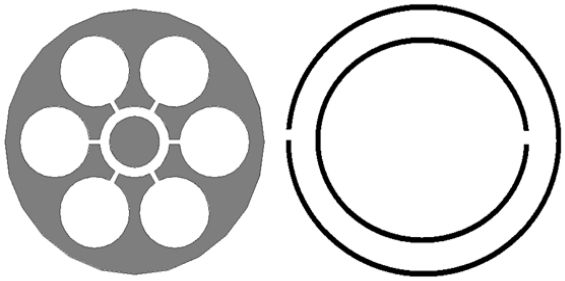

Figure 3.2 Left: Anode block of a magnetron showing the cavities; right: split rings as elements of an MSWS.

Since our interest is to engineer new dispersion relations using MSWSs for use in HPM sources, our motivation here is to demonstrate the similarity of the dispersion characteristics of waves in MSWSs with those in ordinary metallic SWSs.

In this chapter we demonstrate that the properties typically articulated as being unique to MSWSs are also found in traditional all-metallic SWSs with deep corrugations. We discuss the appearance of negative dispersion in all metallic SWSs and speculates on the reason for this. We then describe how the dispersion characteristics of all metallic SWSs evolve as the depth of corrugation of in these structures increases. Two classes of cylindrical structures are discussed – one with a sinusoidal corrugation, where the mean radius is fixed, and the corrugation depth increases (up to the point where diametrically opposite corrugations can touch). The other class is for a rectangular corrugation where the inner diameter is fixed, and the corrugation depth increases radially away from the structure.

3.1. Appearance of Negative Dispersion for Low-Order Waves

An effective permittivity

$$\varepsilon_{\text{eff}} = \varepsilon_0 \left(1 - \frac{\omega_{\text{cutoff}}^2}{\omega^2}\right) \tag{3.1}$$

and permeability

$$\mu_{\text{eff}} = \mu_0 \left(1 - \frac{\omega_{\text{cutoff}}^2}{\omega^2}\right) \tag{3.2}$$

can be used to describe metamaterials [30, 31]. These can also be used to describe an electromagnetic wave with wavenumber [33].

$$h = \sqrt{k^2 \varepsilon_0 \mu_0 - k_\perp^2} \tag{3.3}$$

propagating in a waveguide that is filled with a medium with permittivity ε_0 and permeability μ_0. For a waveguide filled only with a pure dielectric the permeability $\mu_0 = 1$ (in Gaussian units). Therefore, for $h = 0$ the transverse wavenumber is given as $k_\perp = \omega_c\sqrt{\varepsilon_0}/c$. The result is $h = k\sqrt{\varepsilon_0\mu_0\left(1 - \omega_{\text{cutoff}}^2/\omega^2\right)}$, which can be written as $h = k\sqrt{\mu_0\varepsilon_{\text{eff}}}$ using ε_{eff} from (3.1). Here the analogy with the permittivity of a cold plasma $\varepsilon_p = \left(1 - \omega_p^2/\omega^2\right)$ is used (ω_p is the plasma frequency). In a similar manner, μ_{eff} in the form of (3.2) is inserted (when $\varepsilon_0 = 1$ in Gaussian units).

To obtain the lowest order slow mode with negative dispersion in MSWSs, the artificial parameters of the corresponding medium are used, whereas the similar mode exists in ordinary metallic periodic systems with deep corrugation that can be used as SWSs in vacuum electronic sources of microwaves.

Our study of the evolution of low-order wave dispersion in periodic structures with increasing depth of corrugation and noting its similarity with the dispersion characteristics in MSWSs is especially rewarding, since no information about the specific modes associated with the low-order backward waves are given in many articles devoted to MSWSs [50-52]. Such information is important to describe Cerenkov interaction between the electromagnetic wave and electrons. Because of this, emphasis on the similarity of low-order modes in MSWSs and all-metallic SWSs with deep corrugation is important.

Since only discrete modes become backward waves in the interval $0 \leq hd \leq \pi$ a resonance phenomenon is suspected of being involved in leading to negative dispersion. In spite of a small period d in comparison with the wavelength $d \ll \lambda$ of the lowest order mode, for higher order modes (that have smaller wavelengths) negative dispersion occurs when their wavelength λ is close to the period d of the system. In this case the corrugated

wall SWS can be interpreted as a chain of coupled cavities (see, [52], in which for the backward H_{03} mode $\lambda \approx d$).

For low-order modes in a system with small period $d \ll \lambda$, the corrugation can be described by a surface (or slot) impedance Z [56, 57] that is given as

$$Z \sim \frac{E_{\perp}}{H_{\parallel}} \tag{3.4}$$

where $E_{\perp}$ and $H_{\parallel}$ are the electric and magnetic fields on the surface of the corrugated wall. Inside the corrugated surface, $E_{\perp}$ is the electric field transverse to the cavity and $H_{\parallel}$ is the longitudinal magnetic field. For rectangular corrugation of a planar surface with corrugation depth l_0, the impedance is proportional to $Z \sim (j/\eta)\tan(kl_0)$, which changes sign from $Z > 0$ to $Z < 0$ when $l_0 = (1 + 2n)\lambda/4$ (here $n = 0, \pm 1, \pm 2, ...$). For cylindrical surfaces with rectangular corrugation depth l_0 and inner radius R_0, this corresponds to $l_0 \geq \lambda/4$ since Bessel functions increase the scale of fields in comparison with planar wave functions. We speculate that modes with wavelength close to a resonant depth of corrugation must have negative dispersion. Unfortunately, there is no analytic expression for the surface impedance of an arbitrary corrugation. It is likely that for sinusoidal corrugation, the resonance occurs for slightly greater depths than for rectangular cavities (due to the difference in the volumes of rectangular and sinusoidal cavities) that we verified for modes in [42] and modes presented in our work.

In summary, we suspect that the appearance of negative dispersion (and the concomitant appearance of a hybrid EH_{11} mode as the second lowest order mode, as shall be described in the next section) is a consequence of a change in the sign of the surface

impedance at some resonant depth of corrugation (negative impedance, when one of the fields in (2.4) changes sign, could be characteristic of a left-handed medium as an MSWS).

3.2. Evolution of Wave Dispersion in Uniform Periodic Systems with Increasing Corrugation Depth

For all periodic systems with period d along the coordinate z (along the direction of wave propagation) the Floquet – Bloch theorem [56]

$$\boldsymbol{E}(\boldsymbol{r}, z = d) = \boldsymbol{E}(\boldsymbol{r}, z) \tag{3.5}$$

is valid and states that the fields in such systems can be represented as an infinite sum of spatial harmonics

$$\boldsymbol{E}(\boldsymbol{r}, z)e^{i\omega t} = e^{i\omega t} \sum_{n=-\infty}^{\infty} \boldsymbol{E}_n(\boldsymbol{r})e^{-ih_n z} \tag{3.6}$$

where $\boldsymbol{E}_n(\boldsymbol{r})$ is the field structure of the n^{th} spatial harmonic, $h_n = h_0 + n\bar{h}$, and $\bar{h} = 2\pi/d$. According to this representation, the dispersion characteristics of waves in a periodic system are a series of identical repeated dispersion curves with period $\bar{h}d = 2\pi$. Moreover, in each period, the dispersion characteristics are symmetric for waves in azimuthally uniform SWSs. Because of this we will only consider dispersion characteristics in the region $0 \leq hd \leq \pi$.

3.2.1. SWS with Sinusoidal Corrugations

We consider the evolution of the dispersion characteristics of low-order waves in an axisymmetric cylindrical system with a sinusoidal profile (Figure 3.3)

$$R(z) = R_0 + l_0 \sin(\bar{h}z) \tag{3.7}$$

that depends on the amplitude (depth) of corrugation l_0 (R_0 is the average radius of the cylindrical structure) in order to compare with the dispersion characteristics of MSWSs.

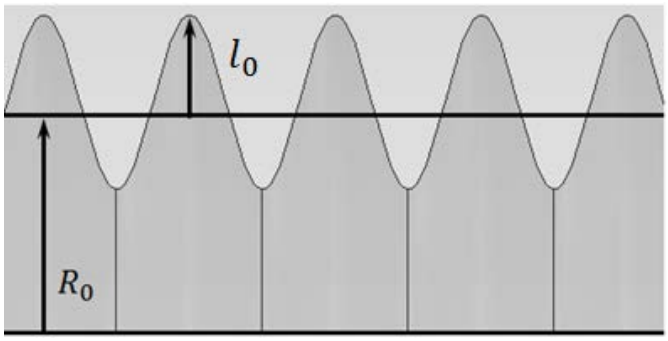

Figure 3.3 Cylindrical SWS with a sinusoidal profile.

Note that in the literature there are different conventions for representing dispersion diagrams. Specifically, there are different conventions for describing hybrid modes. For example, in [58] HE modes are determined as modes in which the components of longitudinal magnetic field prevail over the components of longitudinal electric field, $H_z > E_z$, and EH modes as modes, in which $E_z > H_z$. We will follow [59] where HE modes are defined as modes that are TE modes when the amplitude of corrugation $l_0 = 0$ (they are TE modes of a regular waveguide), and EH modes are TM modes of regular waveguide (when $l_0 = 0$). This definition is independent of the relation between H_z and E_z that can occur at some phase hd.

In hollow metallic waveguides, the dispersion curves of waves are hyperbolas (Equation 3.3) with asymptote $h = k$. When the wall of such a waveguide has a shallow periodic corrugation, the fields of all modes in the waveguide are represented as an infinite sum of spatial harmonics according to Equation 3.5, and their identical repeated dispersion curves intersect oppositely oriented identical hyperbolas with the light lines $h = \pm k$ as asymptotes. A splitting of the curves occurs at such intersections owing to coupling

between the harmonics (Figure 3.4), forming stopbands in which the mode reflects upon itself. When the dispersion curves of two different modes intersect, the stopband formed leads to conversion of one mode to an oppositely propagating different mode [60-63]. The dispersion characteristics of waves in periodic systems thus display alternating passbands and stopbands.

According to analytic theory [59, 64] for shallow corrugation depths satisfying $l_0 \ll R_0$ (Figure 3.3) and supported by computer simulations using the electromagnetic code HFSS [9] for a system with small period $d \ll \lambda$, for low order waves (typical for MSWSs), increasing the corrugation depth l_0 leads to an increase in the splitting of the points of intersection (Figure 3.4) that widens the stopbands. The deeper the corrugation amplitude l_0 is, the wider is the stopband. Figures. 3.5-3.9 show the evolution of the dispersion relation as the corrugation depth l_0 increases for the lowest modes of a SWS with $R_0 = 1.6$ cm and different periods d. We considered SWSs with period $d = 0.671$ cm that was used earlier in a relativistic TWT [65] with the operating TM_{01}-mode when $l_0 = 4$ mm, and also for $d = 2$ and 3 cm. We find that the greater that the period d is, the greater the corrugation depth l_0 is required for the appearance of the low-order hybrid EH_{11} mode with negative dispersion (Figure 2.10).

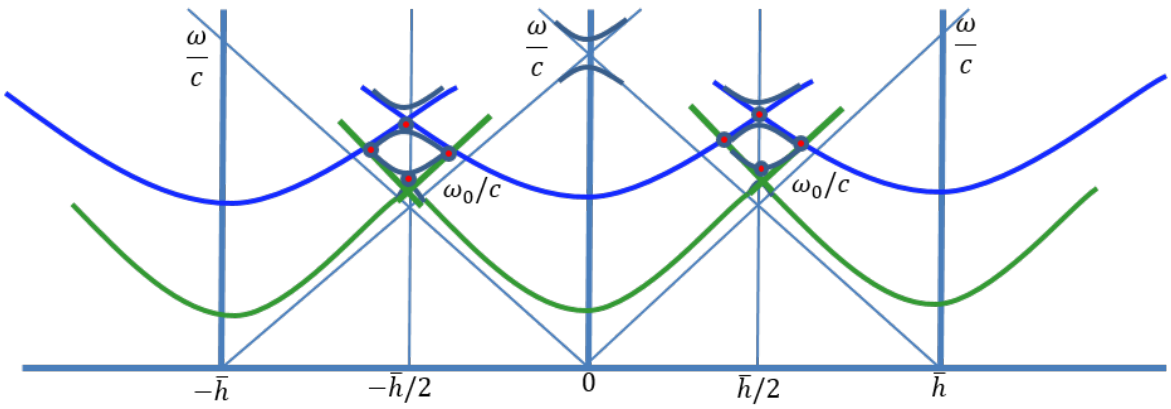

Figure 3.4 Dispersion curves for the two lowest modes with their corresponding spatial harmonics.

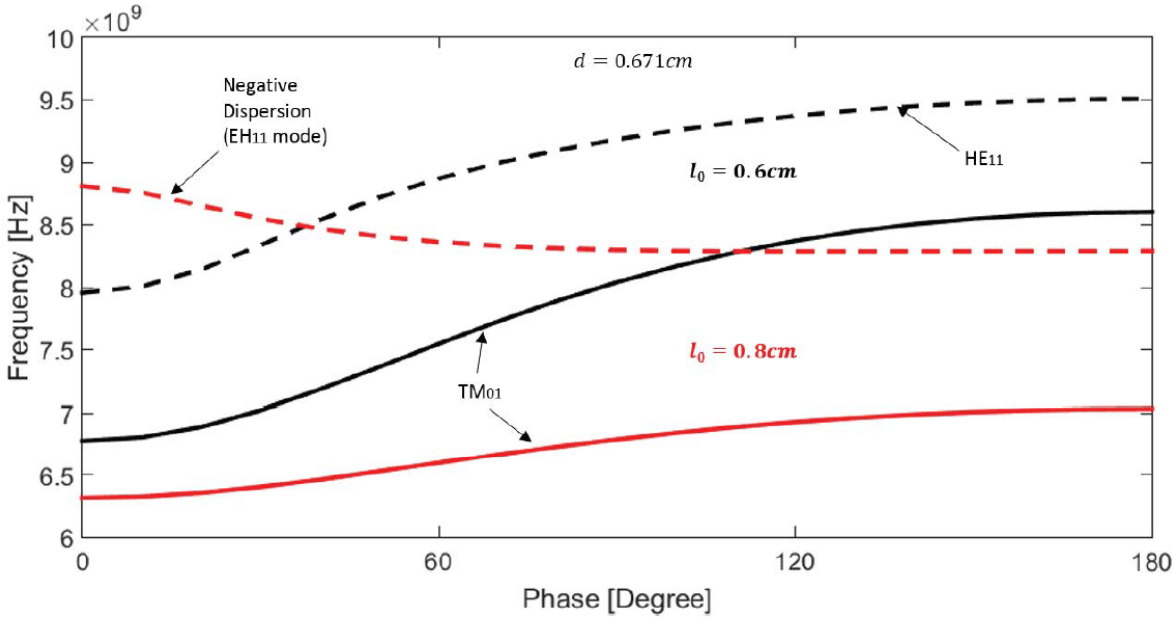

Figure 3.5 Dispersion diagram for the lowest order modes with different corrugation depths in a cylindrical SWS (solid lines represent the first mode while dashed lines represent the second mode for each corrugation depth indicated) with mean radius $R_0 = 1.6$ cm and period $d = 0.671$ cm.

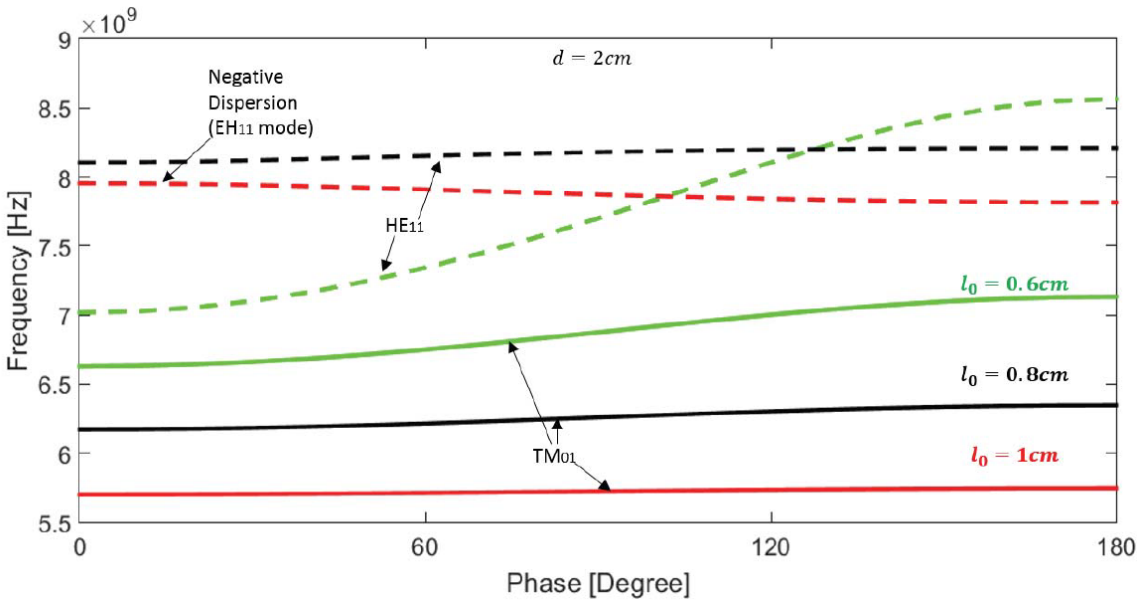

Figure 3.6 Dispersion diagram for the lowest modes with different amplitude of sinusoidal corrugation in an SWS with mean radius $R_0 = 1.6$ cm and period $d = 2.0$ cm.

For the sinusoidal SWS with period $d = 0.671$ cm the hybrid EH_{11} mode (its structure is shown in Figure 3.9) displays negative dispersion when the corrugation depth $l_0 = 8$ mm (Figure 3.5).

Here we would like to point out once again that the appearance of a low-order backward wave corresponding to negative dispersion was deemed to be one of the unique characteristics of MSWSs (the TM_{01} mode is the lowest mode, but it has positive dispersion).

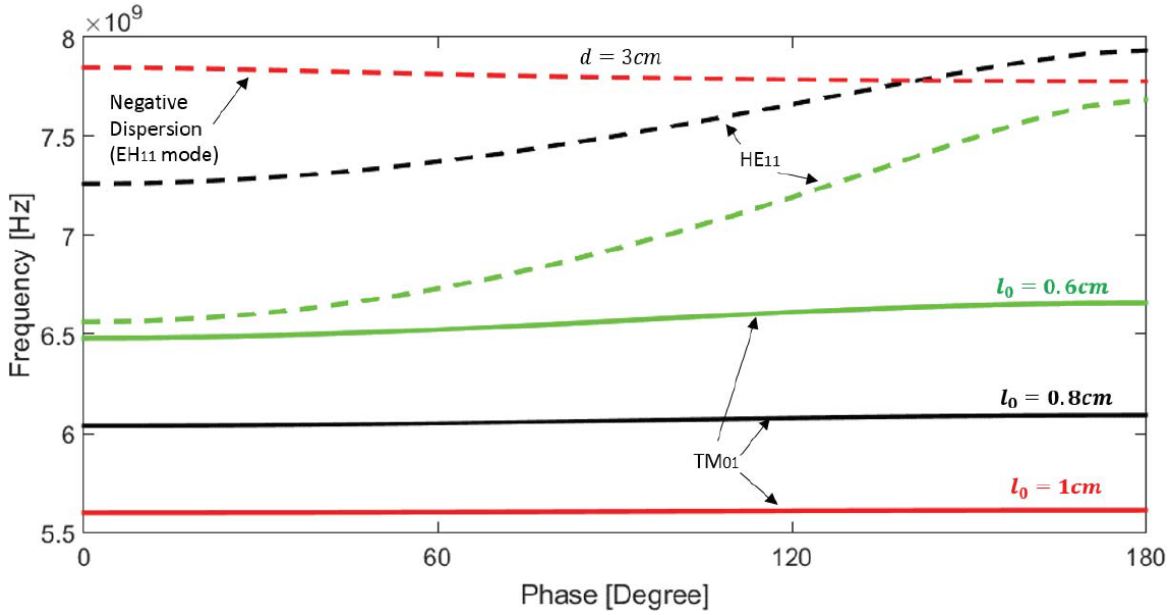

Figure 3.7 Dispersion diagram for the lowest modes with different amplitude of sinusoidal corrugation in an SWS with mean radius $R_0 = 1.6$ cm and period $d = 3$ cm.

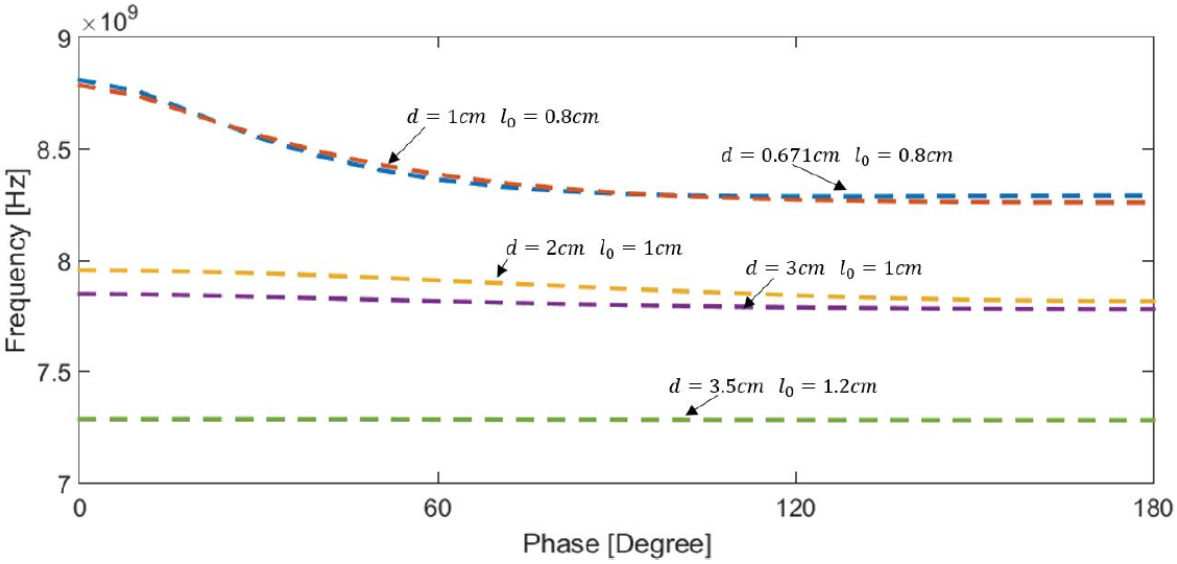

Figure 3.8 Dispersion diagram for the EH_{11} mode in an SWS with a profile given by (3). $R_0 = 1.6$ cm with various periods d and corrugation depths l_0.

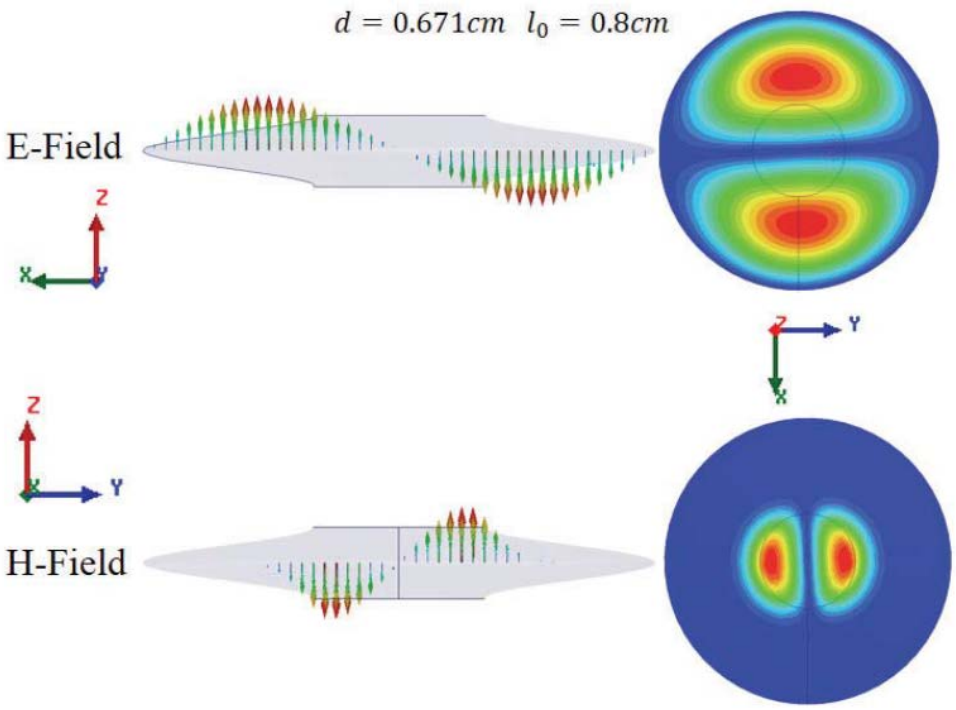

Figure 3.9 Structure of the hybrid EH_{11} mode in an all-metallic SWS with sinusoidal corrugation (Figure 3.3).

Further, increase in corrugation depth l_0 leads to a flattening of the dispersion diagram, which is easily understandable because when the oppositely located sinusoidal corrugations of the SWS touch and totally close the inner SWS space, a set of separate cavities is formed with the same resonant frequency for each cavity that corresponds to the straight dispersion diagram, which is independent of phase hd.

Increasing the corrugation depth l_0 also leads to decreasing the cutoff frequencies of TM_{01} modes and decreasing the cutoff frequencies of the hybrid EH_{11} mode, as is shown in Figure 3.10.

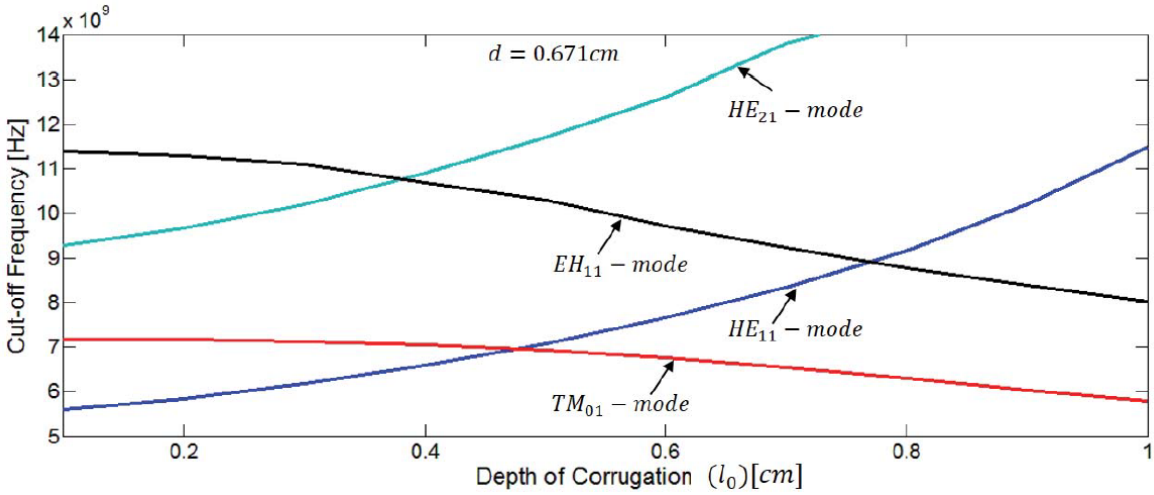

Figure 3.10 Dependence of cutoff frequencies of low order modes on corrugation depth l_0 for the period $d = 0.671$ cm.

3.2.2. SWS with Rectangular Corrugations

Thus, for the sinusoidal profile SWS increasing l_0 leads to a narrowing of the channel for electrons in HPM sources. To avoid this inconvenience, let us consider the SWS shown in Figure 3.11 with constant minimum cross section with radius R_0 and rectangular corrugation with the depth l_0 that could be used to propagate an electron beam with fixed cross section.

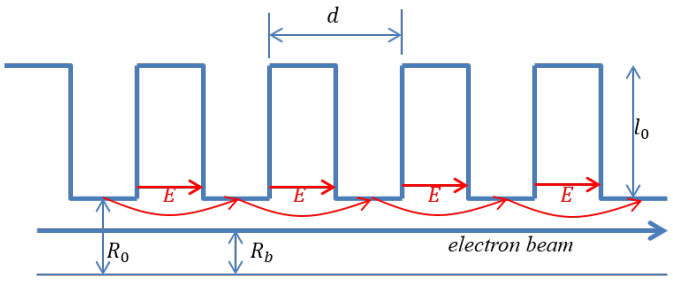

Figure 3.11 Cylindrical SWS with $R_0 = 1.6$ cm and rectangular (meander) profile of periodic system with depth of corrugation l_0.

Dispersion diagrams for different periods for such a system are shown in Figs. 3.12-3.14 for corrugation amplitudes l_0 of rectangular cavities. In each case, the lowest mode

with negative dispersion is a hybrid EH_{11} mode (and this mode is the second lowest mode overall; the lowest mode is the TM_{01} mode with positive dispersion, similar to what is shown in Figure 3.5). In addition, we found that the larger the period d, the deeper must be corrugation l_0 for the appearance of low-order backward waves (Figure 3.15). Again, the negative dispersion of low modes in the traditional SWSs with deep corrugation is similar to that of MSWSs. Furthermore, we would like to point out that, as an example from Figure 3.13, the negative dispersion appears with $l_0 = 1.7$ cm. Since $R = I_0 + r_0 = 3.3$ cm, the ratio $r_0/R = 1.6/3.3 = 0.48$, which is exactly what Garcia et al. [57] found was required for the appearance of negative dispersion and the EH_{11} mode.

The structure of the hybrid backward EH_{11} mode for an SWS with rectangular profile and period $d = 2$ cm is shown in Figure 3.16.

Special consideration is given to identification of left-handed media and metamaterials [26, 27]. For the rectangular (planar) profile of corrugation the impedance (Figure 3.4) alternates sign. When $\mathrm{Im}\{Z\} < 0$ (which is characteristic of a left-handed medium) a low-order hybrid wave with negative dispersion appears in region $0 \leq hd \leq \pi$. For a cylindrical SWS with rectangular corrugation, the result of increasing the corrugation depth l_0 can be different because of decreasing values of the Bessel functions. Thus, the result depends on the value of the inner radius R_0. For $R_0 = 1.6$ cm we found that the EH_{11} mode with negative dispersion appears when $l_0 = 1.8$ cm. Further increasing the corrugation depth leads to narrowing the regions of frequencies with increasing their average frequencies for the backward wave.

It is pertinent to note that any slow hybrid mode of a metal periodic system can be used for interaction with a longitudinal electron beam because of the appearance of a longitudinal component of the electric field.

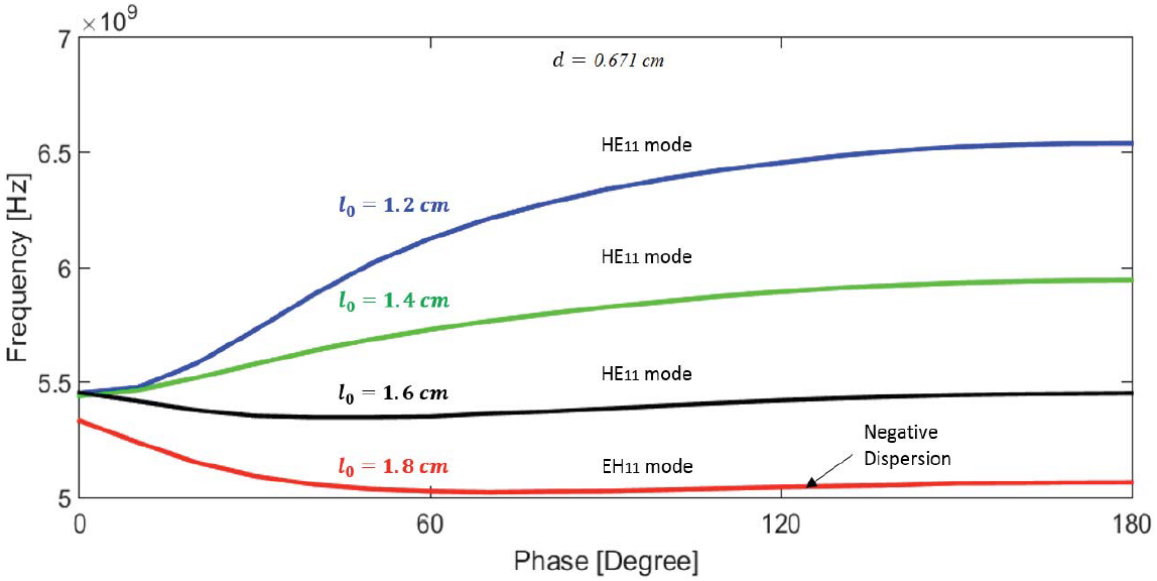

Figure 3.12 Dispersion of lowest modes in rectangular profile systems with period $d = 1$ cm and various corrugation depths l_0.

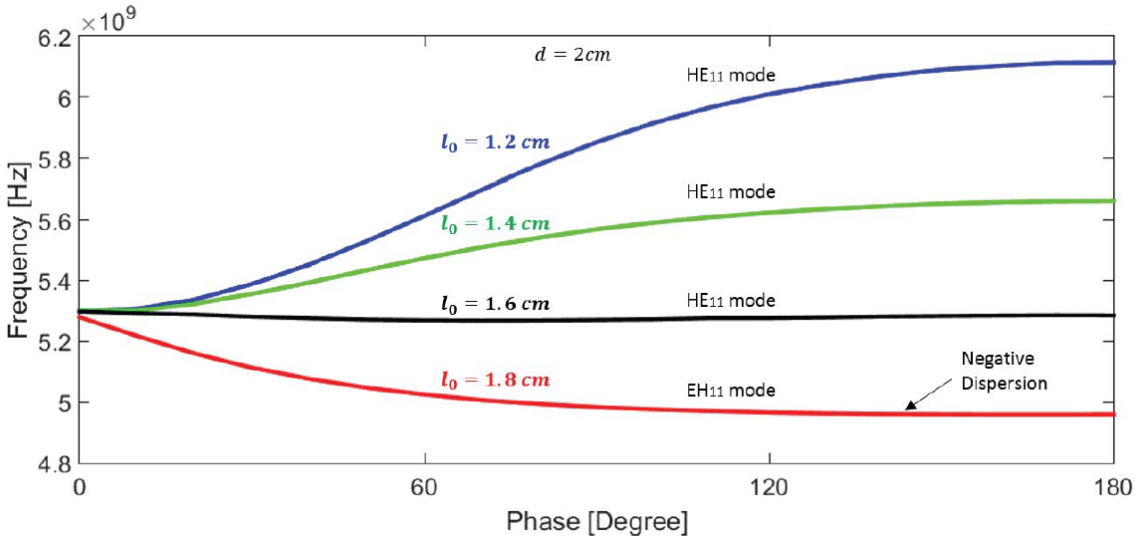

Figure 3.13 Dispersion of lowest modes in rectangular profile systems with period $d = 2$ cm and various corrugation depths l_0.

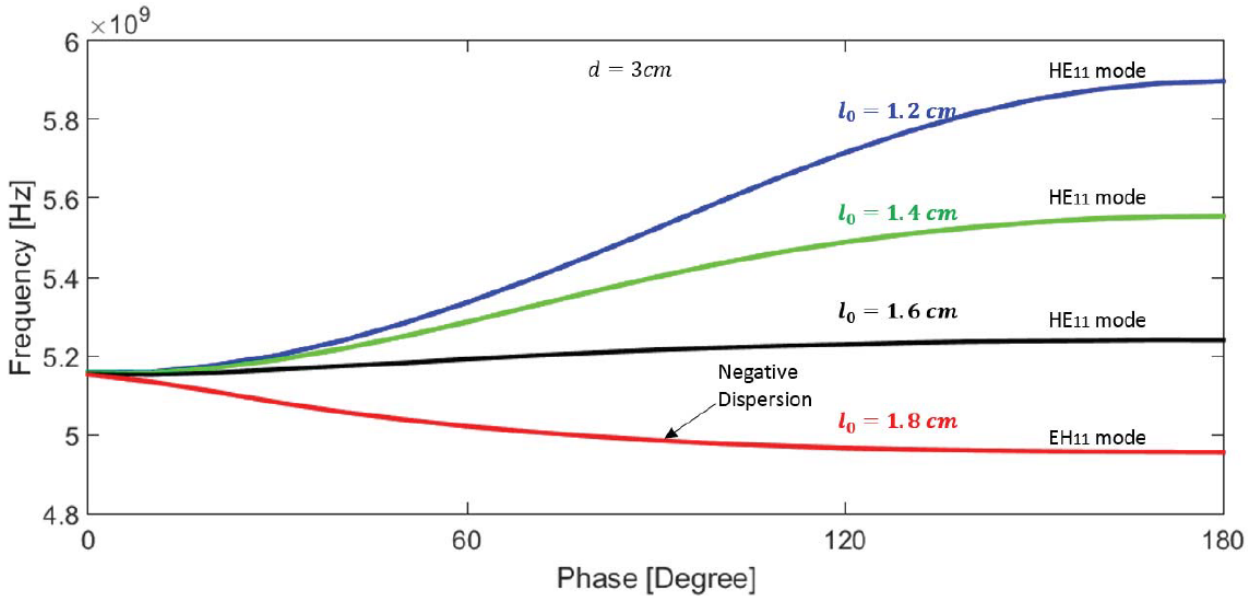

Figure 3.14 Dispersion of lowest modes in rectangular profile systems with period $d = 3$ cm and various corrugation depths l_0.

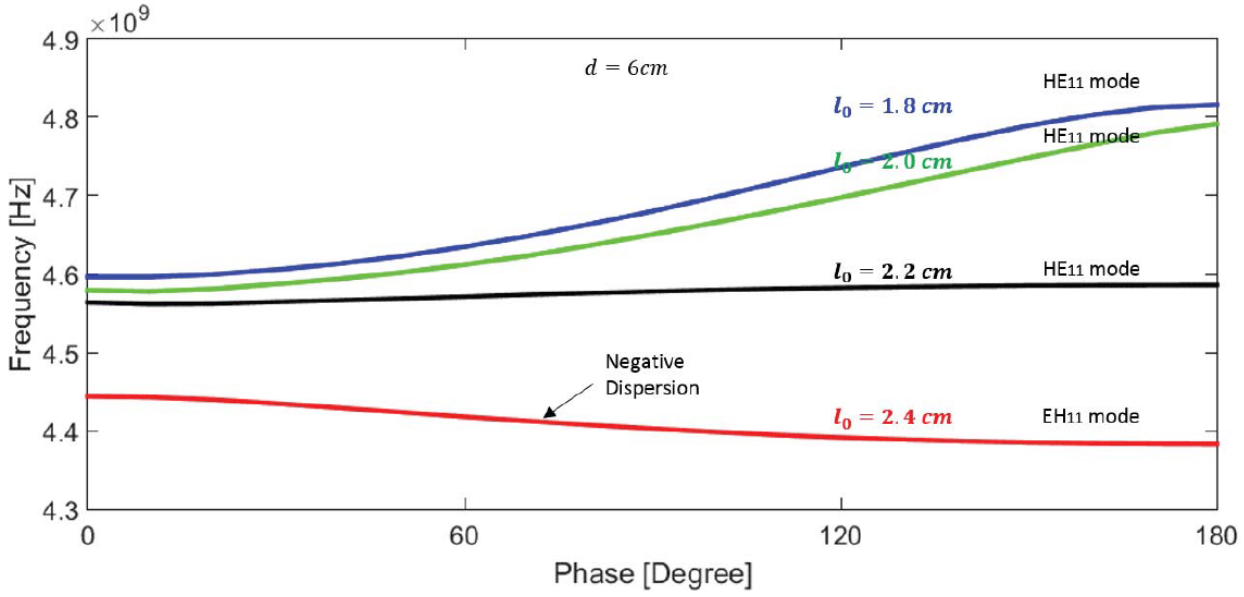

Figure 3.15 Dispersion of lowest modes in rectangular profile systems with period $d = 6$ cm and various corrugation depths l_0.

In summary, using computer simulations we have demonstrated that for some low-order waves in all-metallic periodic systems (SWSs) that increasing the corrugation depth lead to a large splitting in the intersection of their dispersion curves at the phase $hd = \pi$

(as in a MSWS). Corresponding points on such curves with upper cutoff frequencies at the first passband become lower cutoff frequencies (Figure 3.17) that corresponds to the appearance of backward waves in the interval $hd \in (0, \pi)$. In this case, the usual interpretation of stopbands separating passbands unsuitable, as well as the interpretation of the lower (at the phase $hd = 0$) and upper cutoff frequencies (at phase $hd = \pi$).

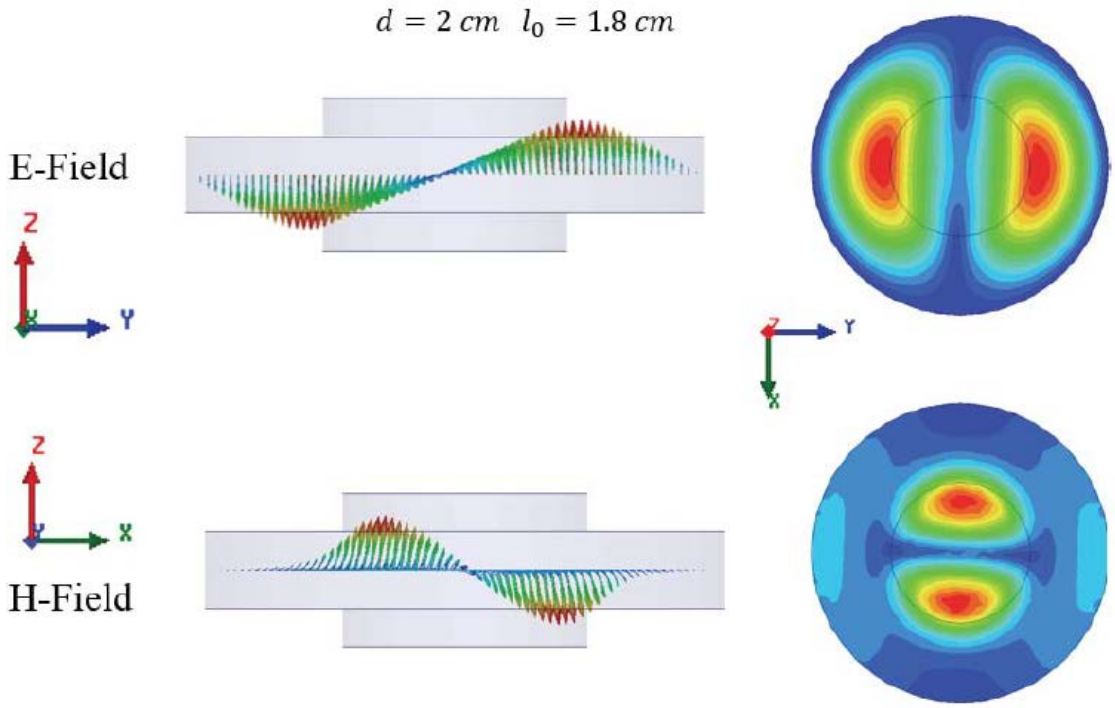

Figure 3.16 Transverse structure of the lowest modes in the SWS (Fig 3.9).

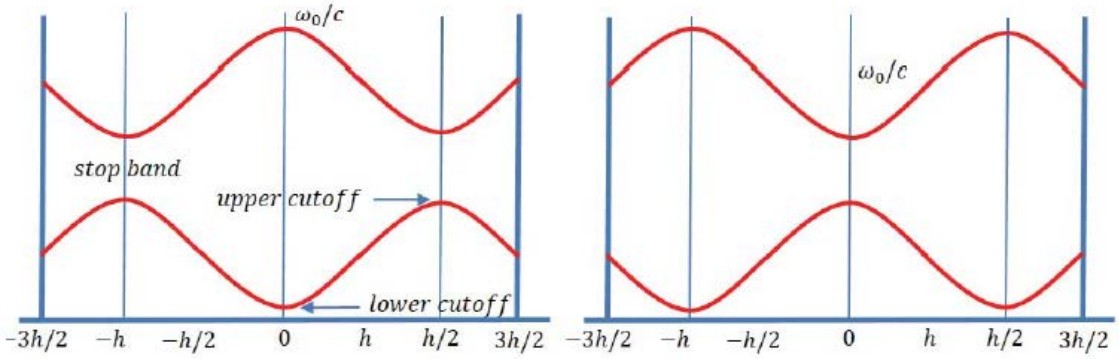

Figure 3.17 Dispersion diagrams for lowest mode in an SWS with small period $d \ll \lambda$ when the corrugation depth is small, $l_0 \ll \lambda$ (left) and when the surface impedance of the SWS slot is resonant $l_0 \geq \lambda/4$ (right).

We assume that the appearance of waves with negative dispersion (and the concomitant appearance of a hybrid EH_{11} mode as the lowest order mode) is associated with some resonance phenomenon. For a high order mode, the negative dispersion takes place when its wavelength is close to the SWS period. For a low order mode, it could be in the interval where the depth of corrugation corresponds to the negative surface impedance, $\mathrm{Im}\{Z\}$, as in a left-handed medium.

Thus, we have shown that the well-known properties of MSWSs are, in fact, common properties of all-metallic periodic systems with deep corrugations.

It is conceivable that additional properties of MSWSs will be identified in the future that will not have similar properties in traditional SWSs.

CHAPTER 4: DESIGN OF AN O-TYPE MSWS FOR HPM GENERATION

4.1. Motivation and Background

HPM sources have long been analyzed and developed in order to increase the efficiency and to have a more compact design within the desired application limitations. Many types of microwave sources, including TWTs and BWOs, have been well-established for HPM generation based on Cerenkov or Smith – Purcell radiation in order to produce coherent radiation with an electron beam and electromagnetic wave interaction inside a SWS. While TWTs produce amplification of a microwave signal, BWOs generate backward waves which are traveling in the opposite direction of the electron beam with negative group velocity $v_g < 0$ [66].

Recently, a new research thrust related to the use of metamaterials in HPM sources took researchers' attention because of the so-called unique properties of MSWSs [48, 67-81]. A Multidisciplinary University Research Initiatives (MURI) grant was awarded to research topic of "innovative use of metamaterials in confining, controlling, and radiating intense microwave pulses" with contribution from five universities including UNM, MIT, LSU, OSU, and UC Irvine. Cerenkov radiation in an MSWS has been a topic of interest due to the backward wave propagation and interest in comparing its operation with a BWO [68]. In light of this motivation, this chapter describes a novel design of an MSWS for HPM generation that produces HPM with the coupling of an electron beam with an MSWS. It is similar to a BWO's SWS because the electron beam interacts with a negative dispersion mode, resulting in backward wave propagation. The difference is that in a BWO

negative dispersion occurs in the second passband, where as for the MSWS negative dispersion occurs in the first passband.

We describe a new O-type HPM oscillator that uses an MSWS supporting waves with negative dispersion. The MSWS comprises periodically alternating, oppositely oriented SRRs connected to a metal tube where the distance between the rings is much less than a wavelength. The SRRs provide negative μ. The diameter of the metal tube is such that the generated oscillations are below cutoff, thus providing negative ε. A tubular electron beam propagates through this structure. The interaction space is coupled with the outer coaxial channel through gaps between the SRRs. Radiation is extracted at the end of the outer channel via a conical horn section.

Briefly, using particle-in-cell (PIC) simulations, it was found that the electron beam in the interaction space forms a sequence of trapped electron bunches by the synchronous operating wave. The output parameters of this oscillator for an applied voltage $U = 400$ kV, electron beam current $I = 4.5$ kA, and guide axial magnetic field $B = 2$ T are a radiation power $P = 260$ MW, radiation frequency $f = 1.4$ GHz, and efficiency $\eta = 15\%$ when the total SWS length L consisting of 12 split rings is 34.5 cm. The output radiation pattern corresponds to a TE_{21}-like mode.

4.2. Design Considerations

Unlike [48, 70], where the low output power of around 5 MW was demonstrated, we are aiming to achieve optimum coupling of the electron beam to the MSWS to demonstrate >100 MW generation with rapid growth. (The growth time of oscillations in [48] was a few 100 ns and no information on growth time was provided in [70], but it is also assumed to be long. We require growth times to be no longer than several ns due to experimental limitations with the UNM SINUS-6 electron beam accelerator.) Since the synchronous operating wave has negative dispersion, its interaction with the electron beam inside the MSWS is as in a conventional BWOs with reflections from the ends where cylindrical waveguides with the same radius as the minimal radius $r_{\min}$ of the MSWS are placed. It is pertinent to reiterate that the frequency of the generated wave in the MSWS is below the cutoff frequency for a regular waveguide of the same radius. We next describe some design considerations.

First, conventional metamaterial structures, which were described in Chapters 1 and 2, cannot survive in the high power environment because of their geometry and material that comprise a dielectric substrate with etched metallic structures. Since metamaterials are highly resonant structures, the dielectric substrate would heat and melt. In addition, as a MSWS, the presence of electrons usually leads to charging of a dielectric, which in turn may result in dielectric breakdown [67]. In order to eliminate these problems we chose to use an all-metallic structure.

Second, the undesired effects of bianisotropy were discussed in Chapter 2. In order to avoid this effect and design a non-bianistropic structure, we chose a modified form of a broadside-coupled SRR (BCSRR) geometry.

Third, we designed a structure that can produce a backward wave with a negative dispersion mode and has negative refraction index, which is one of the fundamental metamaterial properties due to the configuration of its geometry.

The design procedure is summarized in Figure 4.1.

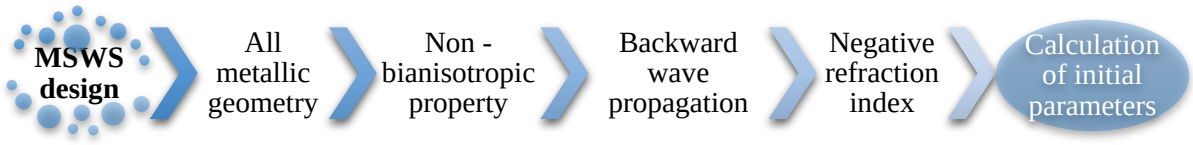

Figure 4.1 Summary of design procedure of MSWS.

Unlike the planar metamaterials that have been used for studying the interaction of electromagnetic fields with electrons [24, 26, 27] and a cylindrical MSWS comprising a pair of concentric solid rings with a radial gap between them, here we study a cylindrical MSWS consisting of separated rings with oppositely oriented cuts as shown in Figure 4.2.

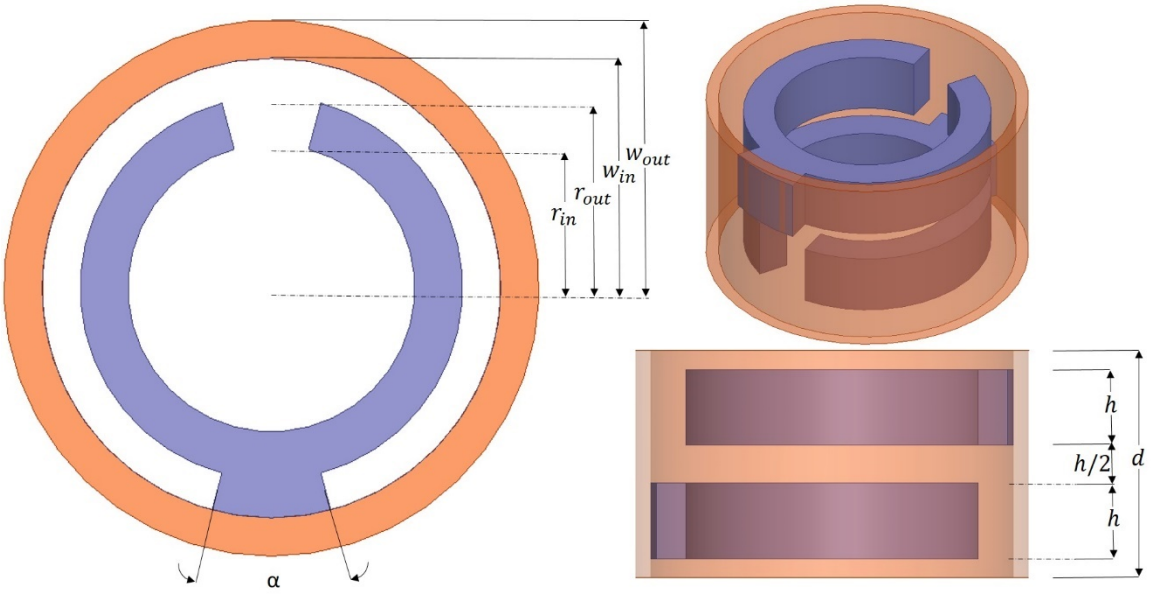

Figure 4.2 Geometry of the O-Type MSWS in different angles of view for a single unit cell.

The MSWS consists of split rings where the broadside coupled rings are 180° out of phase. Each split ring is electrically connected to the output waveguide with a 30° conducting tab, and each ring has a slit in one side except for the final three rings that are solid. These final rings, which are continued onto a conical antenna, are connected to each other in a different way than the other rings, as shown in Figure 4.3. Table 4.1 gives the actual dimensions of the structure.

Table 4.1 Dimensions of the O-Type MSWS.

r_{in}	r_{out}	w_{in}	w_{out}	α	h	d
1.5 cm	2 cm	2.4 cm	2.8 cm	30 degrees	1 cm	3 cm

The actual MSWS consists of 12 split ring elements and is mounted inside a cylindrical channel (Figure 4.3). It also has regular cylindrical waveguides at both ends of the MSWS connected to the channel as all the rings to keep them at the same potential $U = 400$ kV with respect to the cathode potential. A conical horn section is also included in order to mitigate undesired breakdown at the output port.

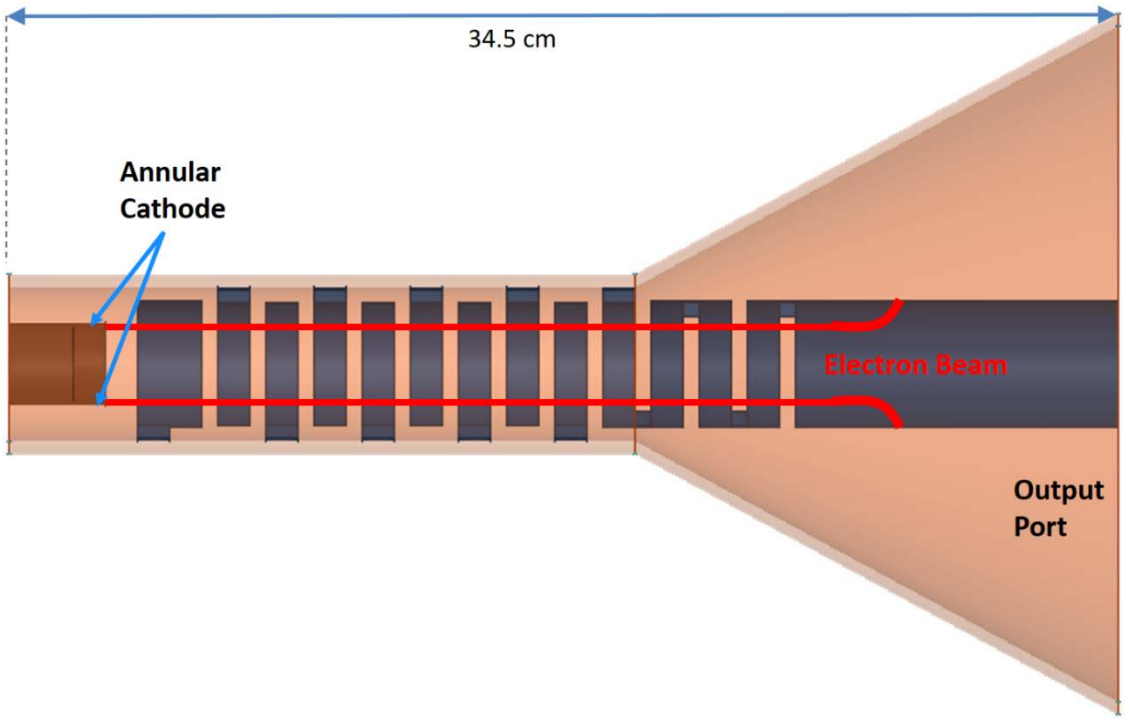

Figure 4.3 Illustration of the entire SWS tube.

The oscillator has a coaxial design with outer channel coupled to the interaction space through gaps between the split rings of the MSWS. The electromagnetic energy completely flows through the MSWS. The explosive electron emission thin-walled tubular cathode is placed in the inner channel of the coaxial structure. The oscillator is immersed in a strong guide axial magnetic field $B = 2$ T that provides longitudinal motion of electrons (practically without transverse motion) with radius R_B that is equal to the cathode radius R_C. Most of the initial design parameters were defined according to UNM's HPM laboratory's accelerators, such as the SINUS-6. Table 4.2 summarizes the input parameters of the structure for MAGIC PIC code simulations and its experimental realization.

Table 4.2 PIC simulation parameters.

Cathode Radius	1.3 cm
Anode Radius	2.4 cm
Applied Voltage	400 kV
Voltage Rise-time	2 ns
Magnetic Field	2T

4.2.1. Forming Trapped Electrons by the Electromagnetic Field

Since the period of the MSWS is much less than a wavelength, $d \ll \lambda$, for the stationary electron beam such a MSWS together with the regular waveguide is a uniform channel. For a uniform channel with coaxial thin-walled tubular cathode when the total system is immersed in a uniform guide axial magnetic field, an electron current is determined by a relation [82]

$$I_B = \frac{mc^3}{e} \frac{\beta_B(\gamma_A - \gamma_B)}{2\ln\left(\frac{R_a}{R_c}\right)} \tag{4.1}$$

where e, m, $\beta_B = v_b/c$ and $\Upsilon_B = (1-\beta_b^2)^{-1/2}$ are electron charge, rest mass, velocity v_b relative to a speed of light, c, and relativistic factor, respectively; $mc^3/e = 17.1$ kA is the Alfvén current; $mc^2/e = 511$ keV is the electron rest mass;

$$\gamma_A = 1 + \frac{eU}{mc^2} \tag{4.2}$$

and

$$\beta_B = \frac{\sqrt{\gamma_B^2 - 1}}{\gamma_B}. \tag{4.3}$$

When the thin-walled tubular cathode with explosive emission is in the uniform channel immersed in an infinite magnetic field the electron beam potential is [83]

$$\gamma_B = \sqrt{2\gamma_A + 0.25} - 0.5 \tag{4.4}$$

(the parameters of electron beams moving in uniform finite magnetic field are given in [84]). The current (4.1) with potential (4.4) is less the space-charge-limited current [82]

$$\frac{eI_{\max}}{mc^3} \ln\left(\frac{R_a}{R_c}\right) = \left(\gamma_A^{2/3} - 1\right)^{3/2} \tag{4.5}$$

that takes place when the potential of electrons is

$$\gamma_B = \gamma_A^{1/3}. \tag{4.6}$$

We are not interested in the case when $I_B > I\max$, which is the case when a virtual cathode (VC) appears. We consider the case when the interaction of electrons with synchronous electromagnetic fields leads to another phenomenon – electrons of the uniform beam are trapped by the increasing strong electromagnetic field when oppositely moving electrons appear relative to average velocity (Figure 4.4) [85].

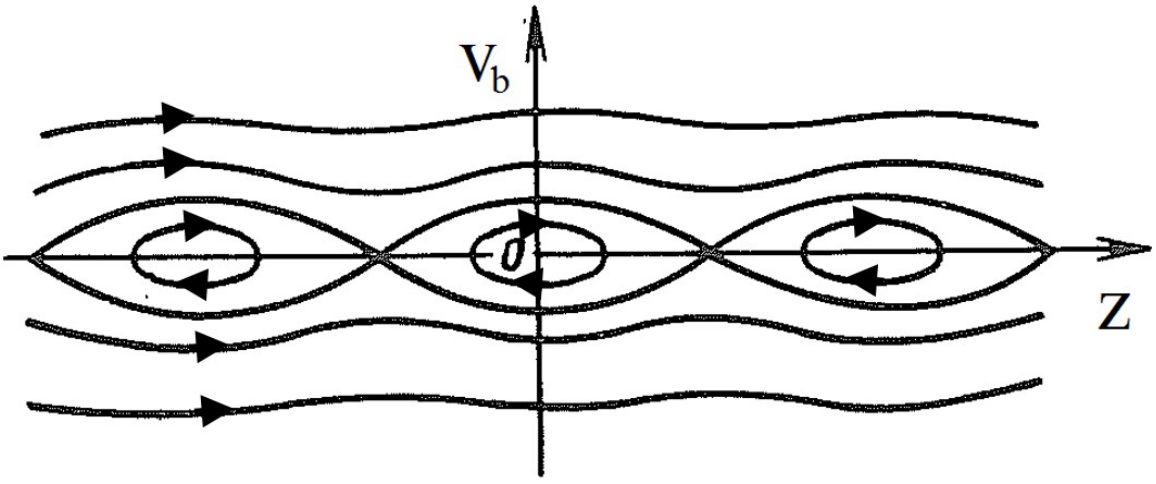

Figure 4.4 Phase space trajectories of electrons moving in a monochromatic wave field [85].

The appearance of electrons trapped by a monochromatic electromagnetic field is inherent to many situations. Here it takes place in a microwave oscillator using an MSWS,

whereas in any O-type microwave oscillator the inertial grouping of electrons forms dense bunches (traps) that, in turn, leads to increasing electromagnetic field.

4.3.Operation of the Oscillator with Cold Simulation Results

4.3.1. Eigenmode Simulations

The resonant frequency of the structure is designed to be below cutoff for a regular cylindrical waveguide. The cutoff frequencies of the three lowest order modes in a cylindrical waveguide with radius 2.4 cm are given in Table 4.3.

Table 4.3 Cutoff frequencies of a hollow cylindrical waveguide with radius 2.4 cm.

TE_{11}	3.6 GHz
TM_{01}	4.78 GHz
TE_{21}	6.07 GHz

Using the full wave electromagnetic code HFSS, it is possible to calculate the dispersion diagram using the eigenmode solver. The MSWS supports forward and backward waves for the two lowest order mode. The dispersion diagram shows that the beam line intersects with the negative slope of the dominant mode suggesting a backward wave generation with the operating frequency of 1.5 GHz. Fig 4.5 shows the dispersion diagram along with the beam line $2\pi f = k_z v_0$ where v_0 = 0.72c and the light line $2\pi f = k_z c$.

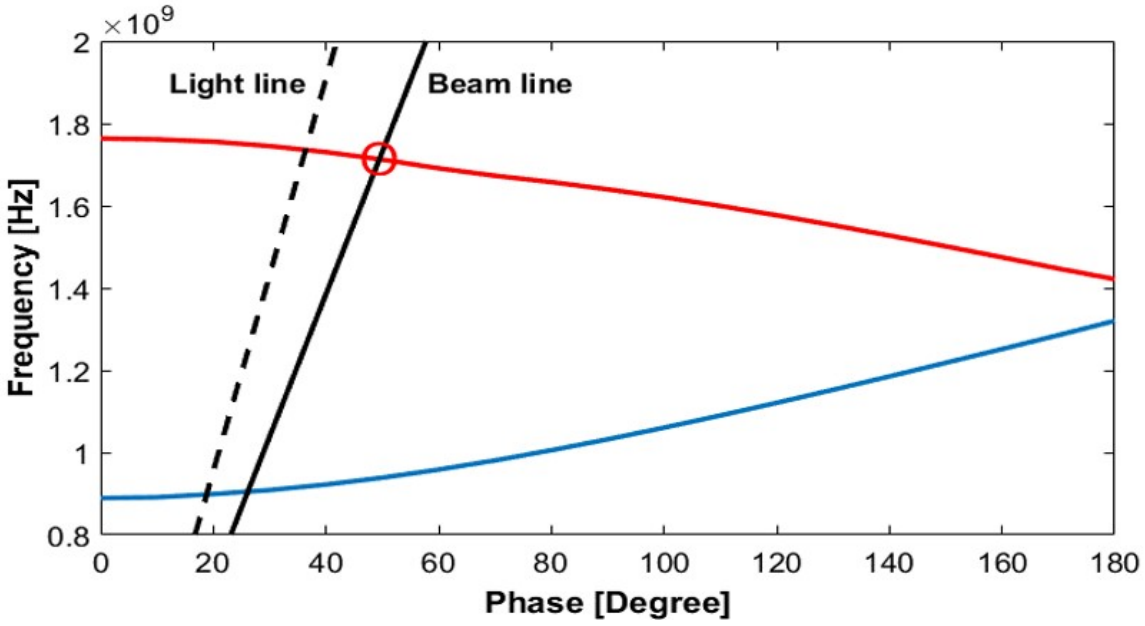

Figure 4.5 Dispersion diagram for the MSWS. The first two modes are shown, along with the light line (dashed) and the beam line (solid).

A negative dispersion mode at the operating frequency shows TE-like mode behavior since the H_z component is stronger than the E_z mode. The field characteristics of the structure are shown in Figure 4.6.

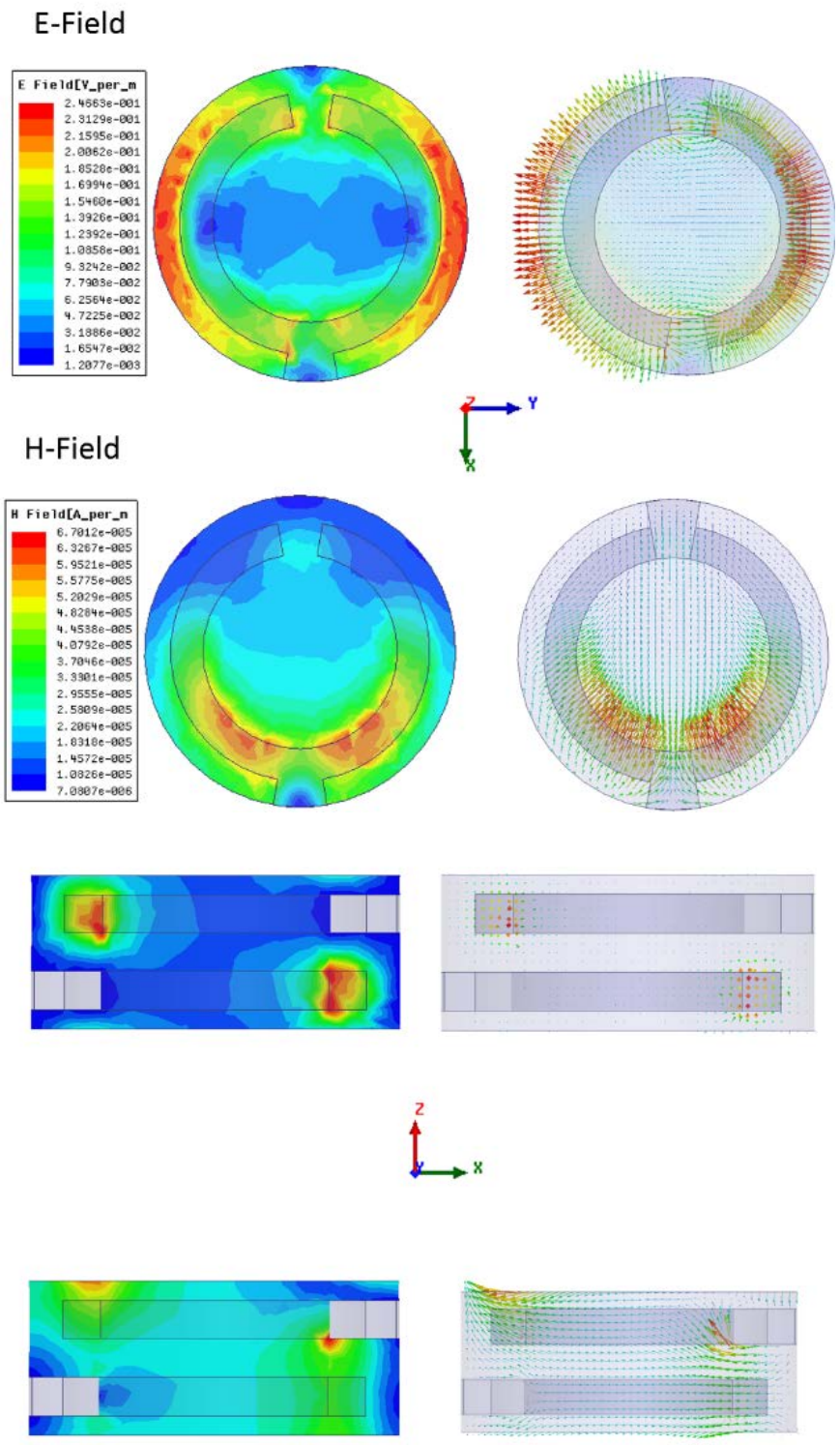

Figure 4.6 Field characteristics (vector and contour plots of E-field and H-field).

It is also helpful to analyze charge and current densities of the structure using HFSS. As we mentioned earlier in Chapter 2, SRR structures show strong capacitive behavior around the gaps of the rings due to the orbital current and the current density is concentrated in the continuous SRR branches. Figure 4.7 shows a current density plot in vector and contour form and Figure 4.8 shows charge density plots for the negative dispersion mode. For the sake of clarity of images, they are shown in two color format. However, the behavior of the structures should be studied in more detail because of the complexity of the results.

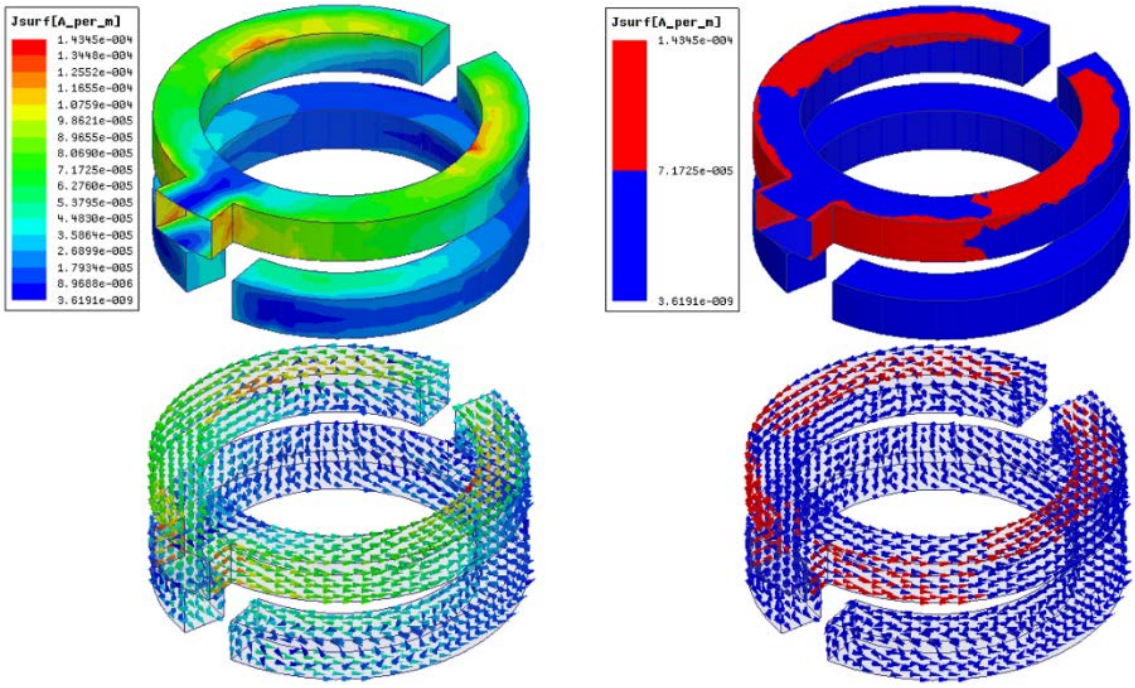

Figure 4.7 Vector and contour plot of current density.

In Figure 4.8, charge density has a symmetric behavior around the gaps, and each half of the rings have charge in a different sign near the gaps.

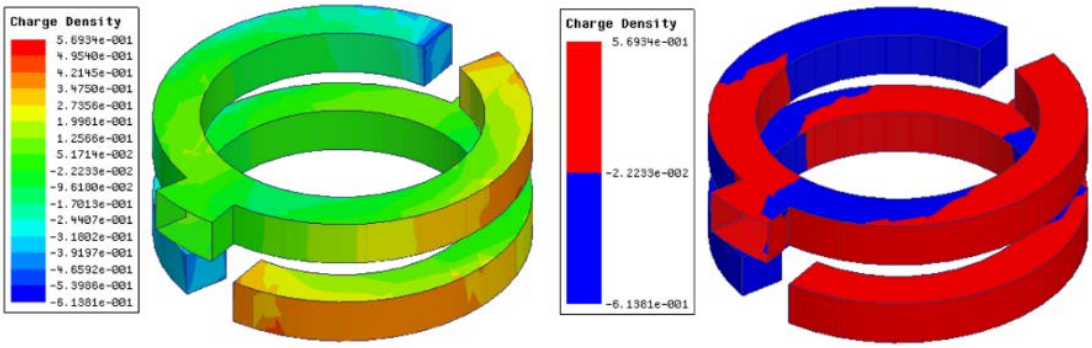

Figure 4.8 Charge density plot.

It can also be shown that the wave propagates in the backward direction and it can be seen with the E_z component of the electric field (as shown in Figure 4.9.) that is an important parameter which affects the interaction impedance significantly.

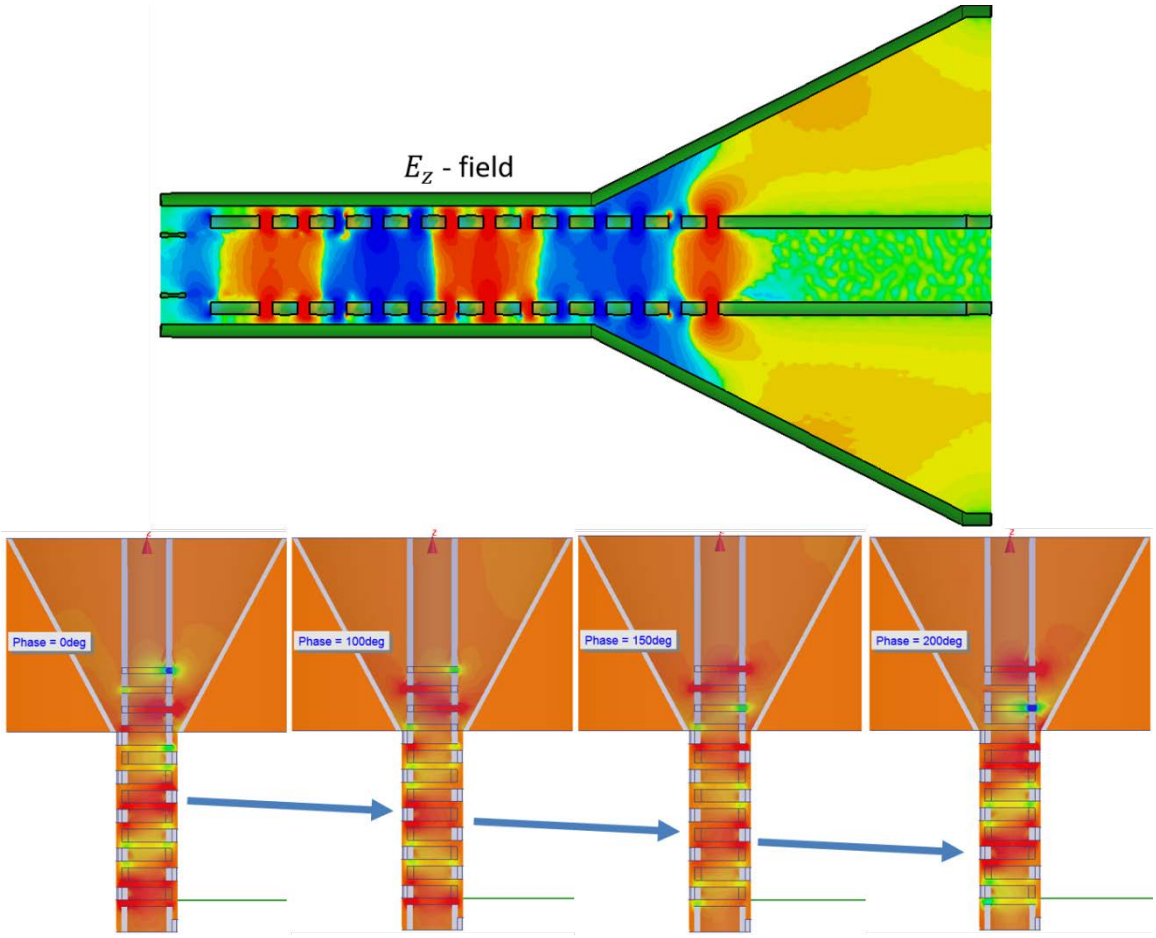

Figure 4.9 Propagation of wave with changing phase for E_z component of the E-field.

From the field characteristics, we can also say that most of the power is stored between ring outer and waveguide inner wall and last three rings along with output horn allow to extract higher power efficiently.

4.3.2. S-Parameter Simulation for Extraction of Constitutive Parameters

S-parameter simulations have been performed using the HFSS driven modal solution for a unit unit cell of the BCSRR structure. The boundary conditions were defined according to a free space metamaterial configuration without a waveguide. Two PEC boundary conditions were placed parallel to the gaps of the rings and two PMC boundaries were defined perpendicular to the gaps. The direction of wave propagation is obtained by defining two wave ports for the 2nd lowest mode of the structure, which is the mode we are interested in. All these simulation settings are illustrated in Figure 4.10. Unfortunately, there is no literature for extraction of constitutive parameters for all metallic structures that are used in HPM systems to be able to compare the results.

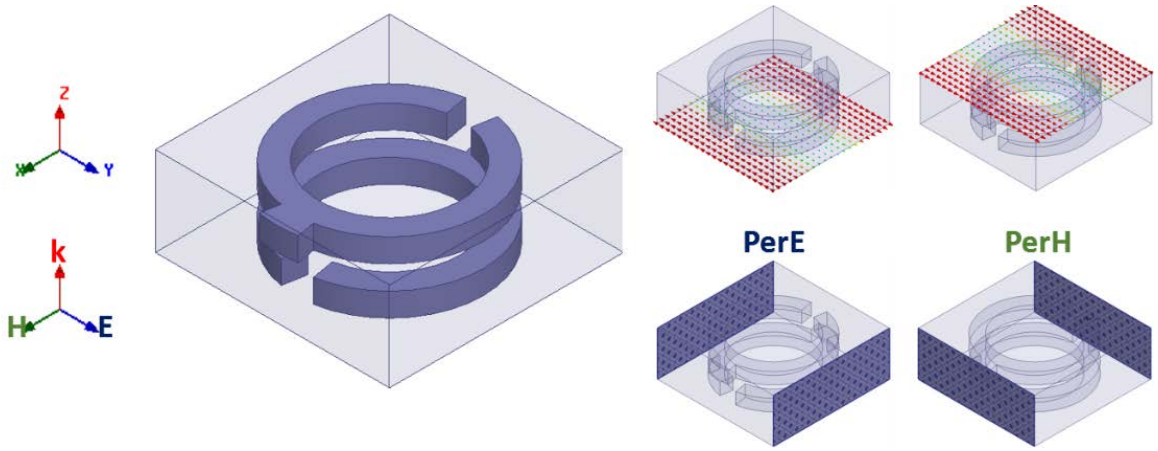

Figure 4.10 Simulation boundary setup for retrieval process.

After we calculate the magnitude and phase of the S-parameters by simulating the unit cell structure, we can retrieve the constitutive parameters. Figure 4.11 shows all

retrieved parameters, including permittivity, permeability, and magneto-electric coupling coefficient. It can be easily seen from Figure 4.11 h) that double negative behavior occurs in the frequency range of 1-3 GHz which covers our operating frequency. It also shows nonbianisotropic behavior between 1-2 GHz.

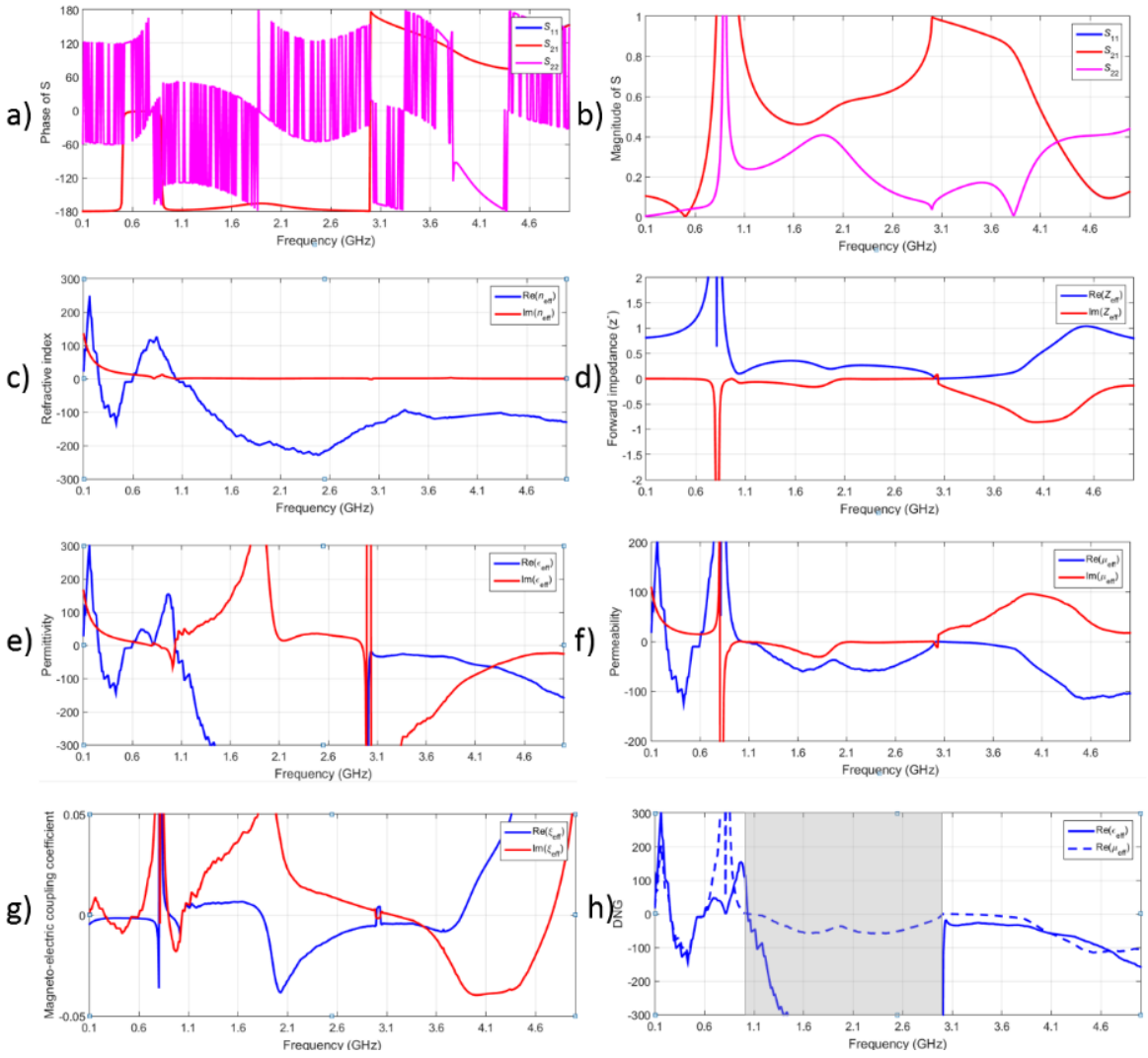

Figure 4.11 Retrieved material parameters a) phase of S-parameters, b) magnitude of S-parameters, c) refractive index *n*, d) impedance *Z*, e) effective permittivity ε_{eff}, f) effective permeability μ_{eff}, g) magneto-electric coupling coefficient ξ_{eff}, h) double negative region.

Another analysis has been performed for the preparation of cold-test experiments with a simulation of the structure that consists of different unit cells in order to find transmission and reflection coefficients and find the optimum dimension of the entire structure. In Figure 4.12 S-parameters are calculated using wave port excitation from both ends of the tube for the whole structure that consists of 10 unit cells and 20 rings. It shows passband characteristics between 0.80-1.76 GHz and stopband characteristics between 1.8-3.4 GHz. These results are in very good agreement with previously calculated dispersion characteristics of the structure. It has one negative and one positive mode in the region of the passband and no mode in the region of the stopband.

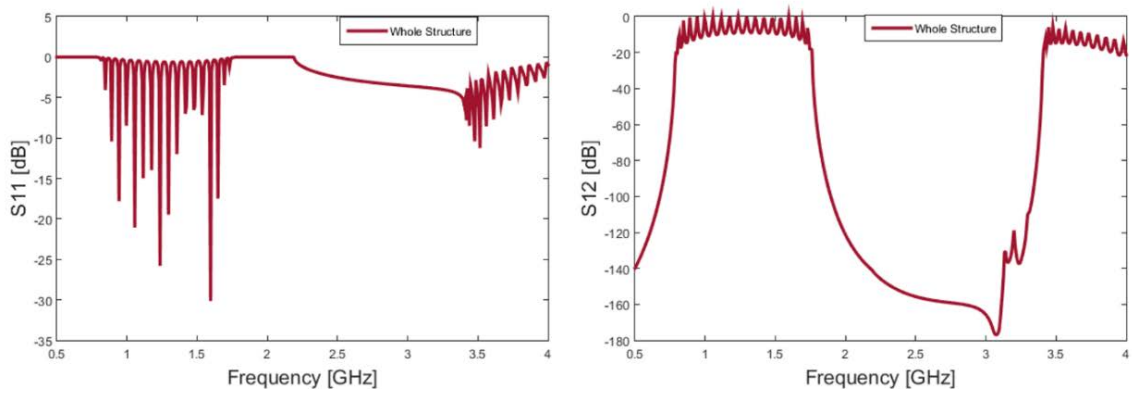

Figure 4.12 Reflection and transmission coefficients of the entire structure that show passband and stopband.

Although it is not obvious from Figure 4.13, the 10-unit cell structure shows clearer passband and stopband behavior compared with shorter structures. For this reason, we chose 10 as the optimal number of rings.

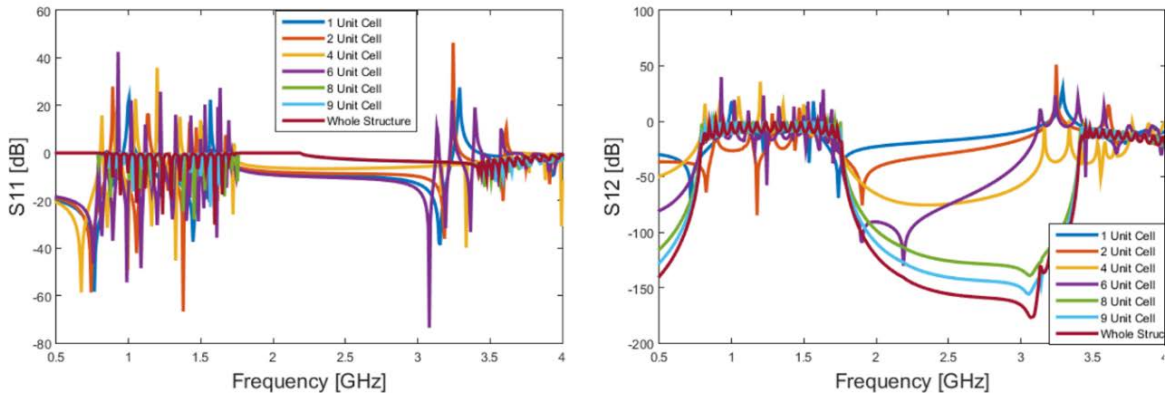

Figure 4.13 Reflection and transmission coefficients of the structure with different unit cells.

4.4.Hot Test (Particle-in-cell Code) Simulation Results

Using the 3D MAGIC PIC code, hot test simulations have been performed in order to calculate output power, anode current, and frequency of the RF signal. Before showing the hot test simulation results for the structure shown in Figure 4.14, which is the optimal case, results are presented for two different scenarios: coaxial output from the tube's cross section and conical coaxial output with a horn antenna added in order to show the design progress here. For the first case with a coaxial output, the $r - z$ plane cross-section view of the interaction space is given in Figure 4.14. Figure 4.15 shows waveforms of radiation power P (a) around 100 MW, the radiation frequency (b) at 1.4 GHz, voltage (c) 400 kV, and anode current (d) 5 kA as functions of time for an applied guide magnetic field $B = 2$ T. Results are obtained with the red annulus representing the electron beam of voltage $U = 400$ kV and risetime $\tau = 2$ ns that enters the interaction space with only longitudinal velocity. The risetime of the output radiation is approximately 5 ns. This is a very important result since the SINUS-6 voltage pulse is on the order of 10 ns (Figure 4.16). (Previous researchers studying a MSWS in a BWO configuration observed very long

risetimes, over 100 ns, a characteristic of MSWS [48].) The output power is 100 MW after saturation.

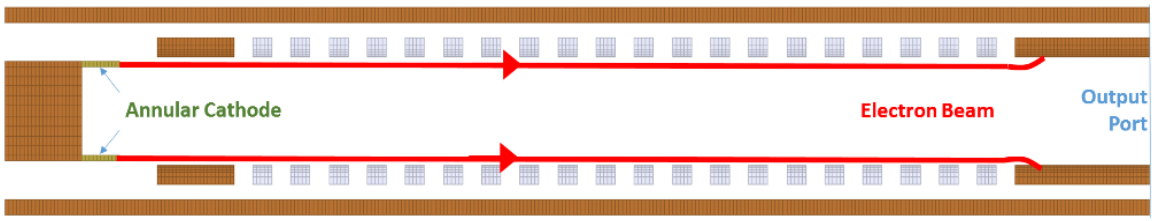

Figure 4.14 Early configuration of a MSWS for PIC simulation.

The frequency of the output radiation is close to that of the TE-like mode. The maximal efficiency achieved is about 5% with 100 MW output power. However, there are some higher order modes excited along with main operating mode, and mode competition is an undesired feature for HPM devices.

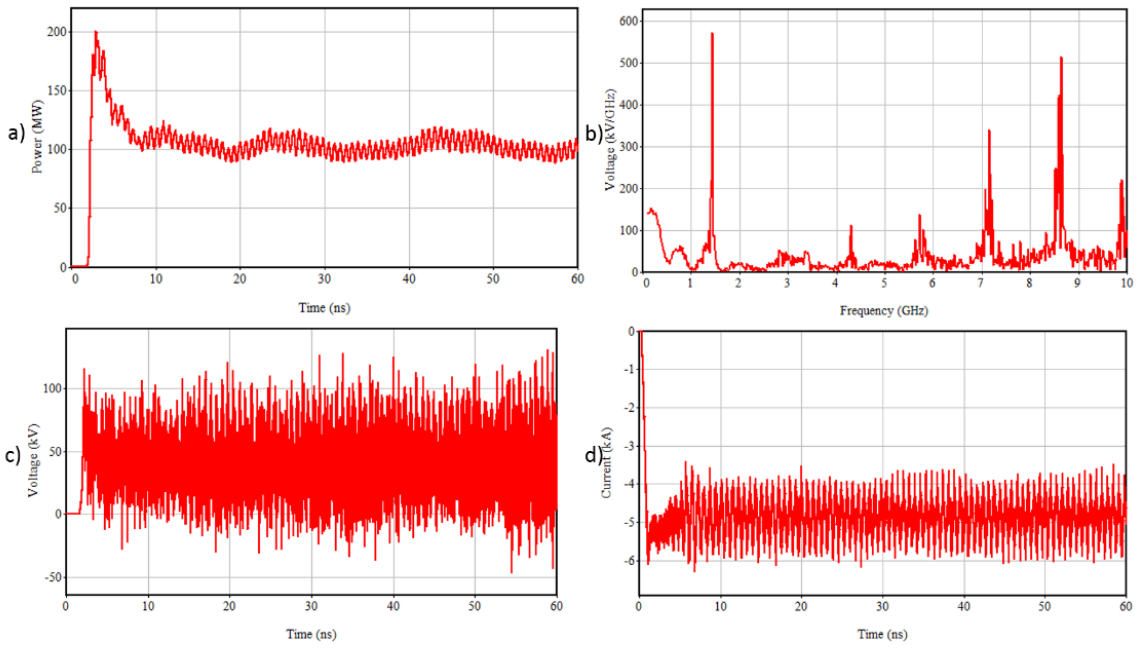

Figure 4.15 3D MAGIC hot test results: a) output power, b) FFT of RF signal, c) voltage, d) anode current.

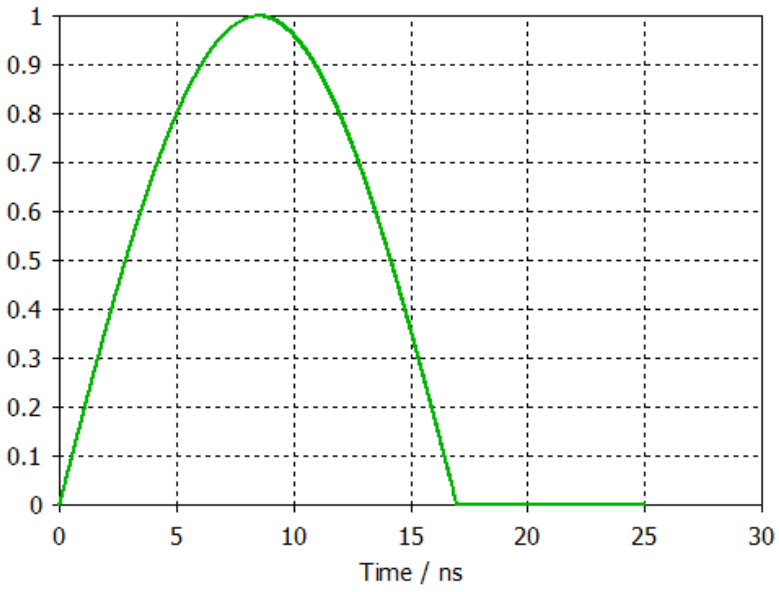

Figure 4.16 SINUS-6 voltage waveform.

Our goal is to increase the efficiency by optimizing the beam and magnetic field parameters, and the device dimensions. For this reason, we added an extended output element which is a conical horn and extended hollow metal tube up to the end of output port as it is shown in Figure 4.17.

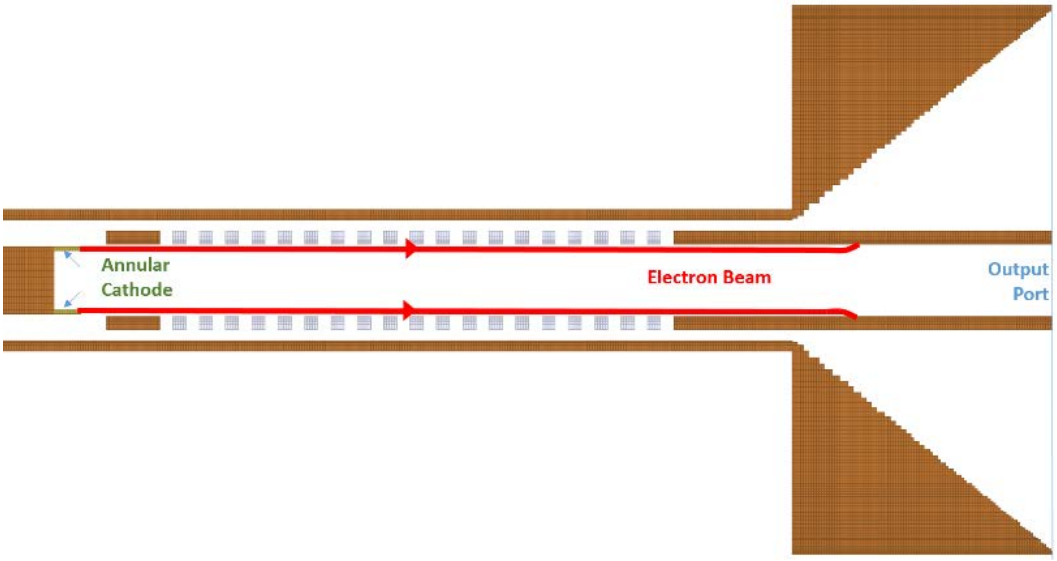

Figure 4.17 Geometry of the MSWS for hot test simulation with the extended output to facilitate extraction.

Figure 4.18 shows the waveforms from the PIC simulations: radiation power P (a) around 400 MW after saturation, radiation spectrum (b), voltage (c) and anode current (d) 3.5 kA. Although we achieved higher efficiency, up to 30% after 5 ns saturation time with high output power, again we could not obtain a clean FFT of the RF signal.

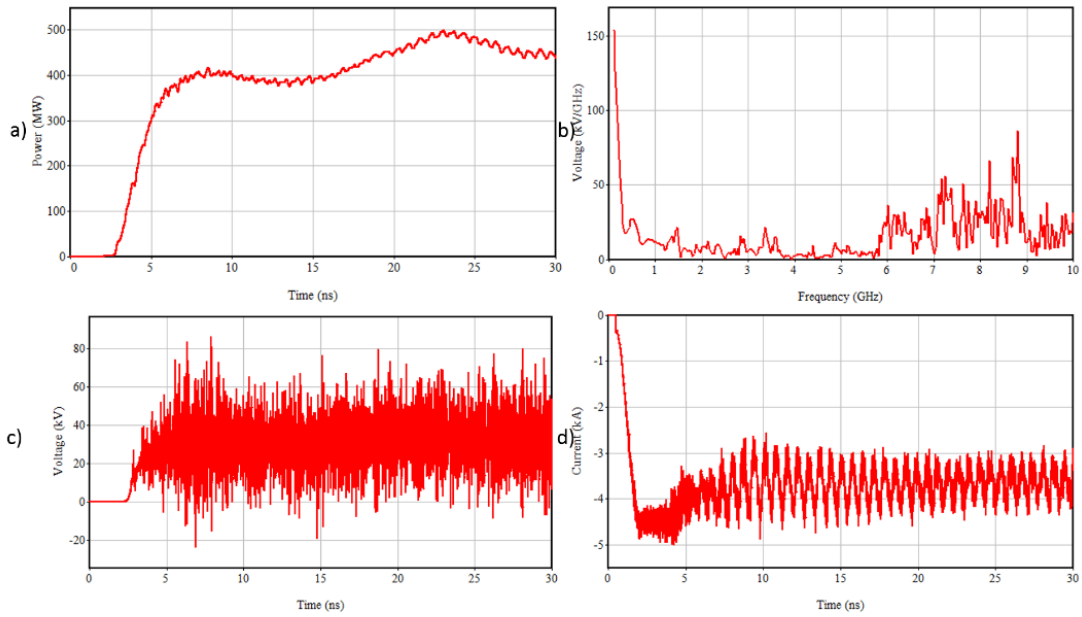

Figure 4.18 3D MAGIC hot test results: a) output power, b) FFT of RF signal, c) voltage, d) anode current.

Finally, we achieved the optimal design (Figure 4.3) that provides relatively higher efficiency and a clean frequency spectrum without mode competition. Figure 4.19 shows waveforms, with radiation power P with maximum 260 MW, anode current I_A with maximum 5.3 kA, and radiation frequency $f = 1.4$ GHz for an applied guide magnetic field $B = 2$ T. In order to verify the MAGIC PIC code simulation results, we modeled the same structure using CST Particle Studio. Figure 4.19 shows a comparison of the output power and FFT of the RF signal obtained from both codes. Both PIC code simulation results are

in very good agreement. We compare the numerical calculation of current with simulation results in Table 4.4.

Table 4.4 Comparison of anode current calculations.

Beam Current Comparison	Based on Equation (4.1)	CST	MAGIC PIC Code
Value	5.46 kA	5.28 kA	5.33 kA

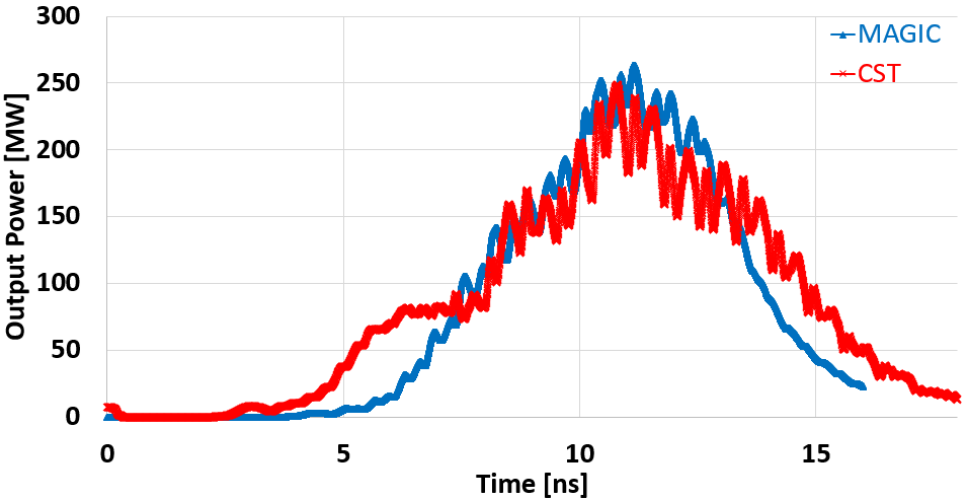

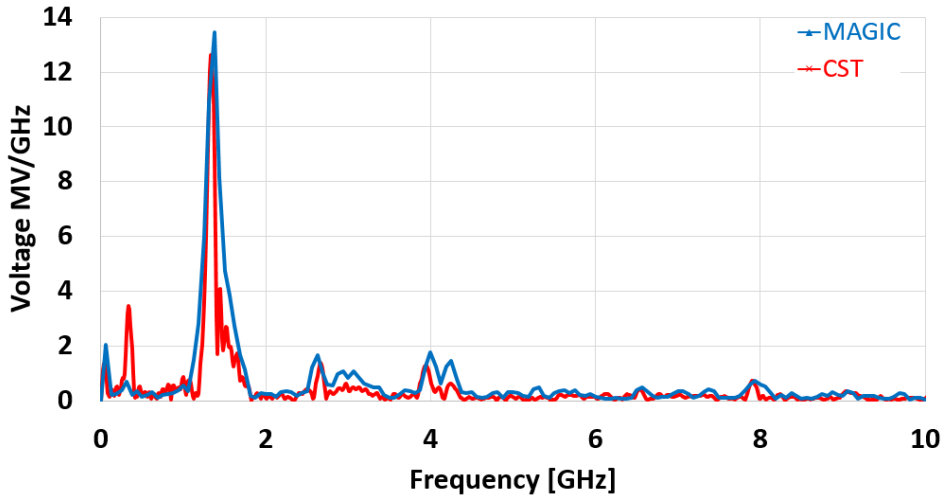

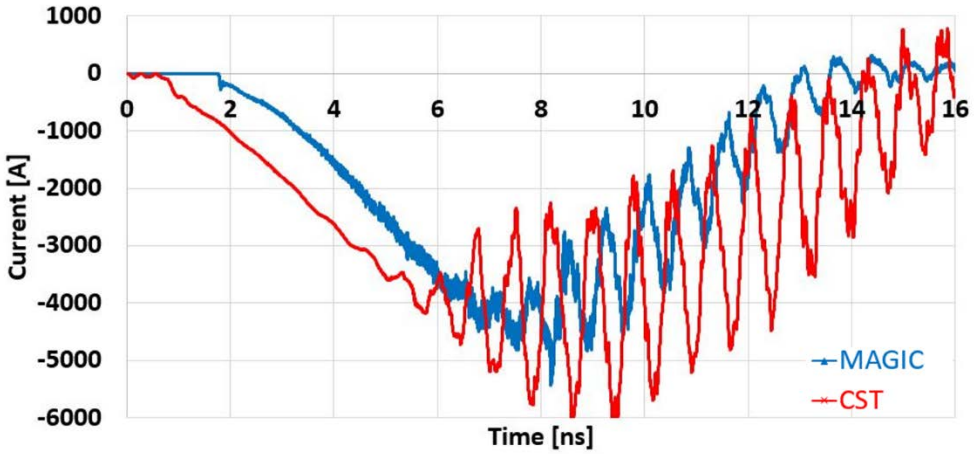

Figure 4.19 CST and MAGIC PIC simulations output: Top: radiation power P; middle: radiation spectrum; bottom: anode current.

The pattern of the output radiation is close to that of the TE_{21}-like mode (Figure 4.20). The maximal efficiency achieved is about 15%.

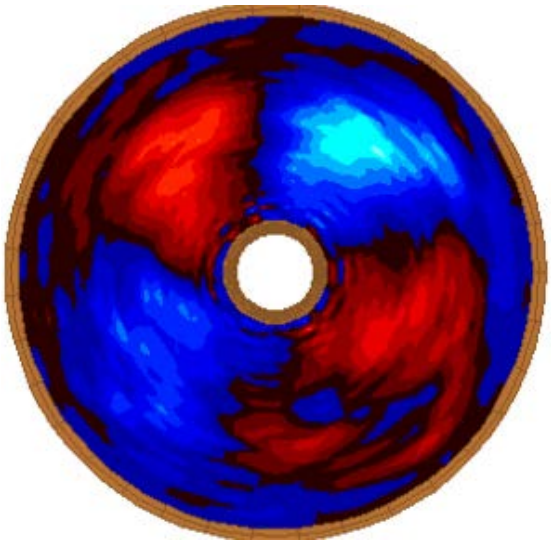

Figure 4.20 Output radiation pattern E_ϑ at the output port.

Figure 4.21 shows plots of particle momentum p_z along the axial length of the MSWS. In our system, particle behavior is similar to particle behavior as a virtual cathode forms. The evanescent wave leads to the formation of electron traps that exhibit a resonant particle distribution similar to that of a virtual cathode when the space-charge-limited

current is exceeded by the beam current (although this is not the case here). Since the wave is evanescent, the generated microwaves reach the ends and reflect back; eventually in time, the electron cloud forms two electron bunches that are approximately $\lambda/2$ apart. This is a consequence of evanescent wave behavior.

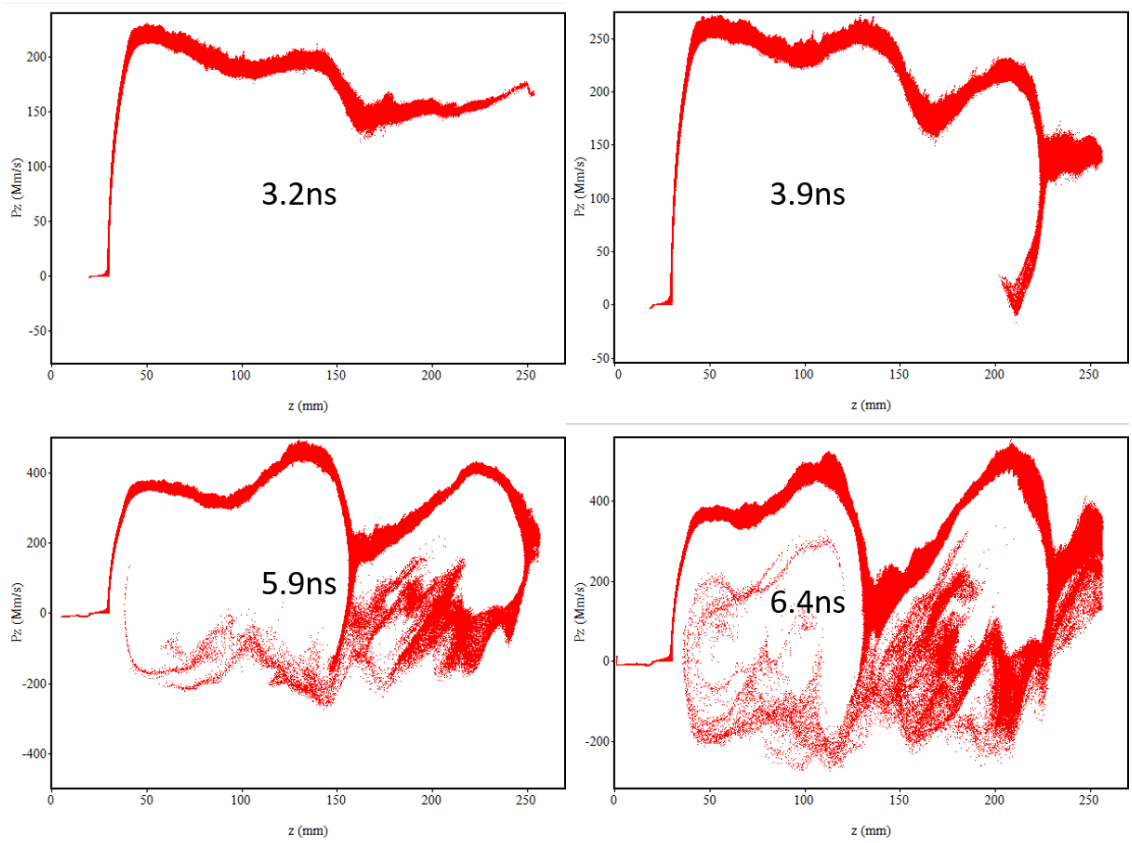

Figure 4.21 Plot of particle momentum p_z along the axial length of the MSWS.

Device performance can be improved by optimizing the reflection mechanism of the structure. In Figure 4.22 it shows an improved 18% efficiency and 310 MW output power by adding a solid ring for better reflection and extending the cylindrical waveguide that is placed before the ring.

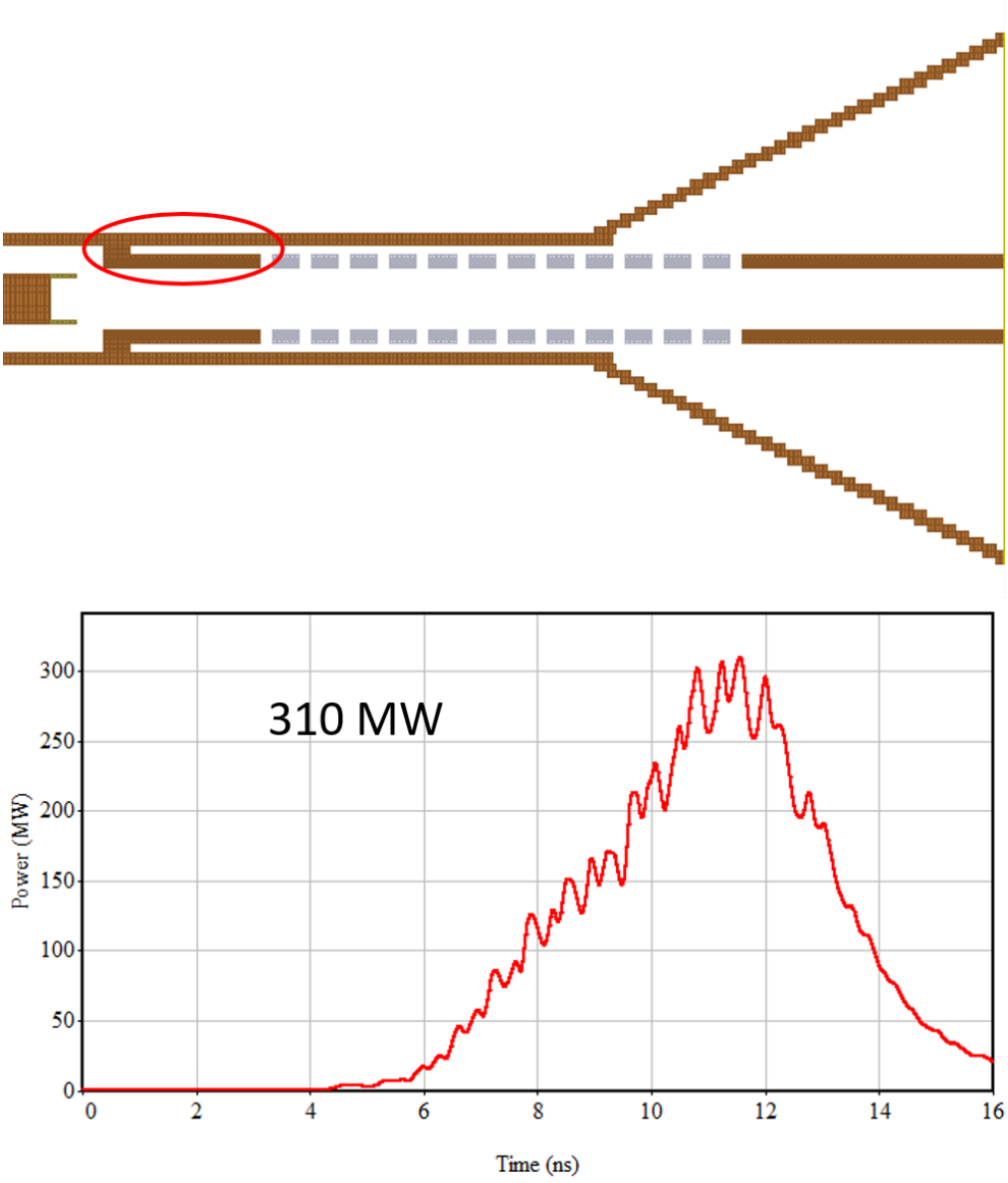

Figure 4.22 Improved efficiency after optimizing the reflection of the system. Top: improved design of MSWS, bottom: Output power plot function of time.

In order to verify device performance (saturation and start time) a flat excitation signal (Figure 4.23) was used instead of the SINUS-6 voltage waveform in additional hot test simulations. According to the simulation results, a fast start time of 4 ns reaching saturation promptly after 10ns is shown in Figure 4.24 for the 100 ns long simulation. 250 MW output power (Figure 4.24) is obtained similar to previous simulations.

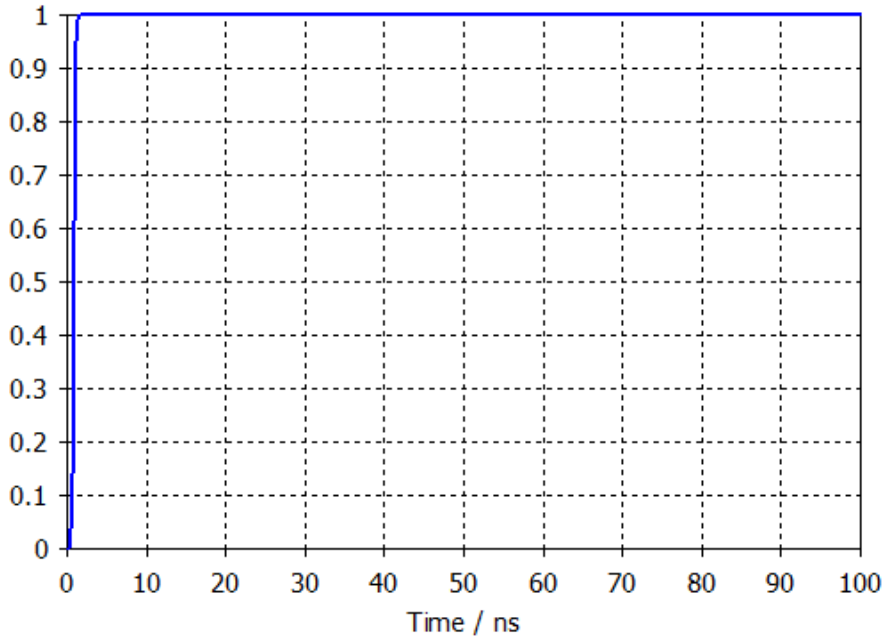

Figure 4.23 Flat excitation signal with 1 ns rise time.

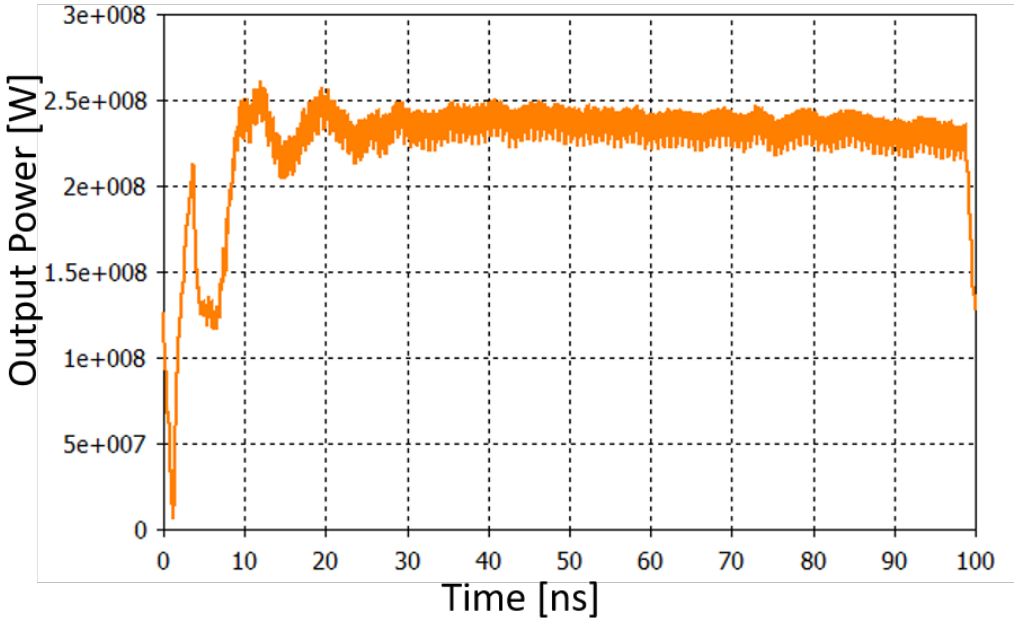

Figure 4.24 Output power calculation with the flat excitation signal.

CHAPTER 5: EXPERIMENTAL SETUP AND RESULTS

5.1. Cold Test Setup and Measurement Results of the BCSRR

The parameter extraction technique discussed in the previous section verified that the MSWS was a double negative structure. In order to confirm this in experiment, a crude prototype MSWS was first constructed using a water jet-cut copper SRRs. We used a network analyzer for the cold test that provides an electromagnetic pulse as a source which is transformed to a particular mode of the structure under test. The geometry of the mode launcher consists of a loop antenna which is fed coaxially. A pair of mode launchers is placed at both ends of the MSWS as a transmitter and receiver. Figure 5.1 shows a photograph of this set-up.

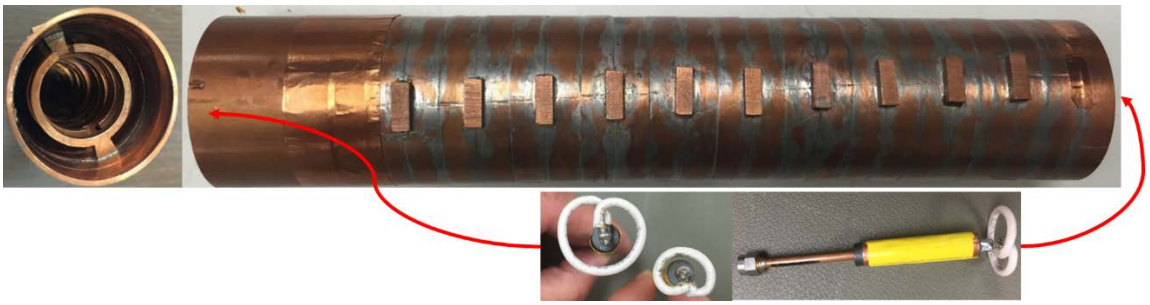

Figure 5.1 Experimental setup of the structure with two mode launchers.

We then performed typical transmission and reflection measurements of the MSWS loaded with rings using two mode launchers. Both experimental and simulation results are in good agreement, and they show passband and stopband in the same frequency region as indicated in Figure 5.2, despite the crude construction technique used to fabricate the prototype MSWS.

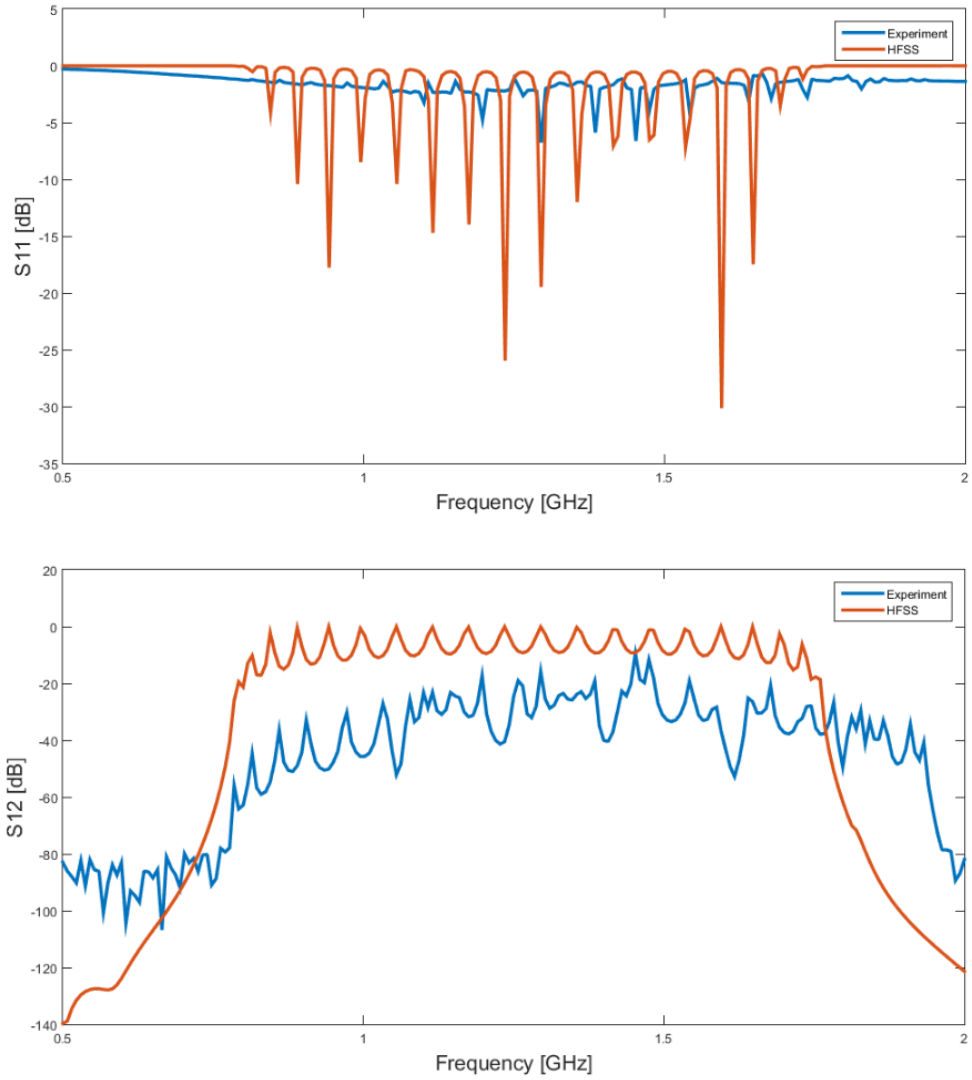

Figure 5.2 S_{11} and S_{12} measurement of the MSWS that shows the first passband between 0.76 – 1.76 GHz for both experimental and simulation cold tests.

After we find the S-parameters, the constitutive parameter retrieval process is performed, and the results are given in Figures 5.3. According to retrieved material parameters, we ended up with a double negative region between 1.32 – 1.5 GHz which covers our operating frequency. It is a remarkable achievement that shows the double negative behavior of a novel design MSWS.

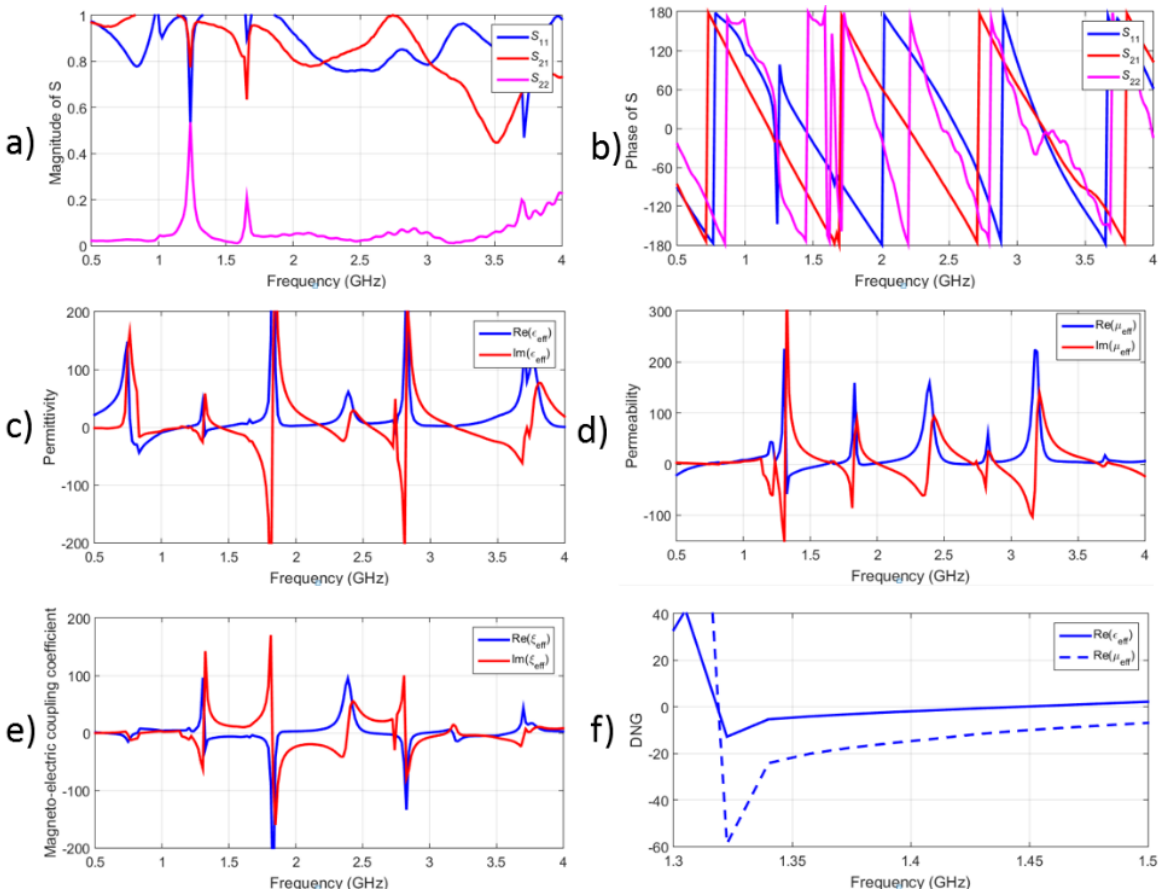

Figure 5.3 Retrieved material parameters a) phase of S-parameters, b) magnitude of S-parameters, c) effective permittivity ε_{eff}, d) effective permeability μ_{eff}, e) magneto-electric coupling coefficient ξ_{eff}, f) double negative region.

5.2. Hot Test Experiment

5.2.1. Experimental setup

The components of hot test experiment are summarized in Figure 5.4 for a typical HPM system with the MSWS as the load.

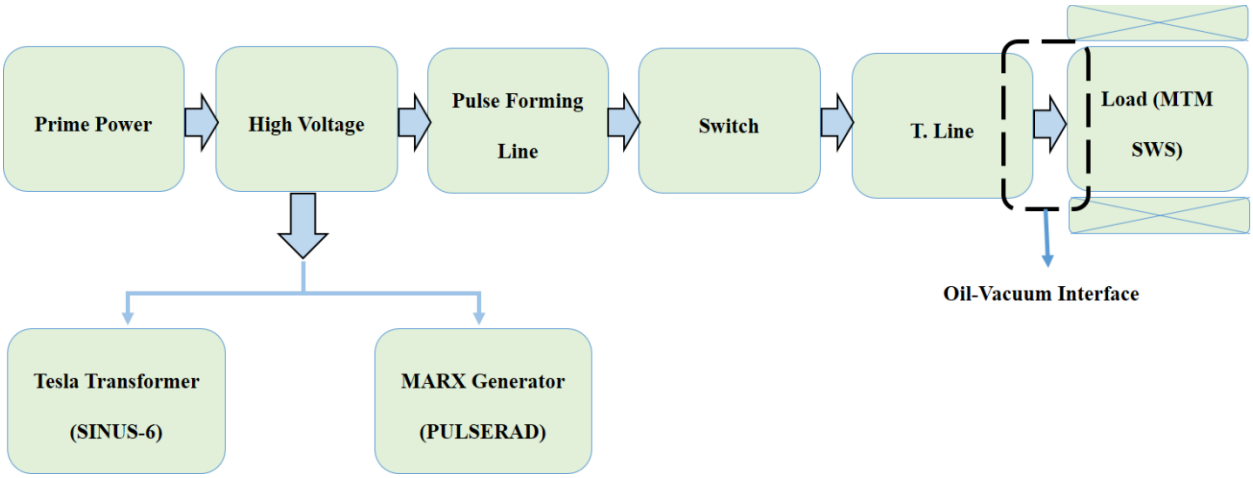

Figure 5.4 Block diagram of HPM components for the experimental plan.

Pulse forming lines (PFLs) that are driven by a capacitor bank are the most commonly used pulsed power systems for HPM devices. When the high voltage is switched onto the PFL, energy is released at the speed of light. There are two common types of pulsed power systems used in HPM: a Marx generator that drives a PFL or a capacitor bank as a low voltage that drives a Tesla transformer generating short pulse, high voltage pulses to power an electron beam diode. In a Marx generator, capacitors are charged in parallel and discharged quickly in series through fast switching in order to provide high voltage to the system. High voltages can be achieved by increasing the number of capacitors that are in parallel. This may lead to an increase in the size of the system. An oil-filled transmission line is commonly used as an essential part of the system in order to take the fairly long output from the Marx (about 1 μs) and shape it to a flat-top, 10s-100s ns pulse.. Marx generators usually cannot work in a high repetition rate regime, but Tesla transformer-based pulsed power systems can. For relatively shorter pulses (<200 ns), PFLs are used. If there is a need for longer pulses then pulse forming networks (PFNs) can be used. A

schematic of a PFL in the context of a Marx generator-based system is shown in Figure 5.5 [1].

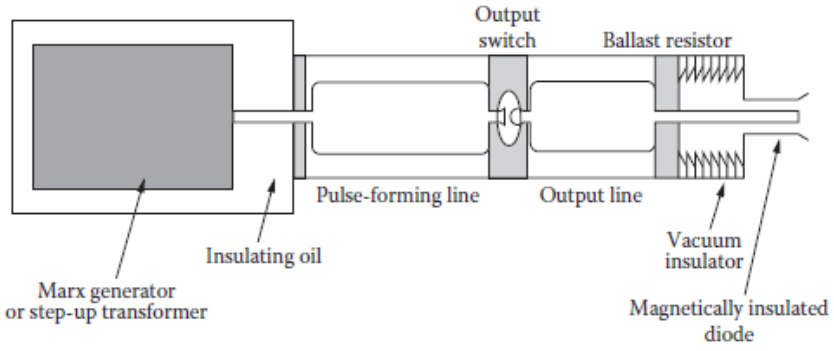

Figure 5.5 Schematic of a PFL [1].

Spark gaps with a gas dielectric are the most common switching mechanisms of Marx/PFLs. It is important to have well-designed spark gaps in order to achieve accurate repetitive operation without having problems related to heat or remains around the electrodes. Nitrogen gas breakdown switches are commonly used as high-pressure spark gap switches.

For the experiment of proposed structure at UNM, we use the SINUS-6 Tesla transformer-based electron beam accelerator as the high voltage source [86]. It will be explained in more detail next.

SINUS-6 (Tesla Transformer)

The SINUS-6 transformer-based electron beam accelerator consists of the low power source as a prime power (capacitor banks charged by the line voltage), pulsed transformer, oil-insulated PFL, high voltage gas spark gap, tapered transmission line,

vacuum-oil interface, and cathode. Illustration of the SINUS-6 configurations is given in Figure 5.6 [1, 87].

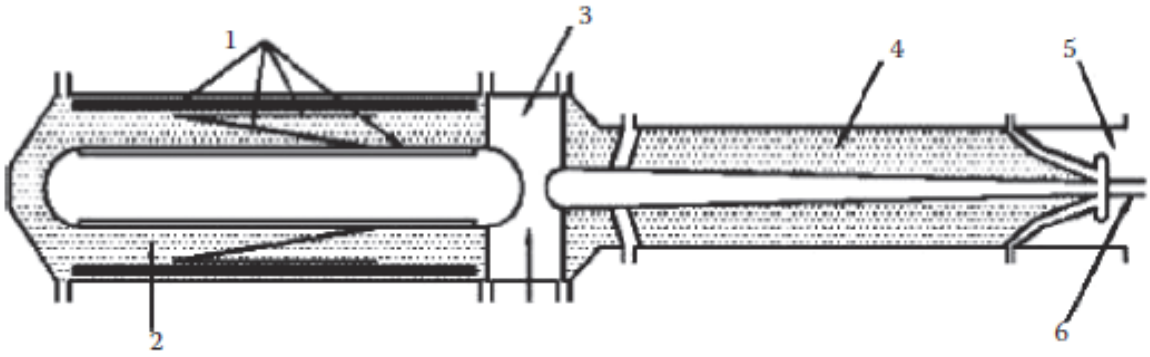

Figure 5.6 Illustration of the SINUS-6 configuration: 1) Tesla transformer for pulsed high voltage, 2) oil-insulated PFL, 3) high voltage gas spark gap, 4) tapered transmission line, 5) vacuum, and 6) diode region [1].

The operation of the SINUS-6 at UNM in the single shot regime is relatively straightforward. The 208 three phase line voltage source provides the continuous power that is used to charged a bank of capacitors. The capacitor bank that includes six parallel capacitors (3 mF) for prime power are charged and provides 300 V input to the transformer. With the help of highly efficient coupling between the transformer turns that have 1:3500 ratio, the input voltage can rise to 700 kV level with up to 7 kA current. The PFL then shapes the output pulse in terms of the rise and fall times, and determines the duration of the pulse which is about 12 ns as an input to the system. Because of the system design requirements the output impedance of the Tesla transformer is 20 Ω. Since its low impedance is undesirable for most of the BWO devices that have an impedance around 100-150 Ω it needs to be matched using a tapered transmission line. Transformer oil is used to insulate high voltage and avoid any breakdown. The relation between the length of the transmission line, L (m) and the duration of electron beam pulse τ_{BEAM}(ns) is

$$L = \frac{3}{2}\, c'\tau_{\mathrm{BEAM}} \tag{5.1}$$

where c' is the reduced speed of light with the ratio of dielectric constant of insulating oil and its value is $2{\times}10^8$ m/s. Illustration of the tapered transmission line is given in Figure 5.7.

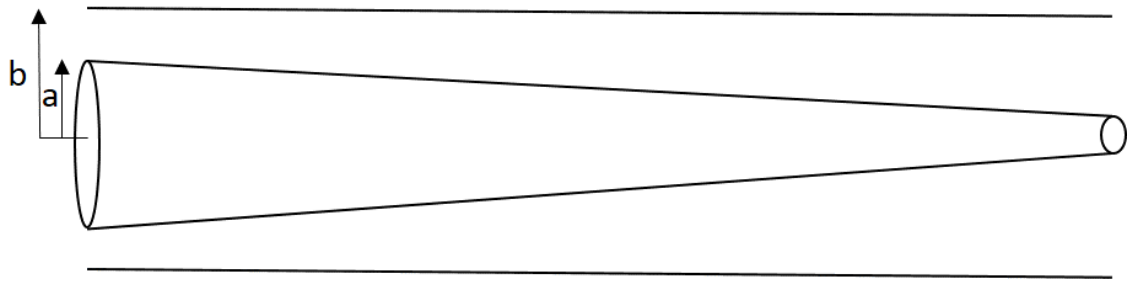

Figure 5.7 Illustration of the tapered transmission line section used in the PFL.

The impedance of the coaxial transmission line depends on the dielectric constant of the insulating oil and the geometry of the conductors via

$$Z_0 = \frac{60}{\sqrt{\varepsilon_r}} \ln\left(\frac{b}{a}\right) \tag{5.2}$$

where $\varepsilon_r = 2.1$ (for oil), b is the radius of outer conductor and a is the radius of the inner conductor.

The impedance and power flow relations are given by

$$P_{\mathrm{BEAM}} = \frac{V_0^2}{Z_{\mathrm{BWO}}} \tag{5.3}$$

where

$$V_0 = V_{\mathrm{PFL}} \left(\frac{Z_{\mathrm{BWO}}}{Z_{\mathrm{PFL}} + Z_{\mathrm{BWO}}}\right). \tag{5.4}$$

The maximum power transfer can be achieved when the impedances of PFL and BWO are matched

$$P_{\mathrm{BEAM,max}} = \frac{V_{\mathrm{PFL}}^2}{4Z_{\mathrm{BWO}}}. \tag{4.4}$$

Using a tapered transmission line in order to match the impedance increases the system efficiency. The only disadvantage of having a tapered transmission line is that it increases the length and size of the system significantly. It is one of the important design trade-offs of the SINUS-6 Tesla transformer-based system. The overall efficiency of the system depends on not only impedance matching but also pulsed power and microwave source efficiencies. The SINUS-6 electron beam accelerator has 90% efficiency that can allow transferring most of the stored energy to the beam.

The oil-vacuum interface is used to separate the end of the oil-filled tapered transmission line with the vacumm diode, and consists of three different materials: dielectric, metal, and vacuum, as shown in Figure 5.8. Backstreaming electrons get trapped by the tapered cathode shank and prevent damage to the oil-vacuum interface.

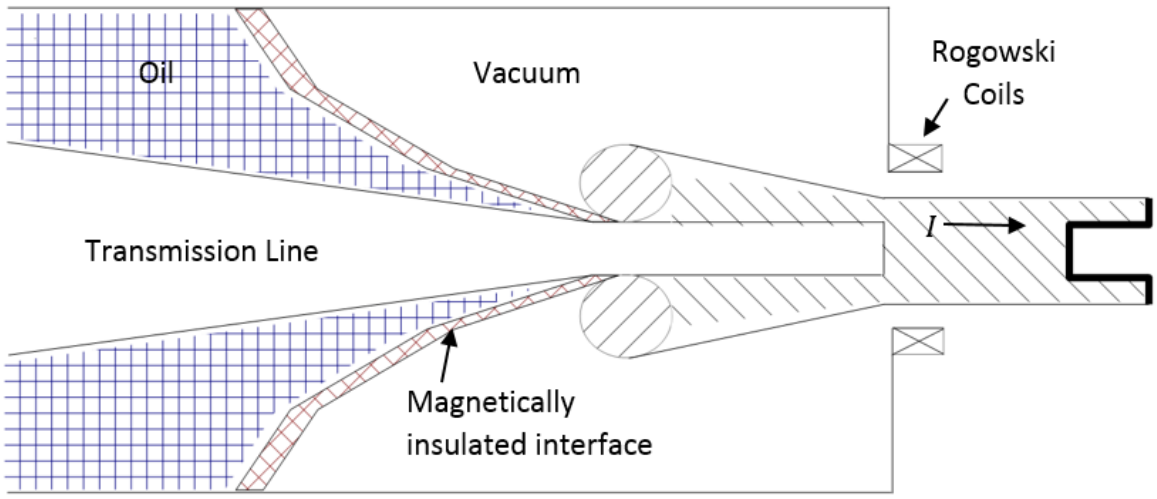

Figure 5.8 Sketch of the oil-vacuum interface.

The input parameters for hot test are given again with previously calculated values:

$$V_{\text{in}} = 400 \text{ kV}$$

$$I = J.dA = \ 5.3 \text{ kA}$$

$$P_{\text{in}} = 400 \text{ kV} \times 5.3 \text{ kA} = 2.1 \text{ GW}$$

$$Z_{\text{in}} = \frac{V_{\text{in}}}{I} = 400 \text{ kV} / 5.3 \text{ kA} = 75 \ \Omega$$

$$B - \text{field} = 2 \text{ T (9 solenoidal coils)}.$$

A 2 T magnetic field guides the electron beam along with longitudinal axis of the structure. The solenoid that provides the magnetic field was designed using the FEMM software, the field lines are and shown in Figure 5.9. According to this design, approximately 1.9 T magnetic field is achieved after two solenoids and starts guiding the electrons until it reaches the collector side and dumps the electrons to the wall.

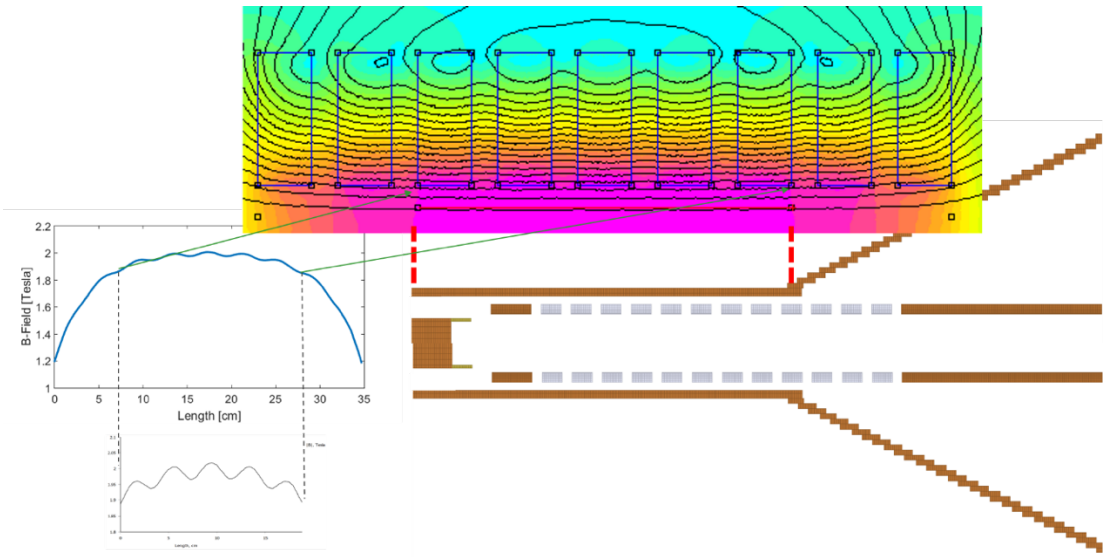

Figure 5.9 Design of the guide magnetic field with solenoids using the FEMM software.

5.2.2. Diagnostics

The following diagnostics are used in the MSWS experiment:

Diode Diagnostics

a) Voltage (capacitive divider)

b) Current (Rogowski coil)

Microwave Diagnostics

c) Microwave power (scanning waveguide detector and integrating the signal)

d) Microwave frequency (FFT of the RF signal)

e) Mode detection (neon grid array)

A precision MSWS was fabricated for experimental hot tests, and is shown in Figure 5.10.

Figure 5.10 Photograph of the interior of the precision-manufactured MSWS for hot test experiments.

5.2.3. Experimental Hot Test Results

Experiments were led by Dr. Sarita Prasad with assistance from undergraduate students Dmitrii Andreev and Daniel Reass, and we include these results here for completeness. Due to a damage on the plastic oil-vacuum interface (evidence of arcing) experiments had to be performed at a reduced voltage in order to avoid electrical breakdown. Therefore, MAGIC simulations were performed by Dr. Prasad at the reduced input parameters with the set-up shown in Figure 5.11 and results shown in Figure 5.12.

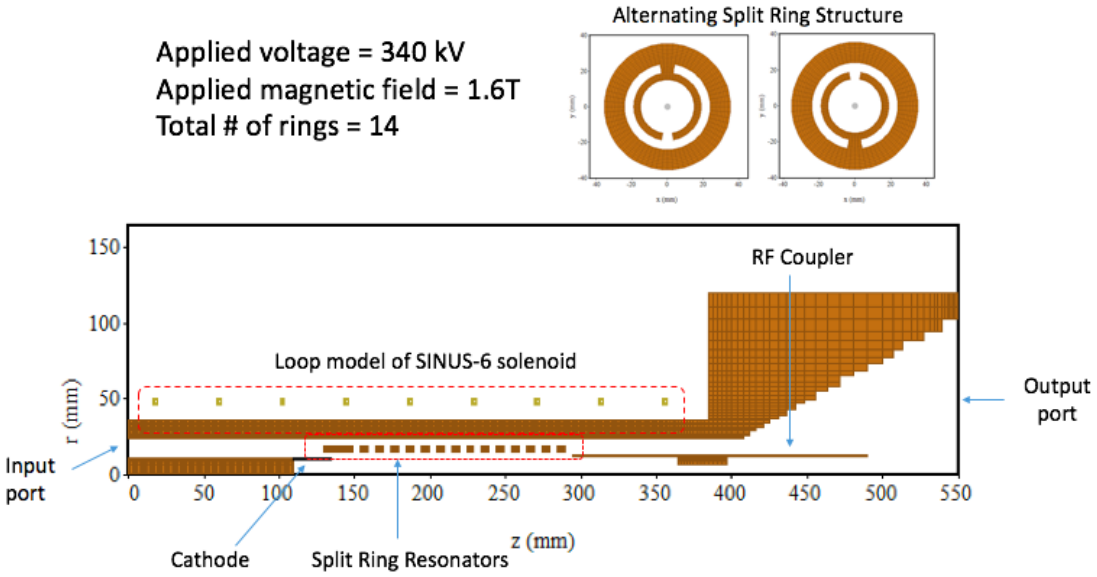

Figure 5.11 MAGIC PIC simulation set-up of the MSWS used in experiments and driven by reduced voltage and current to avoid breakdown.

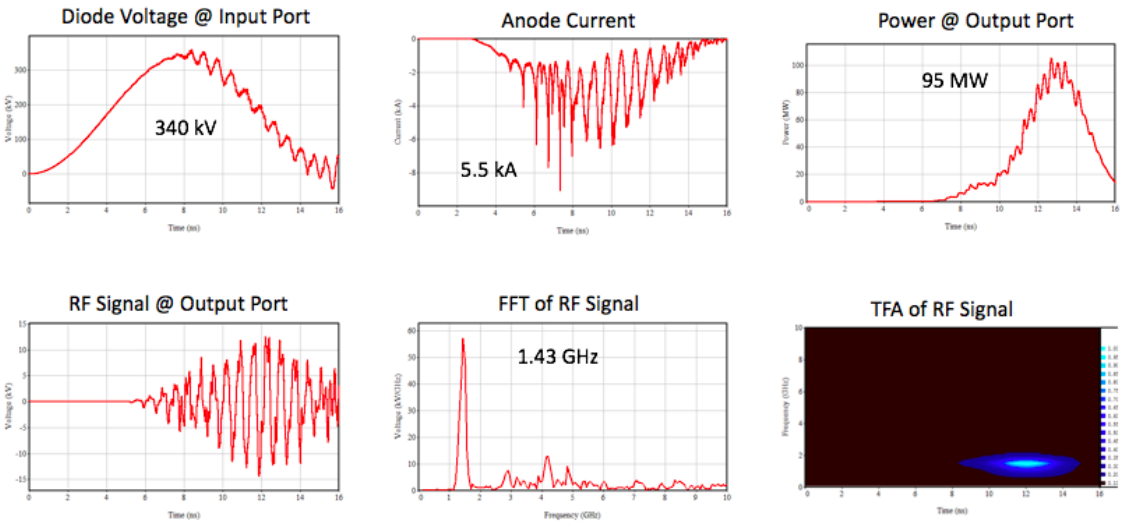

Figure 5.12 Results from the MAGIC PIC simulation of the MSWS used in experiments and driven by reduced voltage and current to avoid breakdown.

The experimental set-up is shown in Figure 5.13 and a summary of the experimental results is shown in Figure 5.14. There is excellent agreement between the MAGIC simulations and the experimental results. In order to obtain power measurements the output mode pattern needs to be mapped in order to properly integrate the power density. This was not possible during this initial run, but it is estimated that the output power in the experiment is of the order of 100 MW. More careful measurements need to be performed in the future once the new oil-vacuum interface is installed.

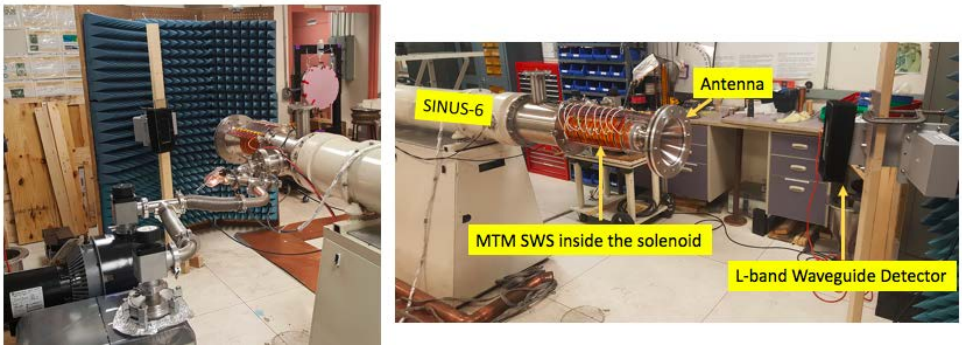

Figure 5.13 Photograph of the experimental set-up for hot tests of the MSWS using the SINUS-6 accelerator.

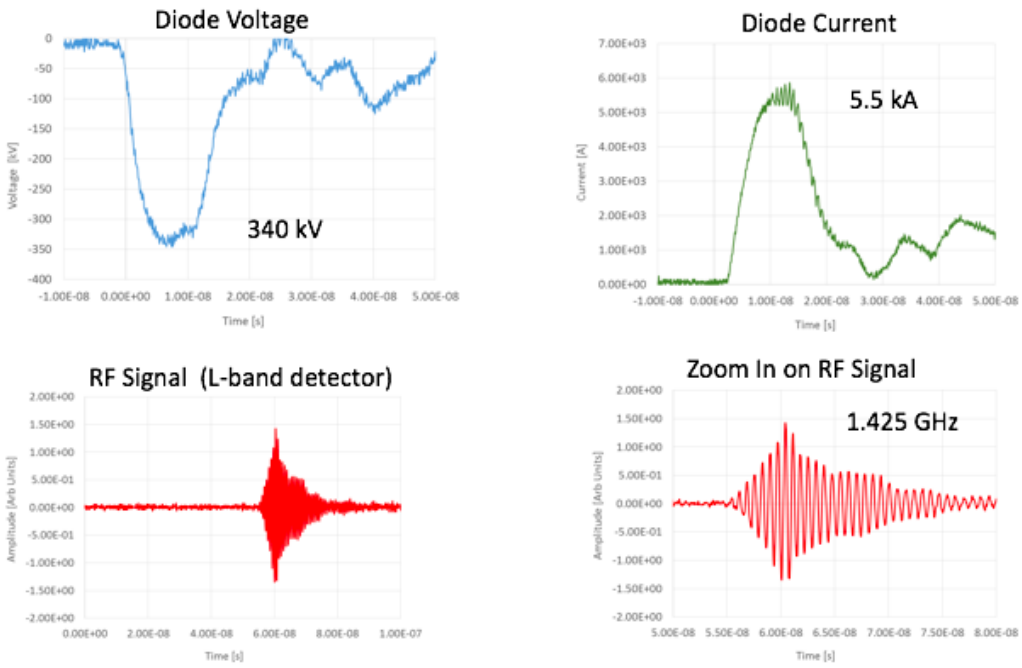

Figure 5.14 Summary of the experimental results.

CHAPTER 6: CONCLUSIONS AND FUTURE WORK

This dissertation described the design, construction, cold test, and hot test of a novel MSWS designed to generate over 100 MW in a radial dimension that is much more compact due to the double negative electromagnetic characteristics of the structure. The experimental achievement of about 100 MW radiated power from a MSWS is the highest power generated from any MSWS that has been reported in the literature.

In addition, the methodology to retrieve the material parameters and verify the double negative behavior of the MSWS was described in detail. The stepwise technique used avoided the branching problems experienced with other parameter retrieval techniques.

Furthermore, we have reported that the evolution of wave dispersion in all-metallic periodic SWSs with increasing depth of corrugation shows similar properties of waves in MSWSs and conventional periodic SWSs, such as rectangular or sinusoidal corrugated waveguide TWTs or BWOs. The important properties of MSWSs, such as the existence of the lowest order negative dispersion mode with below cutoff propagation can also be observed in traditional SWSs with deep corrugation. The hybrid EH_{11} mode has been found as the lowest order mode with increasing corrugation depth in ordinary all-metallic SWSs. Therefore, we have shown that the well-known properties of MSWSs are in common with the properties of conventional metallic periodic SWSs with deep corrugations.

Future work will test the MSWS using the full power of the SINUS-6 electron beam accelerator to demonstrate several 100 MW output power. One concern as the power

increases is the possibility of electrical breakdown occurring across the gaps of the SRRs in the MSWS. An ongoing effort by Kevin Shipman (UNM M.S. student) is to develop optical diagnostics to find evidence of electrical breakdown in the MSWS during high power generation. No evidence of breakdown has been observed at the reduced beam parameters used thus far, but breakdown is expected at the higher voltages.

Additional future work would use the HPM calorimeter to measure the radiated HPM energy to estimate the output power. Better understanding of the radiated output mode would be required in order to more reliably measure the radiated power with certainty, and that will need to be done.

REFERENCES

[1] J. Benford, J. A. Swegle and E. Schamiloglu, High Power Microwaves, Boca Raton, FL: CRC Press, 2015.

[2] R. Kompfner, "The Invention of Traveling Wave Tubes," *IEEE Trans. on Electron Devices,* vol. 23, no. 7, pp. 730 - 738, 1976.

[3] J. A. Nation, "On the Coupling of a High-Current Relativistic Electron Beam to a Slow Wave Structure," *Appl. Phys. Lett.,* vol. 17, no. 11, pp. 491-494, 1970.

[4] N. F. Kovalev, M. I. Petelin, M. D. Raizer, A. V. Smorgonskii and L. E. Tsopp, "Generation of Powerful Electromagnetic Radiation Pulses by a Beam of Relativistic Electrons," *JETP Lett.,* vol. 18, pp. 138-140, 1973.

[5] L. S. Bogdankevich, L. S. Kuzelev and A. A. Rukhadze, "Plasma Microwave Electronics," *Sov Phys-Usp,* vol. 133, pp. 3-32, 1981.

[6] Y. Carmel, J. Ivers, R. E. Kribel and J. Nation, "Intense Coherent Cherenkov Radiation due to the Interaction of a Relativistic Electron Beam with a Slow-Wave Structure," *Phys. Rev. Lett.,* vol. 33, p. 1278, 1974.

[7] A. S. Gilmour, Klystrons,Traveling Wave Tubes, Magnetrons, Cross-Field Amplifiers, and Gyrotrons, Norwood, MA: ARTECH HOUSE, 2011.

[8] P. A. Sturrock, "Kinematics of Growing Waves," *Phys. Rev. Lett.,* vol. 112, no. 5, pp. 1488-1503, 1958.

[9] [Online]. Available: http://www.ansys.com/products/Electronics/ANSYS-HFSS. [Accessed 10 October 2016].

[10] [Online]. Available: http://www.cst.com/. [Accessed 10 October 2016].

[11] B. Goplen, L. Ludeking, D. Smith and G. Warren, "User-Configurable MAGIC for Electromagnetic PIC Simulations," *Comput. Phys. Commun.,* vol. 87, pp. 54-87, 1995.

[12] R. E. Collin, Field Theory of Guided Waves, New York, NY: IEEE Press, 1991.

[13] L. Schachter, Beam-Wave Interaction in Periodic and Quasi-Periodic Structures, New York: Springer, 2011.

[14] L. Brillouin, Wave Propagation of Periodic Structures, New York, NY: McGraw-Hill Book Company, Inc., 1946.

[15] R. Thomas, "Thermionic Sources for Hi-Brightness Electron Guns," in *American Institute of Physics*, Upton, NY, 1989.

[16] R. A. Silin and V. P. Sazanov, Slow-Wave Structures, Boston, MA: National Lending Library for Science and Technology, 1971.

[17] M. Armstrong and E. L. Chu, "Cross-Wound Helices for Travelling Wave Tubes," *Appl. Phys.,* vol. 26, no. 1, pp. 33-43, January 1955.

[18] R. H. LeBorgne, C. Goodman, R. R. Hull, O. Sauseng and G. M. Lee, "Development of an 800 W Ka-Band, Ring-Bar TWT," in *Electron Devices Meeting, 1990. IEDM '90. Technical Digest., International*, San Fracisco, CA, 1990.

[19] D. R. Dyson, M. J. Clark and V. H. Smith, "Numerical Analysis of Ring-Loop and Ring-Bar Slow Wave Structures for Travelling Wave Tubes," *Transactions of IEEE International Vacuum Electronics Conference,* pp. 46-47, 2003.

[20] J. F. Gittins, Power Travelling-Wave Tubes, New York, NY: American Elsevier Pub. Co, 1965.

[21] A. V. Gunin, A. I. Klimov, S. D. Korovin, I. K. Kurkan, I. V. Pegel, S. D. Polevin, A. M. Roitman, V. V. Rostov, A. S. Stepchenko and E. M. Totmeninov, "Relativistic X-Band BWO with 3-GW Output Power," *IEEE Trans. Plasma Sci.,* vol. 26, no. 3, p. 326, 1998.

[22] S. A. Kitsanov, A. I. Klimov, S. D. Korovin, I. K. Kurkan, I. V. Pegel and S. D. Polevin, "Pulsed 5-GW Resonance Relativistic BWT for a Decimeter Wavelength Range," *Tech. Phys. Lett.,* vol. 29, no. 3, pp. 259-261, 2003.

[23] B. A. Munk, Metamaterials: Critique and Alternatives, New York, NY: John WIley and Sons, 2009.

[24] V. G. Vesalago, "The WIectrodynamics of Substances with Simultaneously Negative Values of ε and μ," *Sovy. Phys. Usp.,* vol. 10, pp. 509-514, 1968.

[25] J. B. Pendry, A. J. Holden, W. J. Steward and I. Youngs, "Extremely Low Frequency Plasmons in Metallic Mesostructures," *Phys. Rev. Lett.,* vol. 76, pp. 4773-4776, 1996.

[26] J. B. Pendry, A. J. Holden, D. J. Robbins and W. J. Steward, "Magnetism from Conductors and Enhanced Nonlinear Phenomena," *IEEE Trans. Microw. Theory Techn.,* vol. 47, no. 11, p. 2075–2084, 1999.

[27] D. R. Smith, W. J. Padilla, D. C. Vier, S. C. Nemat-Nasser and S. Schultz, "Composite Medium with Simultaneously Negative Permeability and Permittivity," *Phys. Rev. Lett.,* vol. 84, pp. 4184-4187, 2000.

[28] R. A. Shelby, D. R. Smith and S. Schultz, "Experimental Verification of a Negative Index of Refraction," *Science,* vol. 292, pp. 77-79, 2001.

[29] L. Solymar and E. Shamonina, Waves in Metamaterials, London, U.K.: Oxford University Press, 2009.

[30] R. Marques, F. Martin and M. Sorolla, Metamaterials With Negative Parameters: Theory, Design, and Microwave Applications, New York, NY: Wiley, 2008.

[31] F. Capalino, Theory and Phenomena of Metamaterials, F. Capalino, Ed., Boca Raton, FL: CRC Press, 2009.

[32] L. I. Mandelshtam, "Lectures on Some Problems of the Theory of Oscillations," in *Complete Collection of Works*, Moscow, USSR, Academy of Sciences, 1950, pp. 428-467.

[33] J. D. Jackson, Classical Electrodynamics, New York ,NY: Wiley, 1962.

[34] W. J. Padilla, D. N. Basov and D. R. Smith, "Negative Refractive Index Metamaterials," *Materials Today,* vol. 9, pp. 28-35, 2006.

[35] R. S. Penciu, K. Aydin, M. Kaesaki, T. Koschny, E. Ozbay, E. N. Economou and C. M. Soukoulis, "Multi-Gap Individual And Coupled Split-Ring Resonator Structures," *Optics Express,* vol. 16, pp. 18131-18144, 2008.

[36] K. Aydin, I. Bulu, K. Guven, M. Kafesaki, C. M. Soukoulis and E. Ozbay, "Investigation of Magnetic Resonances for Different Split-Ring Resonator Parameters and Designs," *New J. Phys.,* vol. 7, pp. 168-1-15, 2005.

[37] J. Pacheco, Theory and Application of Left-Handed Metamaterials (Ph.D. Dissertation): Cambridge, MA: Massachusetts Institute of Technology, 2004.

[38] N. Katsarakis, T. Koschny, M. Kafesaki, E. N. Economou and C. M. Soukoulis, "Electric Coupling to the Magnetic Resonance of Split Ring Resonators," *Appl. Phys. Lett.,* vol. 84, pp. 2943-2945, 2004.

[39] T. Weiland, R. Schuhmann, R. B. Greegor, C. G. Parazzoli, A. M. Vetter, D. R. Smith, D. C. Vier and S. Schultz, "Ab Initio Numerical Simulation of Left-Handed

Metamaterials: Comparison of Calculations and Experiments," *J. Appl. Phys,* vol. 90, pp. 5419-5424, 2001.

[40] R. Marques, J. Martel, F. Mesa and F. Medina, "Left-Handed-Media Simulation and Transmission of EM Waves in Subwavelength Split-Ring-Resonator-Loaded Metallic Waveguides," *Phys. Rev. Lett.,* vol. 89, pp. 183901-1-4, 2002.

[41] J. Estaban, C. C. Penalosa, J. E. Page, T. M. Guerrero and E. M. Segura, "Simulation of Negative Permittivity and Negative Permeability by Means of Evanescent Waveguide Modes—Theory and Experiment," *IEEE Trans. Microw. Theory Techn.,* vol. 53, pp. 1506-1514, 2005.

[42] D. R. Smith, D. C. Vier, T. Koschny and C. M. Soukoulis, "Electromagnetic Parameter Retrieval from Inhomogeneous Metamaterials," *Phys. Rev. E.,* vol. 71, pp. 036617-1–036617-11, 2005.

[43] X. Chen, T. M. Grzegorczyk, W. J. Pacheco and J. A. Kong, "Robust Method to Retrieve the Constitutive Effective Parameters of Metamaterials," *Phys. Rev. E,* vol. 70, pp. 016608-1-7, 2004.

[44] Z. Szabo, G. H. Park, H. Ravi and E. P. Li, "A Unique Extraction of Metamaterial Parameters Based on Kramers-Kronig Relationship," *IEEE Trans. Microw. Theory Techn.,* vol. 58, pp. 2646-2653, 2010.

[45] O. Luukkonen, S. I. Maslovski and S. A. Tretyakov, "A Stepwise Nicolson–Ross–Weir-Based Material Parameter Extraction Method," *IEEE Antennas and Wireless Propag. Lett.,* vol. 10, pp. 1295-1298, 2011.

[46] U. C. Hasar, J. J. Barroso, C. Sabah, Y. Kaya and M. Ertugrul, "Stepwise Technique for Accurate and Unique Retrieval of Electromagnetic Properties of Bianisotropic Metamaterials," *J. Opt. Soc. Am. B,* vol. 30, pp. 1058-1068, 2013.

[47] S. C. Yurt, A. Elfrgani, K. Ilyenko, M. Fuks and E. Schamiloglu, "Similarity of Properties of Metamaterial Slow Wave Structures and Metallic Periodic Structures," *IEEE Trans. on Plasma Sci.,* vol. 44, no. 8, pp. 1280-1286, 2016.

[48] J. S. Hummelt, S. M. Lewis, M. A. Shapiro and R. J. Tempkin, "Design of a Metamaterial-Based Backward-Wave Oscillator," *IEEE Trans. Plasma Sci.,* vol. 42, no. 4, pp. 930-936, 2014.

[49] W. Guo, J. Wang, Z. Chen, Y. Wang, L. Cai, G. Wang and H. Qiao, "A 0.14 THz Relativistic Coaxial Overmoded Surface Wave Oscillator with Metamaterial Slow Wave Structure," *Phys. Plasmas,* vol. 21, no. 12, pp. 123102-1–123102-5,, 2014.

[50] J. Estaban and J. M. Rebollar, "Characterization of Corrugated Waveguides by Modal Analysis," *IEEE Trans. Microw. Theory Techn.,* vol. 39, no. 6, pp. 937-943, 1991.

[51] S. Amari, R. Vahldieck, J. Bornemann and P. Leuchtmann, "Spectrum of Corrugated and Periodically Loaded Waveguides from Classical Matrix Eigenvalues," *IEEE Trans. Microw. Theory Techn.,* vol. 48, no. 3, pp. 453-460, 2000.

[52] M. Celuch-Marcysiak and W. K. Gwarek, "Spatially Looped Algorithms for Time-Domain Analysis of Periodic Structures," *IEEE Trans. Microw. Theory Techn.,* vol. 43, no. 4, pp. 860-865, 1995.

[53] R. Kompfner, "The Traveling-Wave Tube as Amplifier at Microwaves," *Proc. IRE,* vol. 35, no. 2, pp. 124-127, 1947.

[54] M. Chodorow and R. A. Craig, "Some New Circuits for High-Power Traveling-Wave Tubes," *Proc. IRE,* vol. 45, no. 8, pp. 1106-1118, 1957.

[55] N. F. Alekseev, D. D. Malairov and I. B. Bensen, "Generation of High Power Oscillations with a Magnetron in the Centimeter Band," *Proc. IRE,* vol. 32, no. 3, pp. 136-139, 1944.

[56] D. A. Watkins, Topics in Electromagnetic Theory, New York, NY: Wiley, 1958.

[57] E. Garcia, J. A. Murphy, E. De Lera and D. Segovia, "Analysis of the Left-Handed Corrugated Circular Waveguide," *IET Microw. Antennas Propag.,* vol. 2, no. 7, pp. 659-667, 2008.

[58] C. A. Balanis, Advanced Engineering Electromagnetics, 2nd ed., New York, NY: Wiley, 2012.

[59] N. F. Kovalev, I. M. Orlova and M. I. Petelin, "Wave Transformation in a Multimode Waveguide with Corrugated Walls," *Radiophys. Quantum Electron,* vol. 11, no. 5, pp. 449-450, 1968.

[60] M. Thumm, "High-Power Millimetre-Wave Mode Converters in Overmoded Circular Waveguides Using Periodic Wall Perturbations," *Int. J. Electron.,* vol. 57, no. 6, pp. 1225-1246, 1984.

[61] M. Thumm, "Computer-Aided Analysis and Design of Corrugated TE11 to HE11 Mode Converters in Highly Overmoded Waveguides," *Int. J. Infr. Millim. Waves,* vol. 6, no. 7, pp. 577-597, 1985.

[62] P. J. Clarricoats and A. D. Olver, Corrugated Horns for Microwave Antennas, London, UK: Peregrinus, 1984.

[63] S. F. Mahmoud, Electromagnetic Waveguides: Theory and Applications, London, U.K.: The Institution of Engineering and Technology, 2006.

[64] E. B. Abubakirov, M. I. Fuchs and N. F. Kovalev, "High-Selectivity Resonator for Powerful Microwave Sources," in *Proc. 11th Int. Conf. High-Power Particle Beams*, Prague, Czech Republic,, 1996.

[65] M. I. Fuks, E. Schamiloglu and Y. D. Li, "RF Priming for Operation of Relativistic TWT with Reflections Near Cyclotron Resonance," *IEEE Trans. Plasma Sci.,* vol. 42, no. 1, pp. 38-41, 2014.

[66] I. V. Lindell, S. A. Tretyakov, K. I. Nikoskinen and S. Ilvonen, "BW–Media with Negative Parameters, Capable of Supporting Backward Waves," *Microwave Opt. Technol. Lett.,* vol. 31, p. 129–133, 2001.

[67] D. M. French, D. Shiffler and K. Cartwright, "Electron Beam Coupling to a Metamaterial Structure," *Phys. Plasmas,* vol. 20, pp. 083116-1-8, 2013.

[68] J. Lu, T. M. Grzegorczyk, Y. Zhang, J. Pacheco, B. I. Wu, J. A. Kong and M. Chen, "Cerenkov Radiation in Materials with Negative Permittivity and Permeability," *Optics Express,* vol. 11, p. 723–734, 2003.

[69] M. A. Shapiro, S. Trendafilov, Y. Urzhumov, A. Alu, R. J. Tempkin and G. Shvets, "Active Negative-Index Metamaterial Powered by an Electron Beam," *Phys. Rev. B,* vol. 86, p. 085132, 2012.

[70] Y. Wang, Z. Duan, F. Wang, S. Li, Y. Nie, Y. Gong and J. Feng, "S-Band High-Efficiency Metamaterial Microwave Sources," *IEEE Trans. Electron Dev.,* vol. 63, no. 9, pp. 3747-3752, 2016.

[71] S. C. Yurt, S. Prasad, K. Ilyenko, M. Fuks and E. Schamiloglu, "O-Type Oscillator with Metamaterial-Like Slow-Wave Structure," in *Proc. IEEE Int. Vacuum Electron. Conf.*, Monterey, CA, 2014.

[72] S. Prasad, S. C. Yurt, K. Ilyenko, M. Fuks and E. Schamiloglu, "Design of a Broad-side Coupled Split Ring Resonator-Type SWS for Short Pulse E-Band Microwave Generation," in *Proc. IEEE Int. Vacuum Electron. Conf.*, Monterey, CA, 2014.

[73] S. C. Yurt, S. Prasad, K. Ilyenko, M. Fuks and E. Schamiloglu, "Dispersion Diagram Modeling for a Metamaterial-Like Slow-Wave Structure," in *Proc. IEEE Int. Vacuum Electron. Conf.*, Monterey, CA, 2014.

[74] S. C. Yurt, A. Elfrgani, K. Ilyenko, M. Fuks and E. Schamiloglu, "Evolution Of Wave Dispersion In Periodic Structures With Increasing Amplitude Of Corrugation," in *Proc. IEEE Int. Conf. Plasma Sci.*, Antalya, Turkey, 2015.

[75] S. C. Yurt, A. Elfrgani and E. Schamiloglu, "High Power Microwave Source Loaded by a Two-Spiral Metamaterial Structure for Cherenkov Radiation," in *Proc. IEEE Int. Conf. Plasma Sci.*, Antalya, Turkey, 2015.

[76] E. Schamiloglu, M. Fuks, S. Prasad, S. C. Yurt, M. A. Gilmore, S. Portillo and T. Wynkoop, "High Power Microwave Sources Using 2d Periodic Structures - Similarities with Metamaterial Structures," in *Proc. IEEE Int. Pulsed Power Conf.*, Austin, TX, 2015.

[77] S. Prasad, S. C. Yurt, S. Portillo, J. Buchenauer, M. Fuks and E. Schamiloglu, "Experimental Plan for Split Ring Resonator Type Slow Wave Structure with Double Negative Properties for High Power Microwave Generation," in *Proc. IEEE Int. Pulsed Power Conf.*, Austin, TX, 2015.

[78] S. C. Yurt, S. Prasad, M. Fuks and E. Schamiloglu, "Metamaterial Slow-Wave Structure Design for High Power Microwave Generation," in *Annual Directed Energy Symposium*, Albuquerque, NM, 2016.

[79] S. C. Yurt, S. Prasad, M. Fuks and E. Schamiloglu, "Designing of an O-Type BWO with a Metamaterial Slow-Wave Structure," in *Proc. IEEE Int. Vacuum Electron. Conf.*, Monterey, CA, 2016.

[80] E. Schamiloglu, S. C. Yurt, S. Prasad and M. Fuks, "Advances in All-Metal Metamaterial Slow Wave Structure Design for High Power Microwave Generation," in *Proc. EUROEM-2016*, London, UK, 2016.

[81] S. C. Yurt, M. I. Fuks, S. Prasad and E. Schamiloglu, "Design of a Metamaterial Slow Wave Structure for an O-Type High Power Microwave Generator," *Phys. Plasmas,* vol. 23, no. 12, pp. 123115-1-7, 2016.

[82] M. I. Fuks, "Forming of Relativistic Electron Beam in Coaxial Diode with Magnetic Insulation," *Sov. Phys. Tech. Phys.,* vol. 27(4), pp. 451-453, 1982.

[83] B. N. Breizman and D. D. Ryutov, "Powerful Relativistic Electron Beam in a Plasma and in a Vacuum (Theory)," *Nucl. Fusion,* vol. 14, pp. 873-907, 1974.

[84] A. I. Fedosov, E. A. Litvinov, S. Y. Belomytsey and S. P. Bugaey, "Account of Electron Beam Parameters in Diodes with Magnetic Insulation," *Izv. VYZov. Fizika,* vol. 10, pp. 134-135, 1977.

[85] R. Z. Sagdeev and A. A. Galaev, Nonlinear Plasma Theory, New York, NY: W. A. Benjamin, Inc., 1969.

[86] N. M. Bykov, V. P. Gubanov, A. V. Gunin, F. Y. Zagulov, S. D. Korovin and A. F. Yakushev, "High-Current Periodic-Pulse Electron Accelerator with Highly Stable Electron-Beam," *Instrum. Exp. Tech.,* vol. 32, pp. 33-36, 1987.

[87] S. D. Korovin and V. V. Rostov, "High-Current, Nanosecond, Pulse-Periodic Electron Accelerators using a Tesla Transformer," *Russian Phys. J.,* vol. 19, p. 1177, 1996.